Design of Lens-Absorber Coupled Microwave Kinetic Inductance Detectors at 1.5 THz

and Evaluation of their Quasi-Optical Coupling for Far-Infrared Spectroscopic Astronomical Observations

Daan Roos

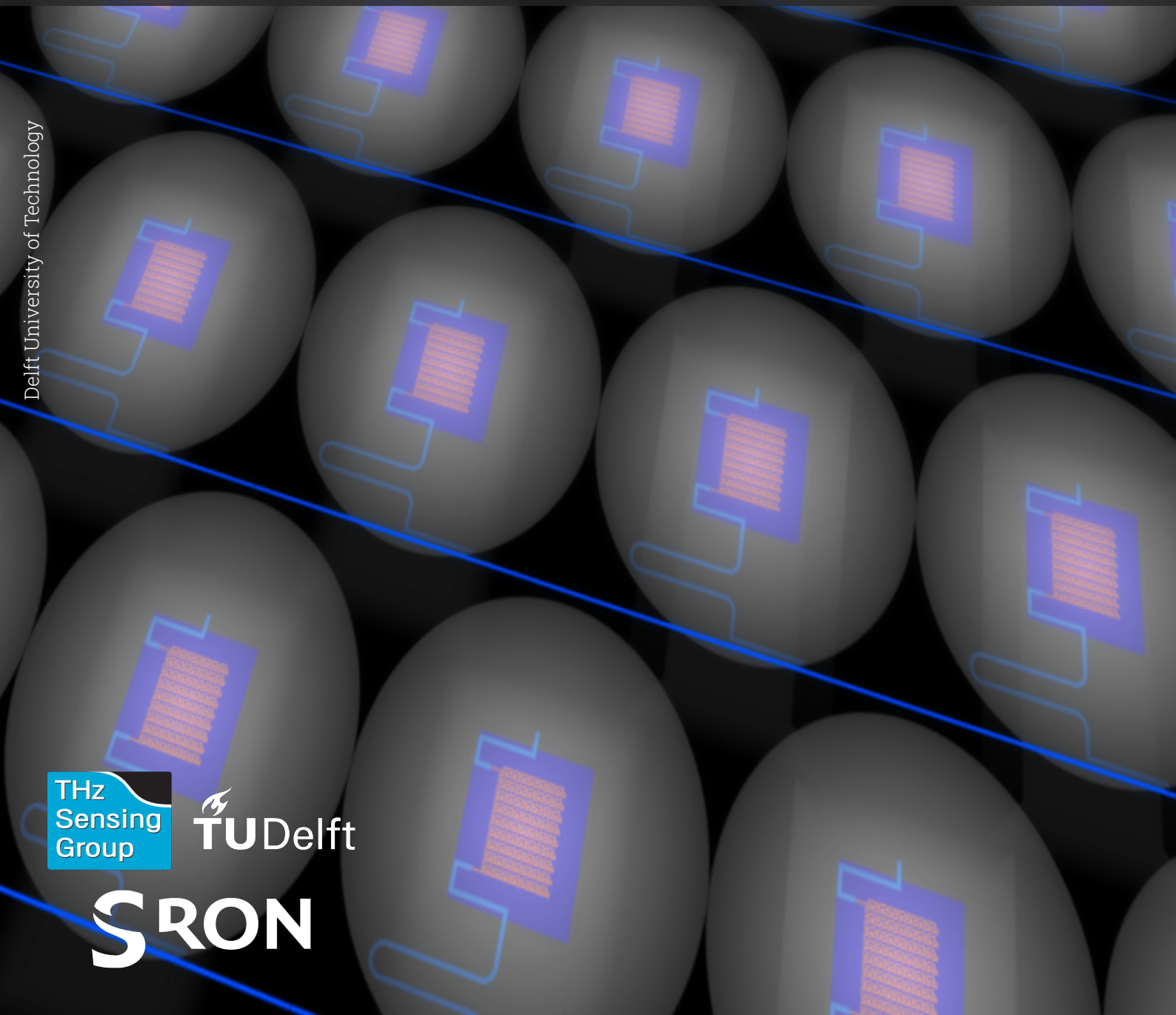

Delft University of Technology

THz Sensing Group

TU Delft

SRON

Design of Lens-Absorber Coupled Microwave Kinetic Inductance Detectors at 1.5 THz

and Evaluation of their Quasi-Optical Coupling for Far-Infrared Spectroscopic Astronomical Observations

by

Daan Roos

to obtain the degree of Master of Science in Electrical Engineering,
Track: Wireless Communication and Sensing,
at the Delft University of Technology,
to be defended publicly on Monday August 26, 2024 at 9:00 AM.

Student number:	4953487	
Thesis committee:	Prof. dr. ir. J.J.A. Baselmans,	TU Delft/SRON, supervisor
	dr. ir. S.O. Dabironezare,	TU Delft/SRON, supervisor
	dr. ir. W. Jellema,	University of Groningen/SRON, co-supervisor
	dr. N. Bhattacharya,	TU Delft

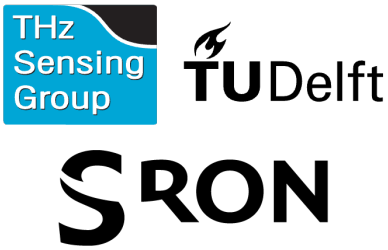

Abstract

Despite advances in astronomy, much of the universe remains hidden behind gas and dust clouds that absorb optical radiation, making it undetectable by conventional telescopes. Far-Infrared (FIR) radiation is capable of propagating through these clouds, and offers a solution for observing these obscured interstellar regions. However, the sensitivity of existing detector systems is insufficient to detect FIR radiation effectively. This thesis focuses on the development of highly sensitive detectors based on Microwave Kinetic Inductance Detectors (MKIDs) that meet the sensitivity requirement for use in future space missions, specifically the NASA led POEMM and PRIMA missions, covering a frequency range from approximately 1.5 THz to 12 THz.

While detectors have been developed previously covering the upper band of this frequency range at 6.98 THz and 12 THz, the lower band remains uncovered. Therefore, lens-absorber coupled MKIDs designed to operate at 1.5 THz are presented, with their performance analysed using models based on the Geometrical Optics-Fourier Optics (GOFO) technique in combination with a Floquet wave approach for periodic absorbers. Additionally, the design methodology of MKIDs to operate at specific readout frequencies is discussed. Absorber coupled MKIDs are limited to lower resonance frequencies with respect to comparable antenna based MKIDs, which offer advantages for space-based missions due to reduced power consumption, but do present challenges for readout systems operating at higher frequencies. In this thesis, two lens-absorber coupled MKID designs were developed and are currently being fabricated as candidates to experimentally demonstrate highly sensitive detector arrays operating at 1.5 THz.

The imaging spectrometers in the POEMM and PRIMA missions require a dispersive element to separate different wavelengths of the incoming radiation. The dispersive element envisioned for these missions, the Virtually Imaged Phased Array (VIPA), suffers from non-idealities, causing phase aberrations in the transmitted field, and part of the power transmitting towards unwanted propagation directions, which can degrade instrument performance. This thesis presents and analyses optimisation techniques to mitigate these effects, thereby enhancing the overall efficiency and degrees of freedom for designing the full instrument.

Furthermore, absorbers, unlike antenna-based devices, are multi-mode detectors. Understanding how absorbers couple to higher-order modes is crucial for optimising their performance. This thesis introduces and validates a model based on a novel experimental technique, Energy Absorption Interferometry (EAI), to extract a modal description of detectors. In the future steps related to the POEMM mission, the findings from this initial investigation into multi-mode absorbers will be used to gain insight and explore possible improvement routes in the coupling of these detectors to complex optical systems.

Acknowledgements

First and foremost, I would like to extend my sincere gratitude to my supervisors, Prof. Dr. Ir. Jochem Baselmans and Dr. Ir. Shahab Dabironezare, for their immense support, dedication, and passion for their work. Their commitment to sharing their knowledge has greatly influenced my academic journey.

Jochem, your enthusiasm for your work and genuine curiosity about the work of others is inspiring and a great motivator. Your passion and enthusiasm were one of the reasons I entered this field after attending one of your lectures of the Electronics for Imaging course during the (albeit short-lived) Physics of Electronics Minor in 2020, where you introduced me to the world of detector design. Even when you are extremely busy, you are always open for discussions about one of the various topics you always seem to know everything about, or (on some rare occasions) learn about something that I know all about, which is one of the reasons working with you has been such a great experience.

Shahab, you are everything a student could hope for in a supervisor. Your tireless efforts to ensure people understand what they are working on and struggling with, whether that will take you 5 minutes or a few hours, are deeply appreciated. More importantly, you always want to make sure that people are doing fine personally, and whether they still enjoy the work they are doing, which I have a lot of respect for. Your relaxed attitude and casual chats are really appreciated, and ensures that working with you is an incredibly fun experience.

I am looking forward to continue working with you two in the coming years.

Additionally, I would like to thank Dr. Ir. Willem Jellema. Although we began working together later in my thesis, your insightful contributions and willingness to discuss ideas have been invaluable and very educational. Your knowledge about optics and radio astronomy have taught me a lot and I am looking forward to collaborate in the coming years.

I would like to thank the Professors, Associate Professors, and Assistant Professors of the TeraHertz Sensing group. Your extensive knowledge of Electromagnetism, Astronomy, and Science and Engineering has taught me a lot and motivates me to learn more every day. To the full TeraHertz Sensing group, I would like to thank you all for the welcoming and relaxed environment you have created, which I am really proud to be apart of.

I would like to specifically thank my wonderful office mates, for our anjoyable chats and relaxed Friday afternoons. To Petar and Çağın, I am glad to have experienced these last two years together. To Kian and Constance, although we only have met a couple of months ago, I am really glad we've gotten so close in such a short time. I am very happy to be able to call you all my friends.

To my close friends: Alex, Chris, David, Jakob, and Tycho. We have started this (academic) journey together 6 years ago, and I am very sure it would have been far more difficult and far less enjoyable if we had not done this together. Looking forward to what we will experience next. I also want to thank Tycho and Chris for their unscheduled visits during my thesis, forcing me to take a coffee break every once in a while (or daily for that matter). This year would have been much more stressful otherwise.

Finally, I would like to express my deepest gratitude towards my family. To my brother, Matthijs, thank you for your support, curiosity, and the countless conversations that helped me through both scientific and personal challenges. I am impressed by all the work you do and I am looking forward to what you will achieve next. To my parents, I want to thank you for your endless support and faith in the work I do. Although these last few months have been a bit hectic, I know I can always count on your love and support. This journey wouldn't have been possible without your faith in me.

Contents

1

Introduction

Over the last few decades, astronomical instrumentation has evolved rapidly, leading to groundbreaking discoveries in both radio and optical domains, including various exoplanets, black holes, and supernovae. Despite these advances, radiation from astronomical objects at optical wavelengths is limited by the absorption by interstellar dust and gas. This limitation becomes particularly problematic when studying dust-obscured galaxies and the radiation from the dust itself, which is crucial for improving our understanding of the evolution of our universe. Moreover, we can learn the molecular content of these dusty environments, including water vapor, ice, and various products of star formation, by performing spectroscopic observations to measure the frequencies, and shapes, of their emissions lines. This allows us to determine the type of molecules, their temperature, and abundance. This offers great insight into the formation and evolution of stars, galaxies and planetary systems, as well as the origins of water on earth and the potential existence of earth-like planets.

Far-Infrared (FIR) radiation, spanning roughly from 100 GHz to 30 THz (corresponding to wavelengths from 3 mm to 10 $\mu\mathrm{m}$), offer a window into interstellar regions invisible at optical wavelengths. Unlike optical radiation, FIR radiation can penetrate dusty clouds. Additionally, key molecules such as water and products of star formation emit FIR radiation; spectral lines from distant galaxies are also often redshifted into this frequency band. However, designing effective instruments for this frequency range has proven problematic. The FIR range, which is part of the so-called "TeraHertz gap" defined roughly as the range from 0.1 THz to 30 THz, is absorbed by the earth's atmosphere, limiting the use of earthbound telescopes. In addition to this, existing instruments often require long observation times due to low sensitivities, as shown in Fig. 1.1 [1].

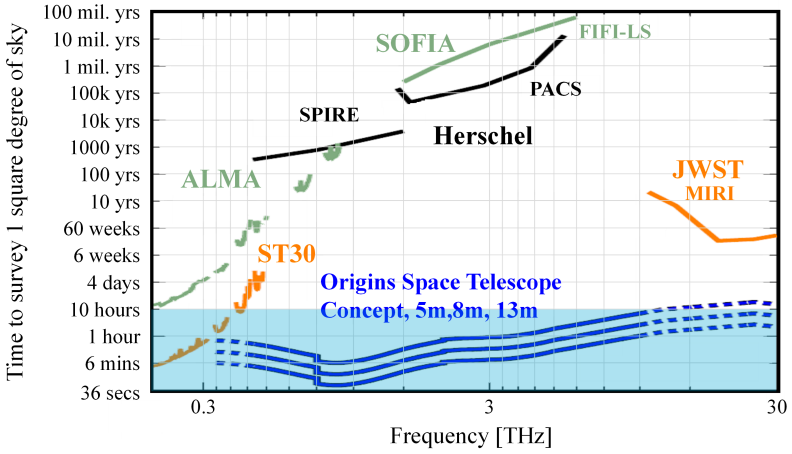

Fig. 1.1: The observation time required by various instruments to observe 1 square degree of sky for a certain frequency in the TeraHertz gap. This figure is reproduced from a figure in [1].

In order to provide an instrument capable of performing FIR measurements within reasonable observation time, detectors must be designed with a high sensitivity, achieving a Noise Equivalent Power (NEP) in the order of $10^{-20}\ \mathrm{W}/\sqrt{\mathrm{Hz}}$. Recent advancements in Microwave Kinetic Inductance Detectors (MKIDs) have demonstrated the potential to satisfy this NEP requirement [2] and [3], while providing capabilities to multiplex large imaging arrays [4]. With these technologies in hand, various missions have been proposed to explore the FIR spectrum. Among them, the Netherlands Institute for Space Research (SRON) is involved in the development of detectors for two key missions: the Planetary Origins and Evolution Multispectral Monochrometer (POEMM) mission in collaboration with NASA Goddard [5] and [6], and the Probe for far-Infrared Mission for Astrophysics (PRIMA) mission in collaboration with NASA Goddard and NASA JPL [7]. This thesis will focus on the design and analysis of detectors in preparation for these missions.

1.1. Missions for Far-Infrared: POEMM and PRIMA

The POEMM mission, is a long duration, high altitude balloon mission planned to operate at an altitude of 45 km above Antartica [5] and [6]. The instrument consists of a multi-band spectrometer operating from roughly 3 THz to 12 THz, as shown in Fig. 1.2. POEMM will be used to improve the understanding of planet formation, the evolution of protoplanetary disks, and the atmospheres of giant planets. SRON will deliver the detector modules for POEMM.

PRIMA is a space-probe that will operate for over 5 years [7]. SRON will contribute to one of two instruments aboard the PRIMA space-probe: the PRIMAger, which has imaging, spectrometry, and polarimetry capabilities [7]. The frequency bands of each of these devices is shown in Fig. 1.2, and covers a total range of roughly 1.5 THz to 12 THz. Due to the high sensitivity of the detectors in the PRIMAger instrument, the observation times are expected to be at least 4 orders of magnitude faster compared to Herschel [7]. The PRIMA space-probe will be used for science cases ranging from probing star formation, to investigating the ratio between Deuterium and Hydrogen in distant galaxies, and measuring heavy elements in early universe dust clouds [7].

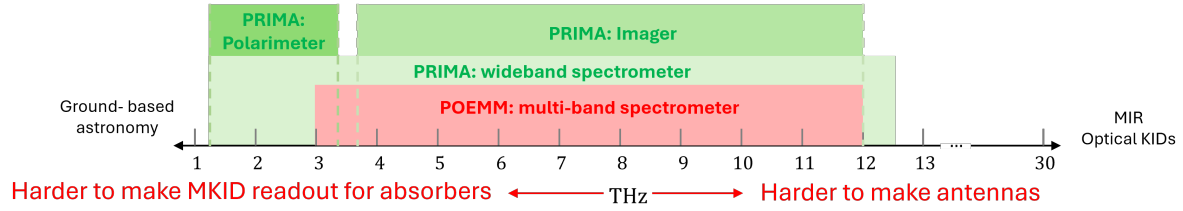

Fig. 1.2: The frequency bands covered by each of the instruments in the PRIMA and POEMM missions.

The instruments on board of the aforementioned missions are working towards an imaging-spectrometer. As the name implies, an imaging-spectrometer provides imaging capabilities at different frequencies. Such a device consists of a 2D array of detectors, where the detectors along one axis will perform imaging in the spatial domain, while the detectors along the other axis perform imaging in the frequency domain. Since the incoming radiation from the telescope dish that is targeting an astronomical source of interest contains multiple frequencies, a dispersive element is added to the optical chain, to create an angular distribution of frequencies, as shown in Fig. 1.3. In the discussed missions, a Virtually Imaged Phased Array (VIPA) is envisioned here as the dispersive element, capable of producing a large angular-dispersion versus wavelength [8].

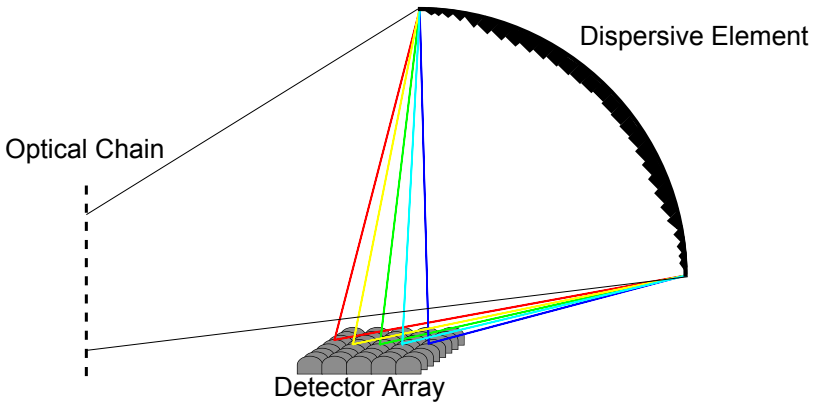

Fig. 1.3: A simple representation of an imaging spectrometer, with a grating reflector as a dispersive element to couple radiation at different wavelengths to different detectors.

While lens-antenna coupled MKIDs have been demonstrated to reach the NEP required for FIR observations [2], designing and fabricating is difficult for FIR observations, and lens-antennas provide single polarisation radiation detection, which is an advantage if the polarisation state needs to be measured, but a disadvantage if the total power is to be measured, as they will miss half the signal power. Additionally, lens-antenna systems are difficult due to two complexities. First of all, antennas are coherent detectors and therefore sensitive to aberrations in the phase of the incoming field. The dispersive elements used in spectroscopy are not ideal, and will aberrate the field that is scattered towards the lens-antenna. Especially at higher frequencies, these aberrations will become more apparent, leading to worse coupling. The second problem ties into the first one: at frequencies above 5 THz imperfections introduced during the fabrication, assembly, and alignment of the lens-antennas is large in terms of wavelength. Due to this, sufficient control over the phase of the incident field coming to the antenna is not feasible, leading to large uncertainty and the possibility of significant reduction in coupling.

An alternative to using antennas, is to use absorbers. An advantage of their incoherent nature is that they are less sensitive to (phase) aberrations of the incoming field. Absorbers can be used directly as an incoherent detector below the telescope system; however, large absorbers are then needed to improve the optical coupling as the absorption scales with the size of the absorber. Such large absorbers will reduce the spatial and frequency resolution of the imaging-spectrometer and limit the sensitivity of the detector. By introducing an extra focusing element above the absorber, e.g. an integrated lens, the absorber size can be reduced and the optical coupling of the system can be controlled via the lens design.

Lens-absorber coupled MKIDs have been presented for the aforementioned FIR missions for 6.98 THz and 12 THz [9]. Since the frequency bands of the FIR missions reach down to roughly 1.5 THz, lens-absorbers also operating at this frequency were envisioned. Although lens-antennas at this frequency aren't as affected by misalignments as at higher frequencies, and have been designed to operate at frequencies of 1.5 THz [2], absorbers allow more naturally for dual polarisation radiation reception, and are more forgiving in terms of aberrations of the incoming field, which is especially relevant when operated behind a dispersive element. Additionally, absorbers, especially at lower frequencies, will allow for smaller detectors that can be read-out at lower readout frequencies. The latter allows for cheaper, less power hungry, and simpler readout systems. Therefore, this thesis focuses on the design of lens-absorber coupled MKIDs at 1.5 THz.

1.2. Thesis Outline

This thesis consists of 6 chapters, including this introduction. In Ch. 2, the design and analysis of lens-absorber coupled MKIDs is discussed. This chapter introduces modelling techniques to assess the performance of lenses and periodic absorbers, and puts specific focus on the integration of these absorbers into MKIDs operating at specific readout frequencies.

The realization of the designed lens-absorbers for 3 different experiments is discussed in Ch. 3, and a developed tool is discussed to automate the mask design of absorber coupled MKID-arrays.

Ch. 4 focuses on the non-ideal behaviour of the dispersive element proposed in the presented missions. The chapter introduces various optimisation techniques to mitigate the effect of these non-idealities, and applies these on 2 test cases.

An initial investigation into the multi-modal behaviour of lens-absorbers is performed in Ch. 5. A novel modelling tool capable of applying the experimental Energy Absorption Interferometry (EAI) technique is developed and validated, and used to perform a set of initial investigations on the multi-modal behaviour of a lens-absorber designed in this thesis.

Finally, in Ch. 6, the conclusions of this thesis are presented, and the knowledge obtained in this thesis is used to present future research directions.

2

Design and Analysis of 1.5 THz Detectors

In this chapter the design of the lens-absorber coupled Microwave Kinetic Inductance Detectors (MKIDs) operating at 1.5 THz will be discussed in detail. The principles of designing the absorber and the lens is discussed, and subsequently lens-absorber designs are introduced in detail. Afterwards, the integration of the absorber into an MKID structure is elaborated, and the design methodology of the MKIDs to operate at a specific readout frequency is discussed.

2.1. Design Considerations

The imaging-spectrometers for the missions discussed in this thesis will consist of two major parts: the dispersive element, and the detector array. Commonly, and element such as a diffraction grating is used as a dispersive element, however, the diffraction grating is typically capable of providing spectra with limited resolution [8]. Instead, a Virtually Imaged Phased Array (VIPA) is envisioned here as the dispersive element, capable of producing a large angular-dispersion versus wavelength [8].

The sources' power received by the dispersive element at FIR frequencies is low. As will be discussed in Ch. 4, combining this with the overall efficiency of a practical VIPA, i.e. the power is lost in the VIPA or radiated towards directions other than the lens-absorber of interest, detectors should be designed with low losses and high optical coupling in mind. As the lens will introduce a large amount of dielectric material above the detector, a dielectric should be chosen with low losses at FIR frequencies. The only available material capable of providing low losses is high resistive silicon with a cryogenic relative permittivity of $\epsilon_r = 11.44$.

Another important material choice, is the one of the absorber and MKID, as this will limit the sensitivity of the detector. As discussed in Ch. 1, the mentioned science cases in the introduced FIR missions require an NEP in the order of $10^{-20}\ \mathrm{W}/\sqrt{\mathrm{Hz}}$ [2], [3], and [9]. As shown in [3], Aluminium is capable of providing these sensitivities at a large range of loading powers ranging from 70 zW to 200 fW, and is therefore an ideal superconductor candidate for the material of the detector.

Although the combination of Silicon and Aluminium offer good performance in terms of losses and NEP, their impedance values do complicate the design of the absorber at FIR frequencies. Although matching an Aluminium absorber to free space (with a characteristic impedance of $Z_0 \approx 377\Omega$) is even more difficult, due to the high-resistive nature of Silicon (with a characteristic impedance in the order of $Z_d \approx 111.5\Omega$), matching Aluminium with a low sheet resistance in the orders of $R_s < 1\Omega/\square$ is still a challenge. Therefore, this chapter will discuss an alternative design, similar to the designs presented in [10], capable of matching the impedance of the low-resistive Aluminium to the high-resistive Silicon at THz frequencies, different from the traditional square or strip absorbers [11].

2.1.1. Lens-Absorber Considerations

Practical absorber designs are often misunderstood as “ideal” absorbers, capable of absorbing all radiation falling directly on top of them, with a cosine shaped Field of View (FoV) due to the projection of power over a conductive sheet. In this chapter, accurate modelling techniques are employed to demonstrate lens-absorbers’ capability in absorbing power from all directions, and obtain the pattern in reception associated with them. The width of this pattern depends on the size of the absorber, and is referred to as the focusing efficiency of the absorber [12]. Since the size of the absorber also impacts the amount of power absorber by the lens-absorber, a trade-off is introduced between the focusing and absorbing capabilities of the detector. This trade-off is worse in the case of absorber based systems with respect to antenna based ones [12].

The resulting wider pattern in reception for lens-absorbers (with respect to lens-antennas), impacts the capabilities of the instrument to spatially discriminate between astronomical sources. Moreover, since the pattern in reception is wider, it is far more sensitive to noise sources, stray light in the cryostat, and to side-lobes of fields focused on neighbouring lens-absorbers in the detector array below a VIPA. These complexities should be taken into account when designing lens-absorbers for FIR missions, and effort should be put into reducing the effect of the widening of the patterns in reception by either improving the noise and stray-light control in the cryostat, and side-lobe levels of the VIPA, or by narrowing the pattern of the designed lens-absorbers.

Another aspect of absorbers that is often overlooked, is the coupling to higher-order Floquet modes by the absorber. For absorbers consisting of a periodic structure, the absorber behaves similar to an antenna array. Once the spacing between the unit-cells of the periodic structure is large (a periodicity above half wavelength), the absorber will produce grating-lobes in its pattern in reception. These grating lobes reduce the performance of the absorber below a lens by reflecting power to skew angles which could lead to high cross talk between detectors.

This chapter will put specific attention to techniques to design lens-absorbers and methods that could possibly aid in optimising the designs of lens-absorbers while maintaining high optical coupling, good sensitivity, and the possibility to control the pattern of the detector.

2.2. Detector Analysis and Modelling

Although lens-absorber systems can be modelled using numerical solvers, the computation time required to simulate the response of such devices to a single incident field is significant. The lenses employed in this thesis are large with respect to the wavelength of the source: in the order of $D_{lens} \approx 7\lambda_0$. Due to this, time domain simulations will take a significant amount of time, as the field will have to propagate through a large Silicon volume. Once these devices are used in flight, the final devices require lenses with an even larger footprint, in the orders of $D_{lens} \approx 20\lambda_0$. As a result, resorting to numerical solvers alone will complicate the design and analysis process of the lens-absorber devices.

Adding to the complexity, the need to iteratively optimise the device, and extract the full pattern in reception, leads to a large number of simulations per lens-absorber. Running all these simulations using numerical solvers is an impossible task. Therefore, there is a need for an equivalent model to describe the coupling of the full lens-absorber device to incident EM radiation.

2.2.1. Absorber Floquet-Wave Model

The spectral response of a periodic absorber to an incoming field can be modelled using a Floquet Wave-field representation. By focusing only on the fundamental Floquet modes, the response to an incoming plane wave can be modelled using the equivalent circuit in Fig. 2.1a [12]. The circuit is based on the stratification of the absorber, as can be seen in Fig. 2.1b, which consists of a semi-infinite slab of dielectric background material, the periodic absorber, and a backing reflector.

In this model, the fundamental incoming TE and TM modes propagating through the background material are represented by two transmission lines feeding into the absorber. The absorber, which can be represented by its Z-parameters, is assumed to have a periodicity much smaller than half a wavelength ($d_{x/y} \ll \lambda/2$), and the model assumes an infinitely extended absorber array.

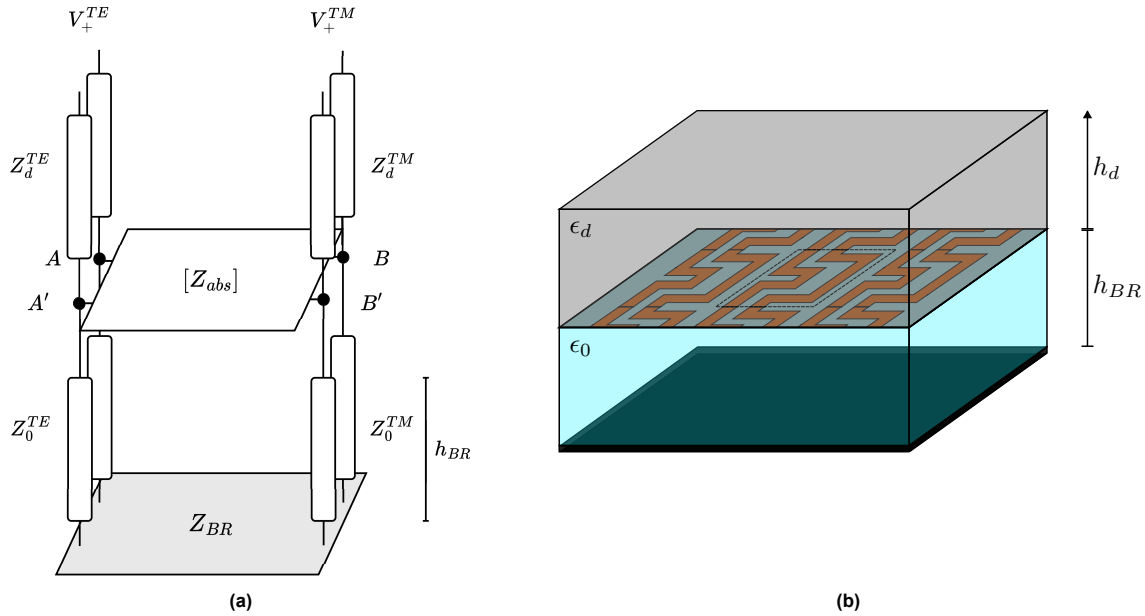

Fig. 2.1: The Floquet Wave transmission line model (a) used to model the response of the meandering line absorber terminated by a backing reflector (b). The meandering line absorber (given in orange in Fig. 2.1b) is represented by its Z-parameters in Fig. 2.1a. The absorber has a semi-infinite slab of dielectric on top with a relative permittivity ϵ_d, and is represented by two semi-infinite transmission lines with characteristic impedances $Z_d^{TE/TM}$ in Fig. 2.1a. The backing reflector with height h_{BR} has a permittivity of free space and is represented by two shorted transmission lines with characteristic impedances $Z_0^{TE/TM}$ in Fig. 2.1a.

The direct field falling on top of the absorber can be represented by a set of voltage sources $V_+^{TE/TM}$ for TE and TM excitations, by averaging the electric field over the absorber's unit cell [12]:

$$V_+^{TE}(\vec{k}_\rho) = \sqrt{d_x d_y} E_\phi^d(\vec{k}_\rho) \tag{2.1}$$

$$V_+^{TM}(\vec{k}_\rho) = \sqrt{d_x d_y} E_\theta^d(\vec{k}_\rho) \frac{k_{zd}}{k_d} \tag{2.2}$$

These voltages propagate through the dielectric material and interact with the absorber described by its Z-parameters. This interaction causes part of the incoming power to be absorbed, and part of the power to be reflected back. The absorption and reflection can be represented by calculating the currents in the absorber, $I^{TE/TM}$, and the voltages reflected back towards the source $V_-^{TE/TM}$.

In order to calculate $V_-^{TE/TM}$, the scattering parameters S_{abs} at the absorber interfaces AA' and BB' must be determined. These can be calculated by transforming the Z-parameters of the absorber while taking the impedance of the backing reflector into account. Since the absorber will not behave symmetrically to incoming plane waves with different angles of incidence, the transformation from Z- to S-parameters is performed for a non-reciprocal case. The derivation for this transformation will be

discussed in App. A. Based on these S-parameters, the reflected voltage sources can be calculated using:

$$\begin{bmatrix} V_-^{TE}(\vec{k}_\rho) \\ V_-^{TM}(\vec{k}_\rho) \end{bmatrix} = S_{abs}(\vec{k}_\rho) \begin{bmatrix} V_+^{TE}(\vec{k}_\rho) \\ V_+^{TM}(\vec{k}_\rho) \end{bmatrix} \tag{2.3}$$

The total currents on the absorber can be calculated from these sources. When dealing with a perfect $\frac{\lambda}{4}$-backing reflector, the total current in the absorber can be calculated as:

$$I^{TE/TM}(\vec{k}_\rho) = \frac{1}{Z_d^{TE/TM}} \left(V_+^{TE/TM}(\vec{k}_\rho) - V_-^{TE/TM}(\vec{k}_\rho) \right) \tag{2.4}$$

However, the air-cavity is not exactly a quarter of a wavelength. Therefore $I^{TE/TM}$ are determined for a backing reflector with arbitrary height, as derived in App. B:

$$I^{TE}(\vec{k}_\rho) = \frac{V^{TE}(\vec{k}_\rho) - \frac{Z^{TETM}(\vec{k}_\rho)}{Z^{TMTM}(\vec{k}_\rho)} V^{TM}(\vec{k}_\rho)}{Z^{TETE}(\vec{k}_\rho) - \frac{Z^{TETM}(\vec{k}_\rho) Z^{TMTE}(\vec{k}_\rho)}{Z^{TMTM}(\vec{k}_\rho)}} \tag{2.5}$$

$$I^{TM}(\vec{k}_\rho) = \frac{V^{TM}(\vec{k}_\rho) - \frac{Z^{TMTE}(\vec{k}_\rho)}{Z^{TETE}(\vec{k}_\rho)} V^{TE}(\vec{k}_\rho)}{Z^{TMTM}(\vec{k}_\rho) - \frac{Z^{TMTE}(\vec{k}_\rho) Z^{TETM}(\vec{k}_\rho)}{Z^{TETE}(\vec{k}_\rho)}} \tag{2.6}$$

From the total current on the absorber, and the total voltage at the absorber terminals $V^{TE/TM} = V_+^{TE/TM} + V_-^{TE/TM}$, the averaged magnetic and electric spectral fields can be derived in Cartesian coordinates as follows [12]:

$$\begin{bmatrix} E_x^t(\vec{k}_\rho, z) \\ H_x^t(\vec{k}_\rho, z) \end{bmatrix} = \begin{bmatrix} E_{k_\rho}^t(\vec{k}_\rho, z) \\ H_{k_\rho}^t(\vec{k}_\rho, z) \end{bmatrix} (\hat{k}_\rho \cdot \hat{x}) + \begin{bmatrix} E_\phi^t(\vec{k}_\rho, z) \\ H_\phi^t(\vec{k}_\rho, z) \end{bmatrix} (\hat{\phi} \cdot \hat{x}) \tag{2.7}$$

$$\begin{bmatrix} E_y^t(\vec{k}_\rho, z) \\ H_y^t(\vec{k}_\rho, z) \end{bmatrix} = \begin{bmatrix} E_{k_\rho}^t(\vec{k}_\rho, z) \\ H_{k_\rho}^t(\vec{k}_\rho, z) \end{bmatrix} (\hat{k}_\rho \cdot \hat{y}) + \begin{bmatrix} E_\phi^t(\vec{k}_\rho, z) \\ H_\phi^t(\vec{k}_\rho, z) \end{bmatrix} (\hat{\phi} \cdot \hat{y}) \tag{2.8}$$

where $E_{k_\rho/\phi}^t$ and $H_{k_\rho/\phi}^t$ are defined as

$$E_{k_\rho}^t(\vec{k}_\rho, z) = \frac{1}{\sqrt{d_x d_y}} V^{TM}(\vec{k}_\rho, z) \tag{2.9}$$

$$E_\phi^t(\vec{k}_\rho, z) = \frac{1}{\sqrt{d_x d_y}} V^{TE}(\vec{k}_\rho, z) \tag{2.10}$$

$$H_{k_\rho}^t(\vec{k}_\rho, z) = -\frac{1}{\sqrt{d_x d_y}} I^{TE}(\vec{k}_\rho, z) \tag{2.11}$$

$$H_\phi^t(\vec{k}_\rho, z) = \frac{1}{\sqrt{d_x d_y}} I^{TM}(\vec{k}_\rho, z) \tag{2.12}$$

In order to calculate the absorbed power from these spectral fields, the inverse Fourier transform is applied to obtain the spatial total fields $\vec{e}_t$ and $\vec{h}_t$. The power absorbed can be determined by integrating the Poynting vector over the finite absorber domain as:

$$P_{abs} = \frac{1}{2} \Re \left\{ \iint_{S_{abs}} \left[\vec{e}_t(x, y) \times \vec{h}_t^*(x, y) \right] \cdot \hat{z} \, \mathrm{d}S_{abs} \right\} \tag{2.13}$$

2.2.2. Lens Modelling using GOFO Techniques

In Sec. 2.2.1, a model was discussed that replaces the need for numerical solvers to evaluate the performance of a periodic absorber. The Floquet Wave model is capable of evaluating the power absorbed from a single plane wave. Thus, to evaluate the performance of the full lens-absorber device, the response of a focusing lens, i.e. its focal field, is represented as a Plane Wave Spectrum (PWS).

A commonly used method to model Quasi-Optical components, is the Physical Optics (PO) technique. The PO technique can be used to analyse the scattering behaviour of Quasi-Optical components. The scattered fields on a surface can be estimated by equivalent current densities and using the equivalence theorem [13] and [14]:

$$\vec{J}(\vec{r}') = \hat{n} \times \vec{H}^{total}(\vec{r} = \vec{r}') = \hat{n} \times \left[\vec{H}^{i}(\vec{r} = \vec{r}') + \vec{H}^{s}(\vec{r} = \vec{r}')\right] \tag{2.14}$$

$$\vec{M}(\vec{r}') = -\hat{n} \times \vec{E}^{total}(\vec{r} = \vec{r}') = -\hat{n} \times \left[\vec{E}^{i}(\vec{r} = \vec{r}') + \vec{E}^{s}(\vec{r} = \vec{r}')\right] \tag{2.15}$$

where $\vec{H}^{i}$ and $\vec{E}^{i}$ are the incident fields on the surface, $\vec{H}^{s}$ and $\vec{E}^{s}$ are the scattered fields which could be either reflecting, or transmitting, and $\hat{n}$ is the normal vector on the surface. The scattered fields are calculated by assuming a locally flat interface at each location of the Quasi-Optical component. The equation is evaluated at the surface of the component, which is indicated by $\vec{r} = \vec{r}'$. To evaluate the focal-field, these current densities can be propagated in a homogeneous medium by applying the radiative part of the Green's function:

$$\vec{e}_f(\vec{r}) = \iint_{S'} j\vec{k} \times \vec{M}(\vec{r}') \frac{e^{-jk|\vec{r}-\vec{r}'|}}{4\pi\,|\vec{r}-\vec{r}'|}\,\mathrm{d}S' - j\omega\mu \iint_{S'} \left[\vec{J}(\vec{r}') - \left\{\hat{k} \cdot \vec{J}(\vec{r}')\right\}\hat{k}\right] \frac{e^{-jk|\vec{r}-\vec{r}'|}}{4\pi\,|\vec{r}-\vec{r}'|}\,\mathrm{d}S' \tag{2.16}$$

where $\vec{e}_f(\vec{r})$ represents the scattered field at observation position $\vec{r}$, $\vec{r}'$ is a position on the equivalent surface, $\hat{k} = \frac{\vec{r}-\vec{r}'}{|\vec{r}-\vec{r}'|}$, $\vec{k} = k\hat{k}$, and k is the wavenumber in the medium.

Although this method offers an accurate approximation of the performance of various Quasi-Optical components [14], the focal-field calculated using this method does not comply with a requirement set at the start of this section. In order to couple the field calculated in Eq. 2.16 to the Floquet Wave absorber model, the field should be a Plane Wave Spectrum (PWS). Although it is possible to use the PO technique to calculate the PWS response as seen in [15], it is far more efficient to use an alternative technique instead: the Fourier Optics (FO) technique.

The Fourier Optics technique (FO) is based on an approximation of the PO radiation integral seen in Eq. 2.16. In the FO method, the PWS is calculated via an auxiliary surface, which is referred to as the FO-sphere seen in Fig. 2.2. Specifically, when our component of interest is illuminated by a plane wave, the field scattered toward its focal plane is evaluated on the FO-sphere using Geometrical Optics (GO). GO is a fast and accurate model for cases where the observation point is far from the focal point of the Quasi-Optical component.

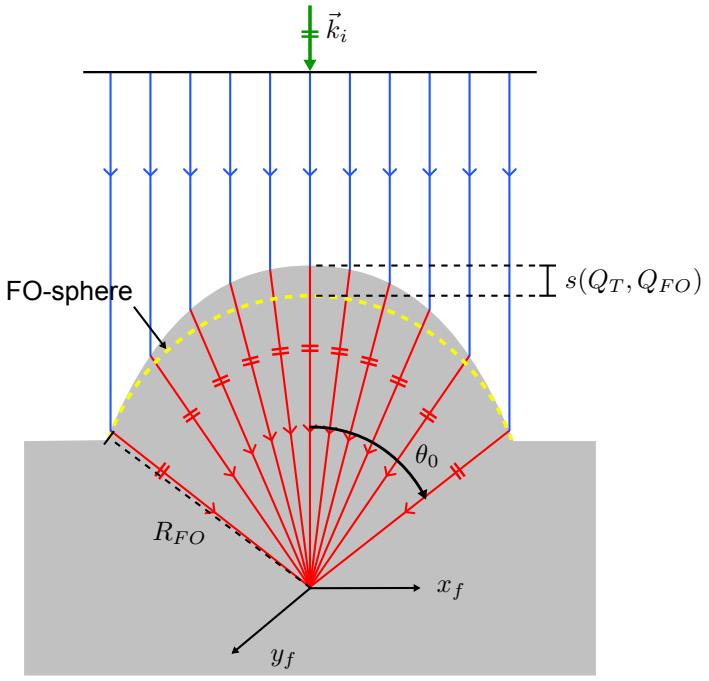

Fig. 2.2: An illustration of the GOFO model for an elliptical lens. The distance between the surface of the lens defined by Q_T and the FO-sphere defined by Q_{FO} with radius R_{FO} (shown as a dashed yellow line) is indicated as $s(Q_T, Q_{FO})$. The focal plane is described by x_f and y_f, where $(x_f, y_f) = (0, 0)$ is the focal point of the lens.

The electromagnetic field on this sphere is then referred to as the GO-fields, which is found using the GO technique described in detail in the following subsection. By applying a set of approximations on the amplitude, phase, and vectorial components of the radiation integral from the FO-sphere to the focal plane, a PWS can be defined [13]:

$$\vec{e}_f(\vec{\rho}_f) = \frac{e^{-jk\frac{|\vec{\rho_f}|^2}{2R_{FO}}}}{4\pi^2} \int_{\infty}^{\infty} \int_{\infty}^{\infty} \vec{E}^{FO} e^{jk_x x_f} e^{jk_y y_f} \, \mathrm{d}k_x \, \mathrm{d}k_y \tag{2.17}$$

where $\vec{e}_f$ is the focal field, $\vec{\rho_f} = x_f\hat{x} + y_f\hat{y}$ is defined for the coordinates on the focal plane of the Quasi-Optical component x_f and y_f, R_{FO} is the radius of the FO-sphere, and $\vec{E}^{FO}$ is a spectral field defined as:

$$\vec{E}^{FO}(k_x, k_y) = \frac{j2\pi R_{FO} e^{-jkR_{FO}}}{\sqrt{k^2 - (k_x^2 + k_y^2)}} \hat{r}' \times \left[\vec{E}^{GO}(k_x, k_y) \times \hat{r}'\right] \tag{2.18}$$

where $\vec{E}^{GO}(k_x, k_y)$ is the GO-field evaluated at the FO-sphere using the Geometric Optics technique.

The GO technique

The Geometric Optics technique is a technique used for high-frequency scattering scenarios. The technique approximates electromagnetic waves as tubes of rays propagating from one medium to another [16]. Because of this, Snell's law can be applied to the incoming field, such that the field on the FO-sphere of the lens, which can be seen in Fig. 2.2, can be represented by:

$$\vec{E}^{GO} = \vec{E}^{i} \cdot \bar{T}(Q_T) S_{spread}(Q_{FO}) e^{-jks(Q_{FO})} \tag{2.19}$$

where $\vec{E}^i$ is the incident plane wave evaluated on the lens surface Q_T, $\bar{T}$ is the transmission dyad, s is the propagation distance from the lens surface to the FO-sphere, and S_{spread} represents the spreading of the field due to the shape of the lens to the FO-sphere defined by Q_{FO}.

This GO-field, and in particular the spreading factor S_{spread} and added phase due to the path length $s(Q_{FO})$, can be calculated in two ways: analytically using a faster, but more crude approximation, or numerically using a raytracing technique. Both these techniques are described in detail in App. C. The advantage of the analytical GO technique is its speed. In case that the effect of the comma phase can be ignored [12], only the linear phase is assumed to play a major role once the lens is illuminated under an angle of incidence other than broadside. This linear phase term only applies a spatial offset to the focusing of the incoming field, allowing for very fast calculation of the pattern in reception, as the GO-field will only have to be calculated once for broadside incidence. Since the comma phase cannot be ignored for the cases discussed in this thesis, this approximation does no longer hold. Therefore, the numerical GO technique is employed due to its higher accuracy for off broadside incident angles.

2.3. Design Methodology

2.3.1. Absorber Design

The basis of designing an absorber, is designing a structure with an input impedance that matches to its background material, such that the power reflected on the background-absorber interface is minimised. When examining an arbitrary absorber as shown in Fig. 2.3, with the input impedance seen at the interface of the absorber expressed as $Z_{abs,in}$, one can calculate the reflected power on the interface via the reflection coefficient:

$$\Gamma_{abs} = \frac{Z_{abs,in} - Z_d}{Z_{abs,in} + Z_d} \tag{2.20}$$

According to this equation, in order to minimise the power reflected from the background-absorber interface, the input impedance $Z_{abs,in}$ of the absorber should be equal to the impedance of the absorber's background Z_d. Designing such a material which is also a superconductor (which is needed for the device to operate in an MKID), is not straight-forward. Therefore, some options for absorbing materials will be discussed in this section.

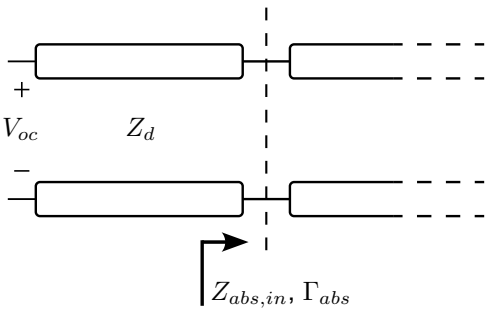

Fig. 2.3: A transmission line model illustrating a source, with voltage V_{oc} at the input of the stratification, propagating through the background material Z_d and transmitting into an absorber, which is defined as $Z_{abs,in}$ at the interface of the absorber

A possible solution for creating an absorbing layer is by choosing a dielectric material with a characteristic impedance close to that of Z_d. Issues with these types of materials is that the attenuation factor is usually very small. Thus, using such a material is difficult, as a very thick slab of dielectric is needed to absorb enough power. Moreover, power dissipated in a dielectric cannot be sensed by MKIDs. Instead, dielectric based absorbers require thermally coupled detectors, such as bolometers in the SCUBA-2 instrument, a large scale sub-millimeter camera operated a the James Clerk Maxwell Telescope in Hawaii [17].

Instead, a conductive material could be used. Since power is dissipated quickly in conductors through Ohmic losses, a layer can be used thinner than needed for dielectric materials. The issue with conductive materials, and especially metals, is that their resistivity is small, resulting in a complex surface

impedance at super-THz frequencies, with a relatively small real value and a significant imaginary value. The result is reflection of most of the incident power if a simple planar metallic thin film would be used.

The reflections on the conductor can be reduced by making the conductor very thin, smaller than the skin-depth of the material. While this solution can be effective for certain conductors, it should be noted here, that this solution is still challenging for conductors with a significantly small resisitivity, as the effective surface impedance will still have a large mismatch with the background material.

There are two problems with this solution. First of all, part of the power is transmitted through the material. This issue can be fixed using a $\frac{\lambda}{4}$-backing reflector. By adding an air-cavity of $\lambda/4$ thickness, and terminating this air-gap with a Perfect Electric Conductor (PEC), all power that passes through the conductor can be trapped between the conductor and the PEC, until all power has been absorbed. Due to this, theoretically, an absorber could be designed that absorbs 100% of the incoming power.

Adding a $\frac{\lambda}{4}$-backing reflector will not solve a second issue: the absorber is the inductive element of the absorber and must be made of a superconductive material such as Aluminium, as will be discussed in Sec. 2.3.3. Since Aluminium has a sheet resistance that is commonly small, usually below $1\Omega/\square$, matching the impedance of Aluminium to the one of its background, Z_d, is especially difficult. Other superconducting materials with higher resistivities are not possible for the demanding application of space: Aluminium MKIDs are by far the most sensitive [2].

To solve this, a more sophisticated design could be made from a conductive material. These designs allow for a tuneable impedance by changing certain dimensions of the design, such that it is possible to use a conductive layer as an absorber, while still maintaining the possibility to match to the background's impedance Z_d. A commonly used absorber design is a strip absorber, which can be seen in Fig. 2.4 [11].

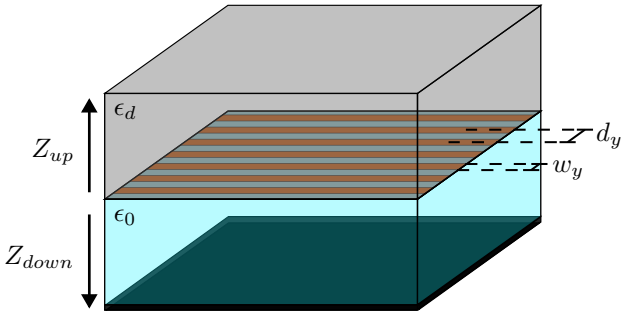

Fig. 2.4: The stratification of a stripline absorber, with the width of the lines and distance between the lines indicated as w_y and d_y, respectively, and the input impedances Z_{up} and Z_{down} as seen from the absorber

In order to match this absorber to Z_d, the line width and line spacing, w_y and d_y respectively, can be tuned. From [11], an approximate relation between the sheet resistance and dimensions of the absorber can be obtained:

$$R_s \approx \frac{w_y}{d_y} Z_{up} || Z_{down} \tag{2.21}$$

In the case of the scenario shown in Fig. 2.4, a perfect $\frac{\lambda}{4}$-backing reflector is used, leading to $Z_{down} = \infty$, and with $Z_{up} = Z_d$. This leads to a simplified equation for the strip absorber:

$$R_s \approx \frac{w_y}{d_y} Z_d \tag{2.22}$$

Evaluating this equation reveals an issue with designing strip absorbers for FIR detectors operating at frequencies $f \gg 1$ THz. Since a silicon lens is used, Z_d is approximately $Z_d \approx 111.5\Omega$. Due to the small sheet resistance of Aluminium ($R_s < 1\Omega/\square$), the fraction $\frac{w_y}{d_y}$ will be of the order of $1/100$. Since the distance between the lines is limited by half the wavelength in order to avoid higher-order Floquet

modes ($d_y \ll \lambda_d/2$), the lines will have to be very narrow: e.g. for 10 THz, with $\lambda_d = 30/sqrt(11.44) \simeq 9\mu\text{m}$, the distance between the lines will be roughly $d_y = 4.5\mu\text{m}$, and lines will be of the order of $w_y = 4.5/100 = 45\text{nm}$ wide. This does not only complicate the fabrication process, additionally it will complicate the design of MKIDs as thinner lines limit the MKID power handling capabilities. Moreover, at THz frequencies the imaginary component of the sheet impedance of Aluminium cannot be ignored, further complicating meeting the requirement on the strip's width.

Another issue with the strip absorber is that the absorber is only capable of absorbing a single polarisation by design. Although it is possible to design a dual polarised absorbed by stacking two of these absorber on top of each other, one rotated $90°$ with respect to the other, this does complicate the final design and fabrication.

Instead of a strip absorber, a more complicated design is employed here consisting of two meandering lines, of which a unit cell can be seen in Fig. 2.5 [10]. An advantage of this design over the strip absorber, is that it contains more tuneable parameters to achieve an impedance match with the background of the absorber. Since the meandering lines add additional capacitance into the structure, the added inductance by the wider lines can be countered more effectively. As an added advantage, the absorber is capable of absorbing both vertical and horizontal polarisations, due to the lines running both in horizontal and vertical directions.

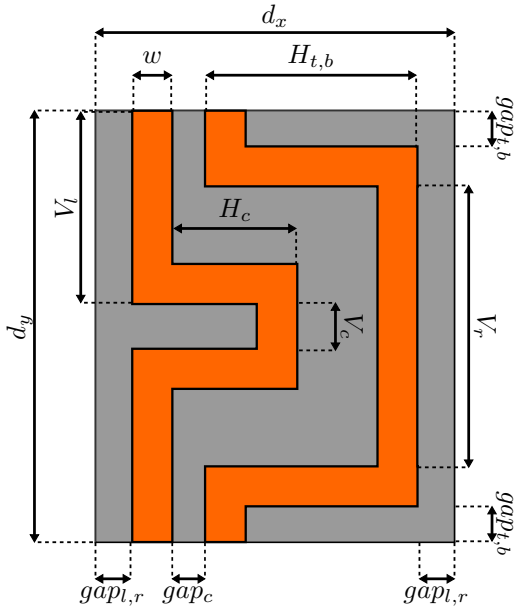

Fig. 2.5: Definition of the dimensions in a unit-cell of a meandering line absorber

Designing a meandering line absorber

As described, analytical expressions were obtained in previous works for strip absorbers to design geometrical parameters to match the input impedance to the characteristic impedance of the background, as seen in Eq. 2.22. However, there is currently no analytical expression available for the meandering line absorber. Equivalent circuit models have been made for single meandering lines, as seen in [10] and [18], however, these models are not equivalent for the dual meandering line absorber and as such can not be applied to design the absorber for this project. Thus, the designs shown in this work were made by simulating the performance of the absorber using unit cell boundaries in CST [19].

Simulating the absorber in commercial numerical solvers such as CST is a time consuming process, which we speed up by the following simplifications: instead of simulating the absorber in a time domain simulation, the devices were simulated using a frequency domain solver and fed by a single plane wave. This provides the possibility to simulate the device as if it is an array of infinite size. To further limit the simulation costs, the simulator was limited to only take into account the first 2 Floquet modes: TE_1 and TM_1. As long as the designs had a periodicity much smaller than $\lambda/2$, higher order Floquet modes were avoided, and thus did not have a significant impact on the performance of the device.

From this simulation, the Z- and S-parameters of the absorber design were extracted. These were used for two specific goals. First of all, the Z-parameters were used to determine the input impedance of the absorber. The input impedance, which will vary for TE and TM polarisations, should each be as closely matched to Z_d as possible, as stated at the start of this subsection. Therefore, the Z-parameters were used as an indication of how much the design should be modified in order to reach a better match to the background material.

Matching this input impedance isn't as straightforward as increasing or decreasing the length of one of the line sections in Fig. 2.5. As each line section is also imposing an imaginary impedance on neighbouring line sections, through capacitive coupling for example, changing the design for TE polarisation will also impact the impedance for TM polarisation, and vice versa. Because of this, it makes more sense to view the absorber as a resonant circuit, instead of a simple impedance, and design accordingly.

Secondly, the extracted Z- and S-parameters were used to calculate a set of performance parameters that describe the quality of the designs:

- The absorption efficiencies at the design frequency f_0: $\eta_{abs,TE}$ and $\eta_{abs,TM}$
- The average absorption efficiency at f_0: $\eta_{abs,avg}$
- The bandwidth of $\eta_{abs,avg}$: BW

These parameters were extracted by evaluating the response of the unit cell design to a plane wave at broadside incidence. The absorption efficiencies, $\eta_{abs,TE/TM}$, have been calculated from the extracted S-parameters of the absorber according to the following equations:

$$\begin{aligned} \eta_{abs,TE} &= 1 - |S_{TETE}|^2 - |S_{TMTE}|^2 \\ \eta_{abs,TM} &= 1 - |S_{TMTM}|^2 - |S_{TETM}|^2 \\ \eta_{abs,\text{avg}} &= \frac{\eta_{abs,TE} + \eta_{abs,TM}}{2} \end{aligned} \tag{2.23}$$

where S_{TXTY} represents the S-parameters for an excitation at the TY Floquet port and observing the reflected voltage at the TX port.

2.3.2. Lens-Absorber Design

Each absorber had to be integrated into an appropriate lens design. The design of the complete lens-absorber comes in two parts: the design of the lens, and the physical, finite size of the absorber.

Lens design

The canonical integrated lens geometry to focus radiation on a minimised spot size is an elliptical lens. Elliptical lenses have the advantage that each ray is focused into the same focal point, where other lenses, such as spherical lenses, have different focal points for each incoming ray. For elliptical lenses, there are 3 independent parameters that can be tuned: its material, its diameter D_{lens}, and the f-number of the lens $f_{\#}$. As for the material, only high resistive silicon is an acceptable option at THz frequencies, due to its significantly low losses and stable cryogenic behaviour.

The lens-absorbers that have been designed in this thesis have one primary goal: show the advantages and feasibility of lens-absorbers in future FIR missions across a frequency band as defined by the POEMM and PRIMA missions. Because of this, instead of putting the focus of the design of the detectors on coupling directly to the optical system of one of these missions, the main focus is on designing detectors to couple well to the measurement setups available at SRON.

Due to these measurement setups, the requirement was set to design lens-absorber arrays with a pitch that approaches 1.4mm-1.5mm. Therefore, lenses have been designed that have a $D_{lens} \rightarrow 1.4$mm, which is approximately $7\lambda_0$ at 1.5 THz.

This leaves a second parameter, the f-number $f_{\#}$, that had to be tuned. The f-number impacts two aspects of the lens-absorber: ease of fabrication, and the angular region at the incident field that falls on top of the absorber.

When investigating the response of an absorber to plane waves from various incident angles θ_i, as seen in Fig. 2.6, two important effects can be observed. First of all, a noticeable null appears for plane waves with a TM polarisation under an incident angle close to 17 degrees, due to the critical angle at the silicon-air interface. Secondly, selecting a region below 17 degrees also provides a response of the absorber that is rather flat versus angle of incidence. As highlighted in Fig. 2.6, the angular region for a lens with an f-number of 2 is approximately equal to $\theta_0 = \sin^{-1}\left(\frac{1}{2f_\#}\right) \approx 14.48°$, which is right before the null due to the critical angle of Silicon. Therefore, a lens was selected with an f-number close to 2, that offers a rather flat response to the incoming field of the lens.

Apart from offering a flat response in the absorption pattern of the absorber, an f-number of 2 also provides a shallow lens which, in turn, simplifies the fabrication process.

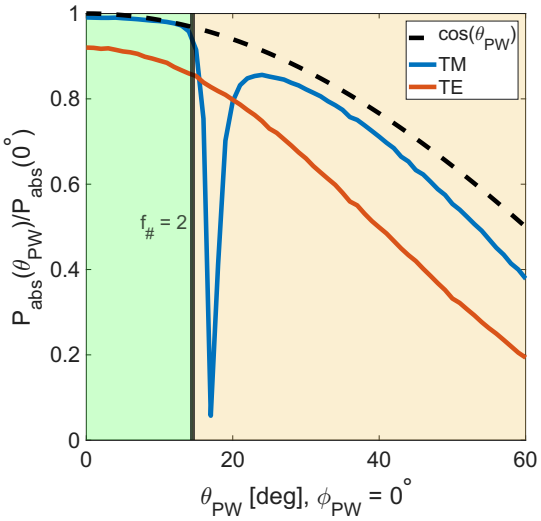

Fig. 2.6: The plane-wave response of one of the absorbers designed in this thesis, made with 21nm Aluminium and a line width of $0.6\mu\text{m}$. Both the response to TM and TE polarisations have been plotted, compared with a $\cos\theta_{PW}$ curve. Two regions have been highlighted: a green region that would by captured by a lens with an f-number of 2, and an orange region outside of the angular region of the lens.

Design of the absorber size

In Sec. 2.3.1 the absorption efficiency was optimised for an infinite absorber. In the case where the absorber is coupled to a Quasi-Optical component, such as an elliptical lens, the physical size of the absorber (which is the absorber side-length in case of an absorber with a rectangular pitch) affects two major performance parameters of the integrated lens-absorber device: the *aperture efficiency* (η_{ap}), which describes the power capturing capabilities of the detector when the lens is illuminated by a plane wave, and the *focusing efficiency* (η_f), which describes how well the detector is capable of distinguishing point sources, in other words, how narrow the angular response of the detector is with respect to ideal benchmarks, i.e. a perfect airy pattern.

The aperture efficiency is defined as follows:

$$\eta_{ap}(f, \theta_i, \phi_i) = \frac{P_{abs}(f, \theta_i, \phi_i)}{P_{in}} \tag{2.24}$$

where P_{abs} is the power absorbed by the absorber, and P_{in} is the total power incident on the aperture defined by the lens surface area. Consider an ideal absorber placed at the focal point of a lens. As the absorber is ideal, the total field on the absorber defined in Eq. 2.13 is equal to the direct field of the lens, thus the field captured by the absorber equals the field that lands in the domain of the absorber:

$$P_{abs} = \frac{1}{2\eta_d} \iint_{-w/2}^{w/2} |\vec{e}_{d,x}|^2 + |\vec{e}_{d,y}|^2 \, \mathrm{d}x_f \, \mathrm{d}y_f \tag{2.25}$$

where η_d is the characteristic impedance of the Silicon of the lens, $\vec{e}_{d,x/y}$ are the direct fields landing on the absorber, and w is the side length of the absorber. Thus, as the size of the absorber increases, more power is captured, increasing the aperture efficiency of the lens-absorber.

For the focusing efficiency the situation is the opposite. Consider the case of an ideal absorber again. As the size of the absorber increases, power from larger angles compared to broadside can be captured by the absorber as it still lands within the domain of the absorber. Thus, not only sources from the intended direction (e.g. broadside) might be captured, but other sources that are not of interest might be captured as well.

This behaviour is described in [12] by dividing a larger absorber into a combination of smaller absorbers, similar to the multi-mode antenna defined in [20]. The power received by each of these smaller devices sum up incoherently, resulting in a less angular discriminating device.

The effect of this, which is defined as a lower focusing efficiency, is the widening of the far-field pattern of the detector. This is illustrated in Fig. 2.7, where the pattern in reception is shown for various array sizes, which is also confirmed in [12]. In the figure, it can be observed that a larger absorber leads to a pattern in reception that resembles a wide sinc shape, while a small absorber will approach an airy pattern.

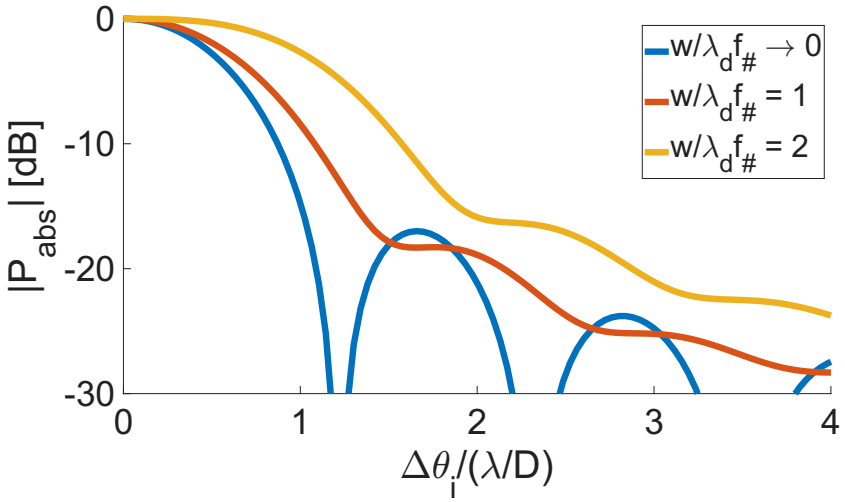

Fig. 2.7: Normalised patterns in reception for a lens-absorber with 3 different side-lengths. The patterns widen the larger the side-length of the absorber gets, reducing the focusing efficiency.

Thus, as the ideal focusing case is defined by an airy pattern, the focusing efficiency describes how close the actual pattern in reception is to an airy pattern, and is defined as [12]:

$$\eta_f(f) = \frac{\Omega_{airy}}{\Omega_0} \tag{2.26}$$

where Ω_{airy}, the ideal solid angle of the Airy pattern, is compared to the solid angle of the detector Ω_0. These solid angles are defined as:

$$\begin{aligned} \Omega_{airy} &= \frac{\lambda^2}{A_{lens}} \\ \Omega_0 &= \int_0^{2\pi} \int_0^{\frac{\pi}{2}} F(f,\theta,\phi) \sin\theta \, \mathrm{d}\theta \, \mathrm{d}\phi \end{aligned} \tag{2.27}$$

where A_{lens} is the aperture area of the lens, and $F(f,\theta,\phi)$ is the normalised lens absorber pattern, defined as:

$$F(f, \theta_i, \phi_i) = \frac{P_{abs}(f, \theta_i, \phi_i)}{\max\{P_{abs}(f, \theta_i, \phi_i)\}} \tag{2.28}$$

There is a clear trade-off between the aperture efficiency and focusing efficiency for the width of the device. In order to have a good performance in term of aperture efficiency, the focusing efficiency will drop drastically due to its major dependence on the side length of the absorber. The trade-off for the side length of the device is worse than for antennas, which will not couple properly to fields not directly focused onto the antenna. This confirms both an advantage and disadvantage of the absorber over the antenna, absorbers can still couple well to incoming fields when the lens-absorber are slightly misaligned, while the performance of antennas will drop drastically. However, this comes at the cost of focusing capabilities of the detector.

Although focusing efficiency is an important parameter for the future missions, the aperture efficiency has a higher priority for this thesis. Therefore, the design was optimised with aperture efficiency in mind.

Matching layer design

A major issue with using a material such as silicon ($\epsilon_r = 11.44$) for the lens, is the large impedance mismatch between free-space and the lens. Due to this impedance mismatch a large part of the incoming field is reflected from the surface of the lens. A common method used to reduce the reflections on the lens, is by adding a quarter wavelength matching layer, such as Parylene-C with $n = 1.62$ [21]. By adding a layer of a material with a relative permittivity close to $\epsilon_m = \sqrt{\epsilon_r}$, and a thickness of $\lambda_m/4$, where λ_m is the wavelength in the material of the matching layer, the lens can be impedance matched to free-space reducing the reflections drastically.

There are two major issues with this solution, the first being the bandwidth of the matching layer. As the layer is designed to have a thickness of $\lambda_m/4$, the bandwidth is limited. For a frequency slightly off the design frequency, the thickness of the layer will no longer allow an impedance match with free space. Multiple solutions are available to increase the bandwidth, where one of the most common solutions is replacing the single matching layer by multiple matching layers [22] and [23]. With this technique, the matching can be done more gradually, leading to a matching layer that is less frequency dependent. However, none of these are applicable to the THz region due to the high dielectric losses at super-THz frequencies.

Moreover, this does not solve a second issue. The absorber is read-out using MKIDs, which are devices built upon superconducting principles. In order for these devices to work, the lens-absorbers will have to be placed in a cryo-chamber and cooled to low temperatures. As the temperatures change, different materials will start to shrink at different rates. This will cause the matching-layers to simply fall off the lens, especially after putting the detectors through multiple cooling cycles.

To mitigate this risk, a matching-layer is employed that uses geometric properties to match to free-space instead of material properties. This way, the matching layer can be made out of the same material as the lens, avoiding the matching layer falling off the lens when cooled. A solution to this is a so called frusta layer [24] and [25]. This matching layer uses pyramid like structures to match the lens to free-space. This matching layer can be made by cutting the pyramids into the surface of the lens, from the same substrate as the lens itself instead of a different material. Another advantage of this matching-layer is its broadband behaviour [24], solving both issues introduced by the single quarter wavelength matching layer. Therefore, in this thesis, a scaled-down version of the design presented in [24] is used in the lens design equipped with a matching layer.

2.3.3. Absorber-MKID Design

One of the important instruments on the missions described in this thesis, is the imaging spectrometer. By combining multiple of the lens-absorbers designed in this thesis, and aligning them along a 2D grid, the detectors can be used to perform imaging along one axis of the lens-absorber array, while performing spectroscopy along the other axis. In order to get high resolution data from the instruments, a high number of lens-absorbers will be employed in the final array design, both in the spectral as well as the spatial direction.

Although an imaging spectrometer at FIR would offer great insight into the formation of stars, planets, and the galaxy us humans reside in, it does pose a technical problem. Reading out a high number of detectors can be problematic, using an individual read-out line and its associated circuitry per detector is not feasible, and sticking to conventional multiplexing techniques adds additional design complications due to the need of additional electronic components. Combining this with the fact that sensitivity becomes a major issue at these frequencies: for a background-limited space telescope it has been shown that a Noise Equivalent Power (NEP) of $3 \cdot 10^{-20}\ \mathrm{W}/\sqrt{\mathrm{Hz}}$ is required for detector arrays with a pixel count of $\approx 10^5$ [1] and [26], a more sophisticated read-out design is needed.

As shown in [2], a solution to this problem is the use of Microwave Kinetic Inductance Detectors (MKID). MKIDs have shown to offer capabilities of multiplexing a large number of detectors with a good sensitivity in the order of NEP $\approx 3 \cdot 10^{-20}\ \mathrm{W}/\sqrt{\mathrm{Hz}}$ [2].

Microwave Kinetic Inductance Detectors

MKIDs are superconductive devices that operate on the basis of Cooper pairs, which are electron-pairs at the Fermi energy that form once superconductive materials are brought below their critical temperature T_c [27]. The transport of charge in conductors can be described by a resistance due to electrons in the material, and a kinetic inductance L_k due to the kinetic inertia of electrons in the material. In superconductors, this kinetic inductance dominates. The superconductor can be respresented by the equivalent circuit shown in Fig. 2.8a. Power can be absorbed in a superconductor for photon energies exceeding the gap energy of ($E_{gap} = 2\Delta$ [27]), which will cause Cooper pairs to break. This will change the number of Cooper pairs and quasiparticles in the material, leading to a change in the kinetic inductance and resistance of the material. Although the change in the kinetic inductance is small, this pair-breaking effect can be used by creating a resonator, as seen in Fig. 2.8b, which allows us to precisely read the amount of power absorbed by the detector.

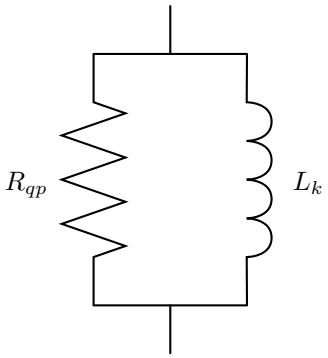

(a) Circuit model of a superconductive film, consisting of a resistance R_{qp} due to quasiparticles and a kinetic inductance L_k due to the inertia of quasiparticles

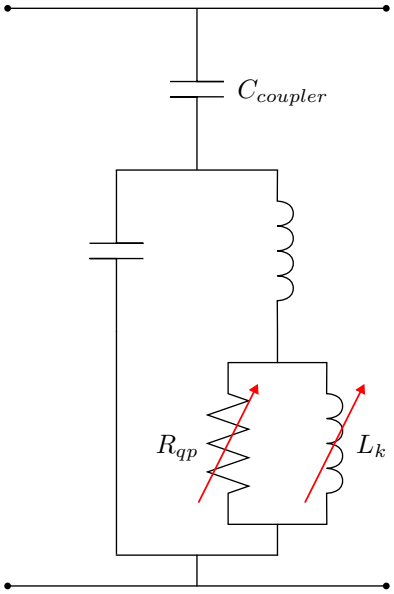

(b) A superconductive film employed in an MKID, which is a resonator capacitively coupled to a feeding line

Fig. 2.8: Circuit models used to represent a superconductive film in an MKID

Usually, the superconductive resonator is capacitively coupled to a read-out line. This turns the resonator into a band-stop filter with a resonance frequency f_{MKID} and with a quality factor Q, which will both vary as power is absorbed by the detector as illustrated in Fig. 2.9. For each detector, the f_{MKID} can be precisely designed, such that each detector has its own distinguishable resonance frequency. Due to this, a high number of detectors can be coupled to a single read-out line, leading to an output consisting of various dips in the frequency domain, allowing MKIDs to be used to create frequency domain multiplexing with a high multiplexing factor.

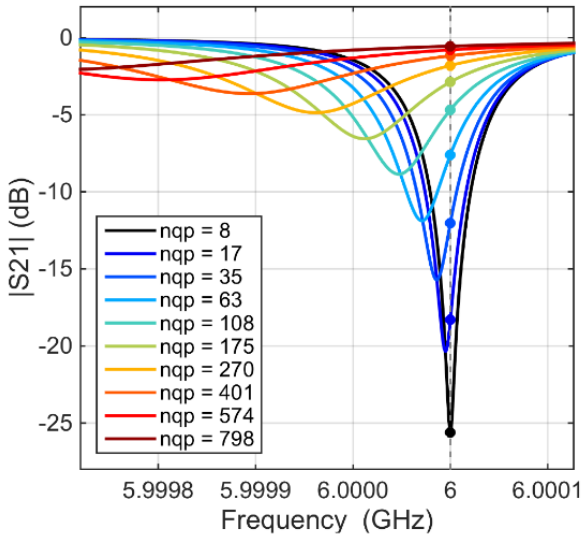

Fig. 2.9: The transmission of an MKID changing as the number of quasiparticles changes in the superconductive materials once power is absorber by the MKID [28].

Detector Design

An MKID consists of a superconductive resonator, where the inductive part is realized by the discussed absorber, and the capacitive part is realized by a transmission line connected to the absorber. Although MKIDs can be made using a single superconductor, it is beneficial to design MKIDs in a Hybrid form: consisting of two different superconductive materials. As shown in [27], when selecting a superconductor, there is often a trade-off between performance parameters of MKIDs, such as the sensitivity and noise performance. Using Aluminium for example offers a higher sensitivity, while NbTiN offers lower noise. To achieve best of both worlds, these two materials can be combined: NbTiN is used at the capacitive end of the MKID (the transmission line), which is coupled to the read-out line, while the Aluminium section is used on the inductive end of the MKID (the absorber), which is placed at the focal plane of a lens. This configuration ensures an MKID with low noise, as the capacitive end of MKIDs is more sensitive to noise, and a higher sensitivity to quasiparticles as power is absorbed in the Aluminium section and thus most current resides in the absorber. This configuration also offers a second advantage due the difference in energy gap between NbTiN and Aluminium. Due to the gap difference, quasiparticles are confined to the Aluminium section where the sensitivity is highest.

The Hybrid MKID design can be used for both antennas as well as absorbers, as seen in Fig. 2.10. The difference between the two designs, is the additional Aluminium line required in the antenna case seen in Fig. 2.10a. Since power is not absorbed by the antenna itself, the Aluminium line is needed to absorb the power from the field that is received by the antenna. Since the absorber is capable of capturing power, power is absorbed in the material of the absorber itself. Thus, as seen in Fig. 2.10b, the absorber is made from the superconductive Aluminium and connected directly to the NbTiN line, as Cooper pairs will be broken in the absorber itself.

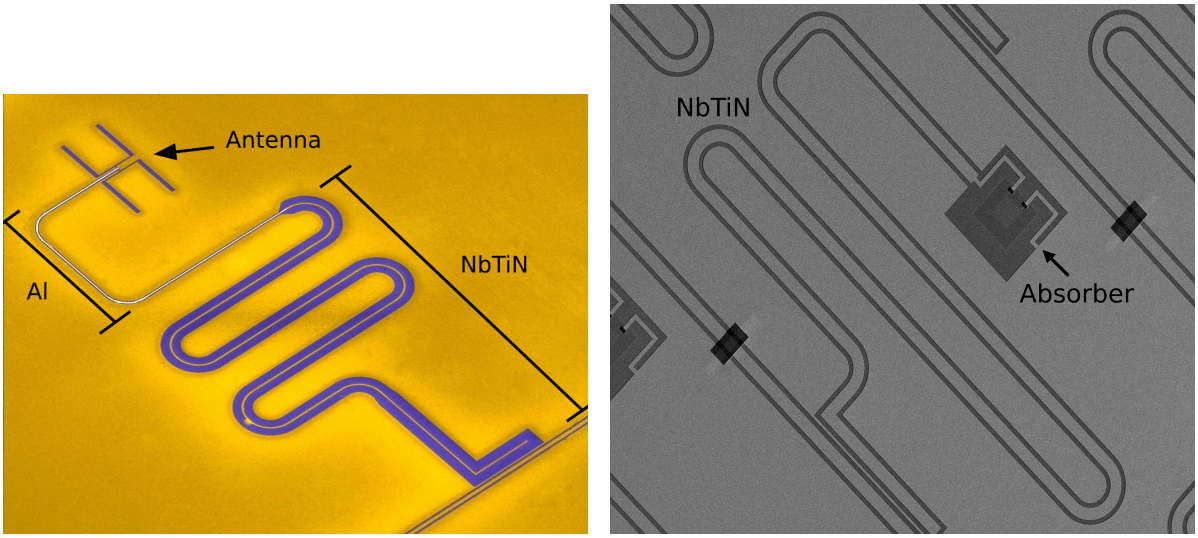

(a) Antenna coupled MKID

(b) Absorber coupled MKID

Fig. 2.10: SEM pictures of two MKIDs coupled to an Antenna and an Absorber

2.3.4. MKID Resonant Frequency Design

As stated earlier in this section, multiple MKIDs can be read-out and multiplexed by designing each of the MKIDs with a different resonance frequency f_{MKID}. Resonance takes place when the input impedance of the structure becomes real and the imaginary part approaches zero. Thus, in order to tune an MKID to resonate at f_{MKID}, a design should be made where $\Im\left(Z_{MKID,in}\left(f_{MKID}\right)\right) = 0$. Observe the MKID shown in Fig. 2.11, the MKID can be split into two parts: the NbTiN transmission line, and the absorber structure connected to it. The input impedance of the two parts can be investigated at their interface and described by the input impedance of the transmission line $Z_{TL,in}$ and the input impedance of the absorber structure $Z_{abs,in}$ for guided waves at GHz frequencies, the latter of which should not be confused with the impedance to a plane wave at THz frequencies. Therefore, in order to obtain resonance at f_{MKID}, the imaginary parts of these input impedances combined should approach zero, and thus $\Im\left(Z_{abs,in}\right) = -\Im\left(Z_{TL,in}\right)$.

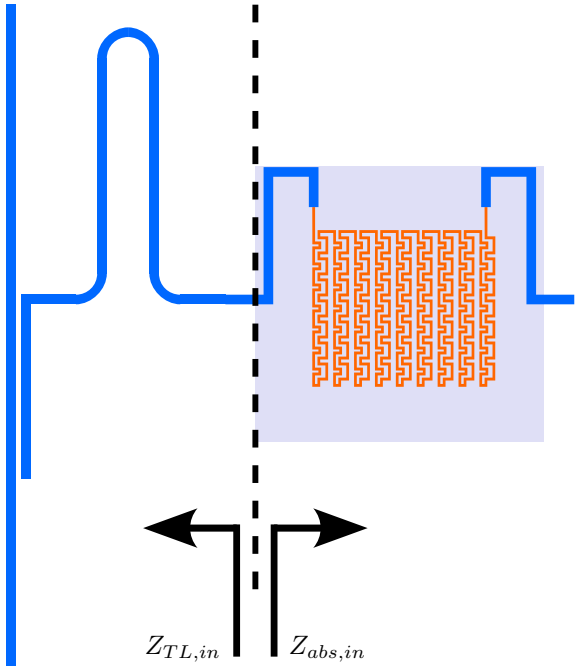

Fig. 2.11: An illustration of an absorber coupled MKID, consisting of a NbTiN transmission line (given in blue) coupled to a read-out line on the left, and the absorber structure on the right, consisting of 2 NbTiN feeding lines connected to the Aluminium meandering line absorber (given in orange). The input impedances of the transmission line and absorber structure, as seen at their interface, have been indicated by $Z_{TL,in}$ and $Z_{abs,in}$, respectively.

The microwave input impedance of the absorber structure depends on the design of the absorber. Since the design was optimised to absorb incoming propagating waves, the absorber geometry is fixed. Thus, its microwave impedance is fixed and the only impedance that remains tuneable, is the input impedance of the NbTiN transmission line $Z_{TL,in}$. It is known that the input impedance of a transmission line can be described by

$$Z_{TL,in} = Z_{TL}\frac{Z_L + jZ_{TL}\tan\left(\frac{2\pi f}{v_p}l\right)}{Z_{TL} + jZ_L\tan\left(\frac{2\pi f}{v_p}l\right)} \tag{2.29}$$

where Z_{TL} is the characteristic impedance of the employed transmission line used, v_p is the phase velocity in the transmission line, l the length of the transmission line, and Z_L is the load attached at the end of the transmission line. The transmission line section of the MKID can be either open or short circuited, however the transmission lines used in this thesis are open, leading to a load impedance equal to $Z_L = \infty$. Due to this, the equation can be rewritten to

$$Z_{TL,in} = Z_{TL}\frac{1}{j\tan\left(\frac{2\pi f}{v_p}l\right)} = -jZ_{TL}\cot\left(\frac{2\pi f}{v_p}l\right) \tag{2.30}$$

Following the equality of $\Im\left(Z_{abs,in}\right) = -\Im\left(Z_{TL,in}\right)$, the equation above can be rewritten to obtain an expression for the length of the transmission line as

$$l = \frac{v_p}{2\pi f_{MKID}}\cot^{-1}\left(\frac{\Im\left(Z_{abs,in}\right)}{Z_{TL}}\right) \tag{2.31}$$

So, for a given input impedance of the absorber structure, the characteristic impedance of the transmission line, and the resonance frequency of the MKID, the length of the transmission line can be determined.

To obtain the input impedance of the absorber structure, the different absorber designs, each with their unique unit cell designs and absorber widths, were simulated in Sonnet [29]. For each of these designs the absorbers were recreated in Sonnet using an absorber structure such as the one seen in Fig. 2.11, resulting in the structure seen in Fig. 2.12. The input impedance is evaluated at port 1 connected to the CPW line seen in Fig. 2.12

Using this frequency dependent input impedance, and the characteristic impedance of the CPW transmission line, the lengths of the NbTiN transmission lines could be calculated for each of the resonance frequencies of interest.

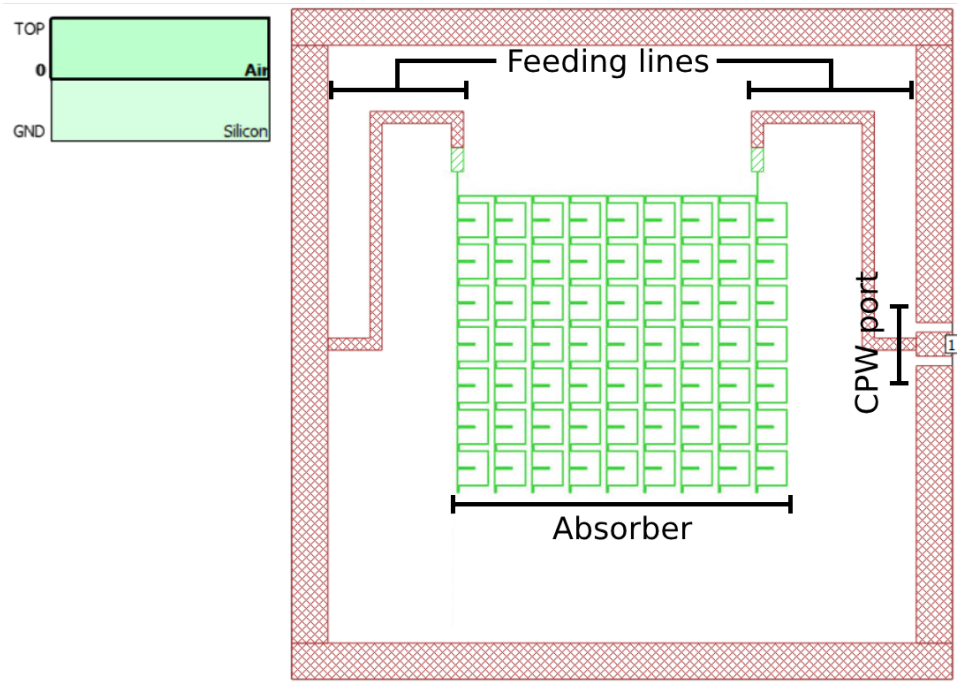

Fig. 2.12: An absorber structure for one of the absorbers designed in this thesis (right), and the used stratification (left) to simulate the structure in Sonnet. The green coloured material is Aluminium, and the red coloured material is NbTiN. The input impedance of the structure is simulated at the CPW port indicated by the number 1 on the right side. The structure will be connected via this port to a CPW NbTiN transmission line, and is connected to ground on the left side.

2.4. Detector Designs and Performance

2.4.1. Materials and Guidelines

One of the main subjects of this chapter, is investigating the feasibility of designing lens-absorbers to operate at 1.5 THz. An important part of this feasibility study is related to the manufacturability of the lens-absorbers. Therefore, two important parameters that impact fabrication limitations in the unit-cell designs of the absorbers were selected: the width and thickness of the meandering lines.

As stated in Sec. 2.3.3, the absorbers have been designed using Aluminium as the absorbing material, to provide the capability to integrate the absorbers in MKIDs. A number of different depositions of Aluminium have been measured at SRON in the past, each with their own thickness and resistivity. Two material thicknesses were selected from this dataset, in order to investigate the effect of material thickness on the performance of the absorbers.

In order to select possible line widths, previously in-house fabricated Aluminium structures were investigated. $0.3\mu\mathrm{m}$ wide lines have been fabricated in the past, however, at the time of designing the absorbers, the yield of these detectors was relatively low. In addition to this, narrower Aluminium lines lead to lower power handling capabilities in MKIDs, which in turn affects the sensitivity of the detector. Therefore, two line widths slightly wider than $0.3\mu\mathrm{m}$ have been selected, leading to a final 2-by-2 design matrix consisting of the parameter values shown in the table below.

Thickness (Resistivity ρ)	$21\mathrm{nm}\ (35.9\mathrm{n}\Omega\cdot\mathrm{m})$	$28\mathrm{nm}\ (17.4\mathrm{n}\Omega\cdot\mathrm{m})$
Line width	$0.6\mu\mathrm{m}$	$1.3\mu\mathrm{m}$

Tab. 2.1: Different parameters and values for which absorbers have been designed. Since these parameters lead to a 2-by-2 design matrix, a total of 4 different designs have been made

To get a better understanding of the differences between two different Aluminium thicknesses, the sheet impedance can be calculated for each of these Aluminium thicknesses using [30]

$$Z_s = \frac{1+j}{\sigma\delta}\coth\left(\frac{(1+j)\,d}{\delta}\right) \tag{2.32}$$

where σ is the conductivity of the material (which is equal to the inverse of the resistivity $\sigma = \frac{1}{\rho}$), δ is the skin-depth of the material defined in terms of angular frequency (ω): $\delta = \sqrt{\frac{2}{\omega\mu_0\sigma}}$, and d is the thickness of the material. Eq. 2.32 is basically defined by the kinetic inductance of the electrons in the material. This equation was used to produce the results shown in Fig. 2.13 below.

For the frequency range of interest, Fig. 2.13 shows that the change in sheet resistance versus frequency is near constant up to 4 THz, while the sheet reactance increases for higher frequencies. Thus, as expected, the sheet impedance is mostly inductive, which presents itself as a higher and positive reactance when increasing the frequency in the metal. Although the difference in sheet reactance between the two thicknesses is rather small, the sheet resistance is about 2.5 times larger for the thinner Aluminium. This means that matching the absorber to Silicon is easier, as the reactance will not be as prominent as for the thicker Aluminium.

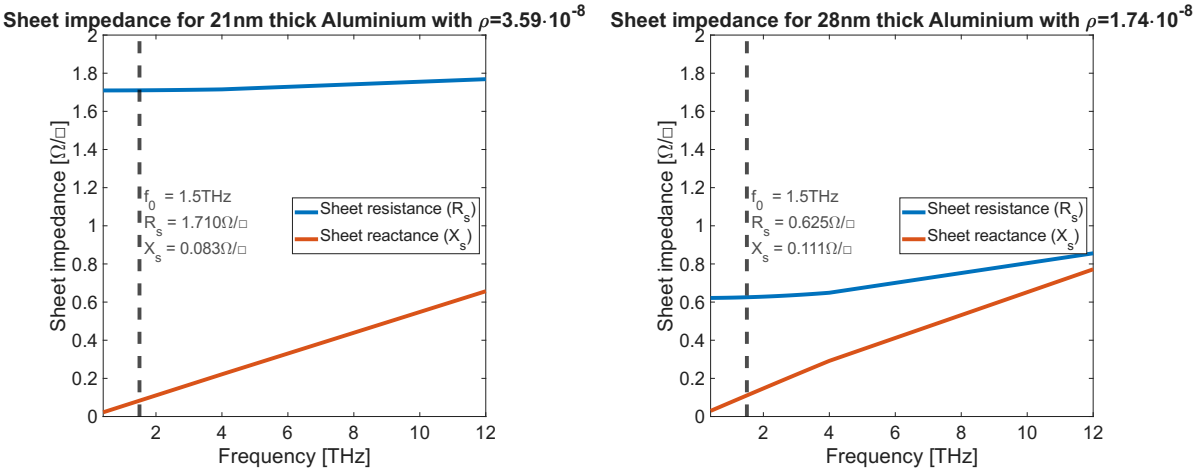

(a) Sheet impedance of $21\mathrm{nm}$ thick Aluminium

(b) Sheet impedance of $28\mathrm{nm}$ thick Aluminium

Fig. 2.13: Sheet impedance ($Z_s = R_s + jX_s$) of the two materials used to design the absorbers presented in this thesis

2.4.2. Absorber Designs

A total of 4 meandering-line absorber designs with quarter wavelength backing reflectors have been optimised in CST based on the different parameter values presented in Fig. 2.5. The designs have been optimised for the absorption efficiencies for TE and TM polarisations, as discussed in Sec. 2.3.1. Since no particular design strategy is available as of writing, a number of observations have been presented in Tab. 2.2 that can aid in future designs of the type of meandering line absorber presented in this thesis.

Dimension	**Change in** f_{TE}	**Change in** f_{TM}	**Change in** $\max(\eta_{abs,TE})$	**Change in** $\max(\eta_{abs,TM})$
$H_{t,b}$	- - - -	-	- -	+++
H_c	- -	- -	+	- - - -
V_r	- - -	- - -	- -	++
V_c	~	-	+	- -
gap_c	-	++	-	- -
$gap_{t,b}$	~	- - -	-	~
$gap_{l,r}$	+++	~	+	-

Tab. 2.2: A visual representation of the impact of changing certain unit-cell parameters on the performance parameters of the design. f_{TE} and f_{TM} represent the resonance frequencies of the structure for TE and TM polarisation, respectively. $\max(\eta_{abs,TE})$ and $\max(\eta_{abs,TM})$ represent the absorption efficiencies of TE and TM polarisations at the resonance frequency of the structure. The findings reported here indicate the effect after increasing the mentioned dimension, and indicates how much a parameter increases (indicated by the number of +), decreases (indicated by the number of -), or stays relatively the same (~).

One key observation to point out, relates to specifically tuning the impedance of only TE or TM polarisation. Although most unit cell dimensions impact coupling to multiple different line sections, the gaps surrounding the unit cell offer more specific control over either TE or TM polarisations. This is particularly useful in the case where the peaks of the absorption efficiencies for TE and TM are both moved away from the design frequency in opposite directions. Tuning the gaps on the sides of the unit cell offers the possibility to move both peaks close to the same frequency. An example of this is shown in Fig. 2.14, where an arbitrary, unoptimised design is shown in Fig. 2.14a with good performing peak efficiencies, located away from the design frequency. After increasing the gap-sizes from $1.4\mu\mathrm{m}$ to $2.4\mu\mathrm{m}$ horizontally and $2.6\mu\mathrm{m}$ vertically, the result in Fig. 2.14b is obtained. The peaks have been moved to the same design frequency.

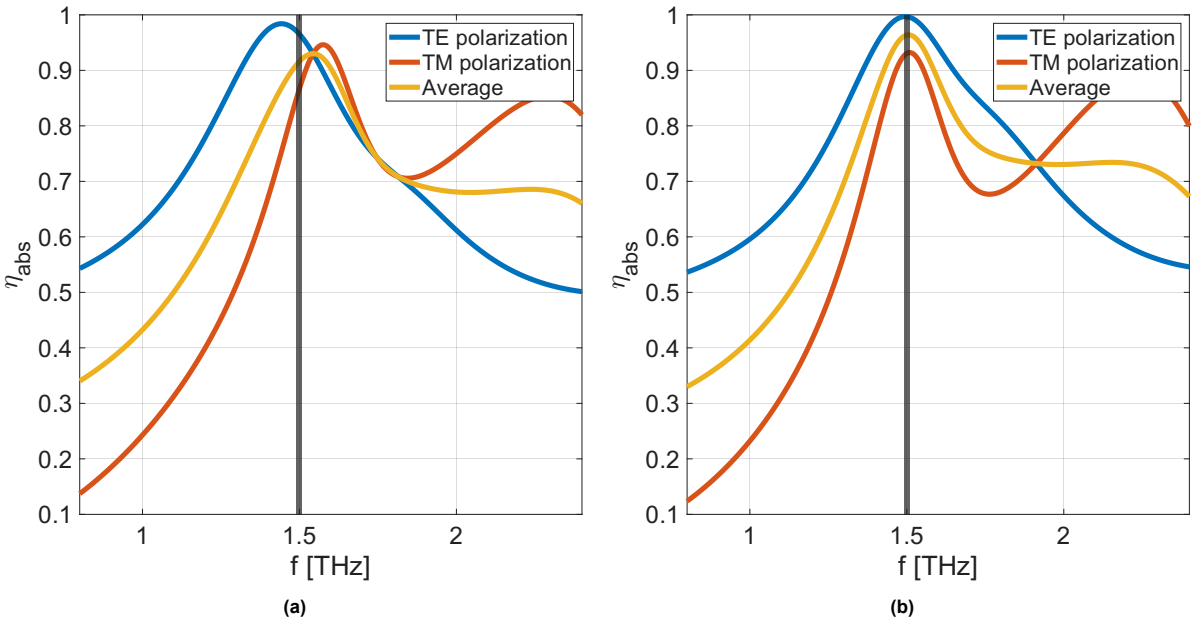

Fig. 2.14: The absorption efficiency versus frequency for an absorber design before and after increasing the gaps surrounding the unit cell. The figure highlights the resonance frequency tuning capabilities by tuning the gap sizes $gap_{t,b}$ and $gap_{l,r}$ around the unit cell, and shows the absorption efficiency curves (a) before tuning, and (b) after tuning the gap sizes.

Using the observations presented above, and by studying the effect of each change on the input impedance of the absorber, 4 absorbers designs have been created (see App. F for the complete design descriptions). For each of these designs, the absorption efficiency for broadside incidence versus frequency is shown in Fig. 2.15. For each of the designs, the attempt was made to design the resonances of both TE and TM polarisations at the same design frequency. Although shifting these peaks away from the design frequency could slightly improve the bandwidth of the average absorption efficiency, the decision was made here to improve the performance of TE and TM polarisations individually.

Two major performance criteria can be studied when investigating the curves shown in Fig. 2.15: the absorption efficiencies at 1.5 THz, and the bandwidth of the design. For both of these criteria, a clear relation between the two design parameters (line width and thickness) is visible. Choosing a design with thicker material and wider lines offers a significant amount of control over the peak efficiency, leading to a high absorption efficiency. The bandwidth does suffer for these design parameters, which is much larger when opting for thinner material and lines that are narrower.

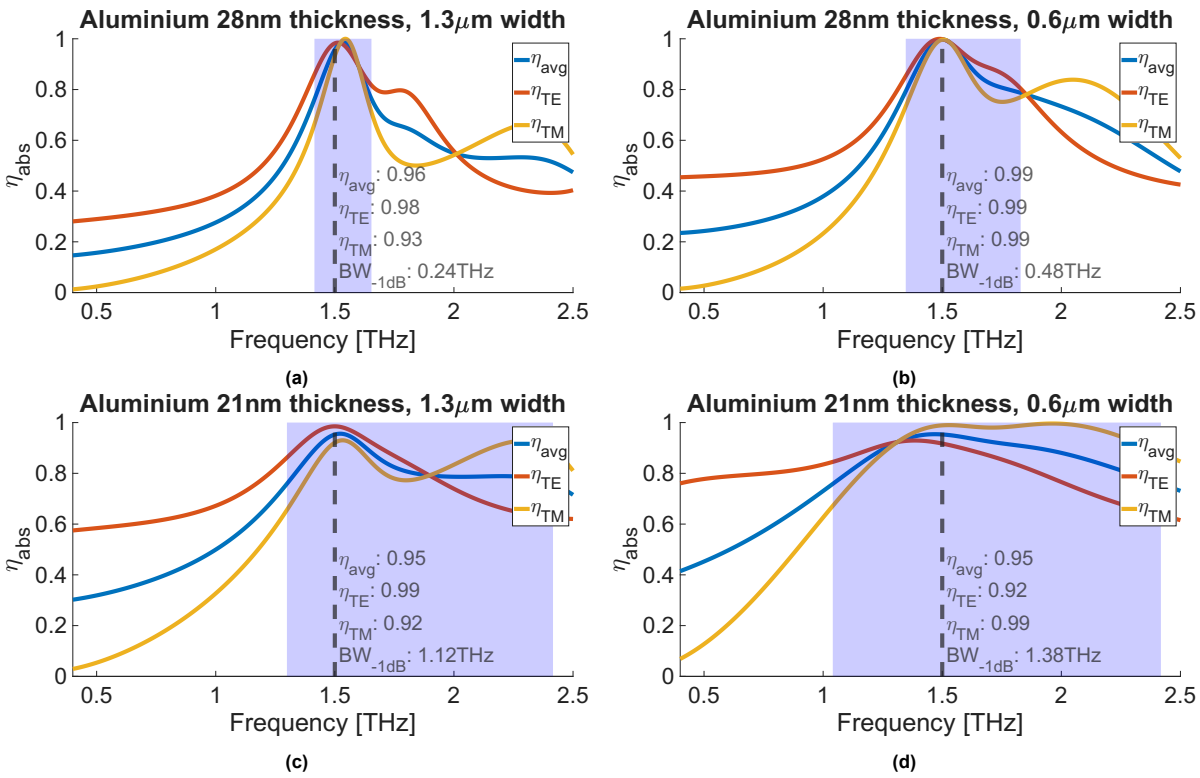

Fig. 2.15: The absorption efficiencies versus frequency for the 4 different absorber designs presented in this thesis, for which the design parameters of the complete absorber structure can be found in App. F. The efficiencies at the design frequency of 1.5 THz have been highlighted using a vertical line, and the $-1\mathrm{dB}$ bandwidth has been highlighted in blue.

Although the efficiency of the device drops slightly for the designs made using the thinner Aluminium, see Fig. 2.15c and Fig. 2.15d, since these devices offer a far larger bandwidth than devices made from the thicker aluminium, these two devices (whose unit cell design are shown in Fig. 2.16) are of most interest to this thesis, and thus have been selected as the most promising candidates for the final design. The final design selection was made after investigating the effect of each of these designs on MKID performance, as will be discussed in Sec. 2.4.4.

The design procedure discussed in this thesis has been proven to aid in the design of the meandering line absorbers discussed here, and could also be applied to high frequency designs, examples of which can be seen in App. G where absorbers are presented to operate up to 35 THz.

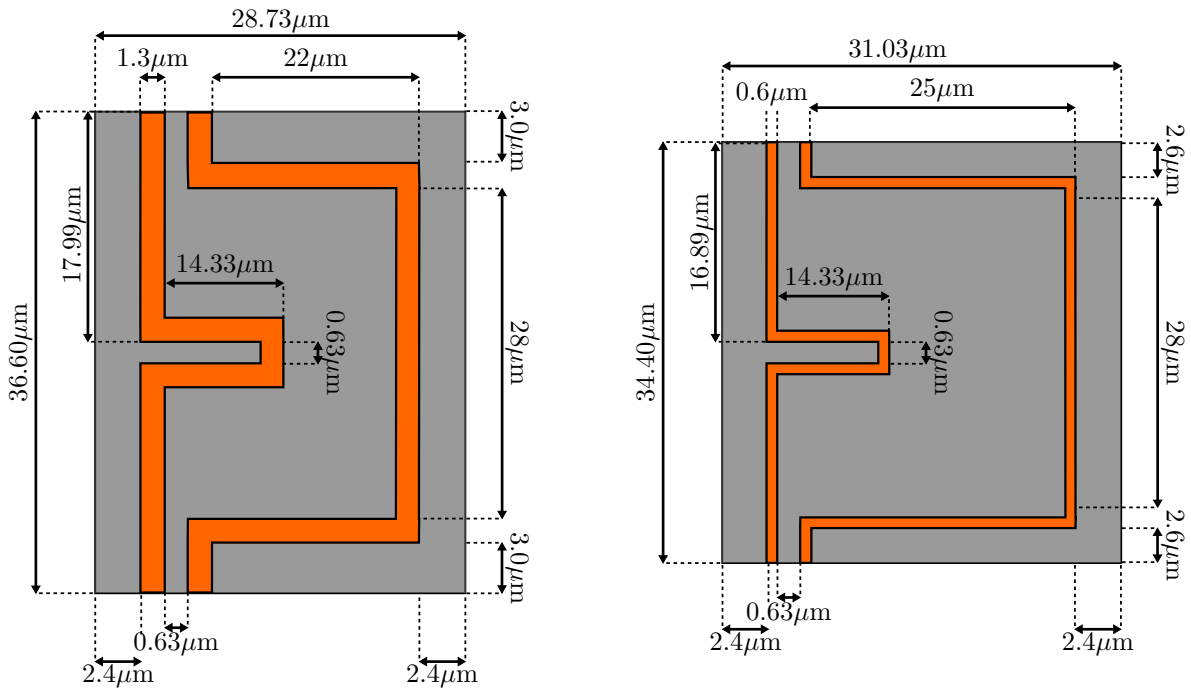

(a) Unit-cell design for a line width of $1.3\mu\mathrm{m}$

(b) Unit-cell design for a line width of $0.6\mu\mathrm{m}$

Fig. 2.16: Unit-cell designs made for Aluminium with a thickness of $21\mathrm{nm}$

2.4.3. Lens-Absorber Designs

Validation of the models

Before any of the lens-absorber designs and their analysis can be presented, the models introduced in Sec. 2.2 of this chapter must be verified. Hence, this first subsection will focus on the validation of the models presented in this chapter, such that they can be applied for the remainder of this chapter.

For the validation of the models, the design with 21 nm thick Aluminium and 0.6 $\mu\mathrm{m}$ wide lines presented in Sec. 2.4.2 will be used as a verification case. For each of the models presented in this chapter, the absorber, and where needed an associated lens, is modelled and compared to the same situation when simulated in CST.

The Floquet Wave model is used to calculate the response of a periodic absorbing structure to an incident plane wave. To construct this model for the aforementioned absorber, the impedance matrix of the absorber was obtained by simulating the response of the absorber in CST to plane waves of various angles of incidence. This impedance matrix was connected to the transmission lines shown in Fig. 2.1a that represent the stratification of the absorber. To validate the model, the absorber was illuminated by plane waves under various incident angles, and propagated into the transmission line model by calculating the equivalent voltage and current potentials as discussed in App. B. The power absorbed was determined by calculating the voltages and currents in the impedance matrix, and was compared to the same set of simulations in CST, leading to the result shown in Fig. 2.17. The difference between the CST simulation and the output produced by the in-house Floquet Wave model is negligible, and thus verifies the capabilities of the proposed technique.

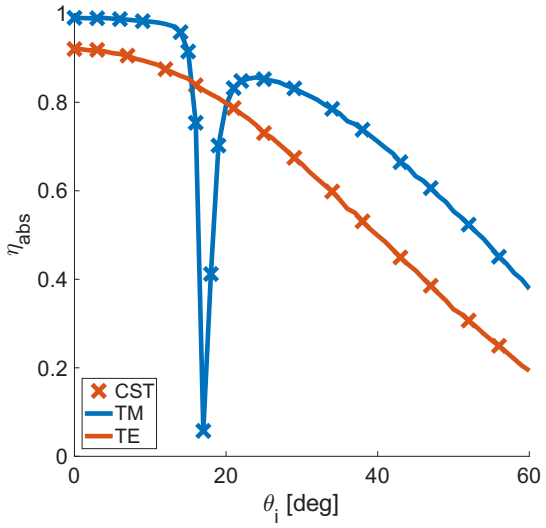

Fig. 2.17: Absorption efficiency versus angle of incidence for $\phi_i = 0°$ of the absorber design made with $21\mathrm{nm}$ thick Aluminium and a line width of $0.6\mu\mathrm{m}$. The absorption efficiency was calculated using the Floquet Wave model (shown as solid lines), and verified by calculating the absorption efficiency in CST (shown as the crosses).

The GOFO model approximates the focal field of a lens by propagating an incident field through the surface of the lens, to an auxiliary surface called the FO-sphere, and applying approximations on the radiation integral to represent the focal field as a Plane Wave Spectrum (PWS). In order to validate whether this PWS is generated accurately, the PWS was chained to the previously validated Floquet Wave model, such that it could be compared to the same lens-absorber simulated in CST.

For this validation case, the design with 21 nm thick Aluminium and 0.6 $\mu\mathrm{m}$ wide lines was coupled to a Silicon lens with an f-number of 2, a diameter of 1.4 mm, and an ideal $\lambda/4$ matching layer. This lens-absorber setup, which is shown in Fig. 2.18, is in line with to the lens-absorbers that have been designed in this thesis, and will be discussed in the remainder of this section.

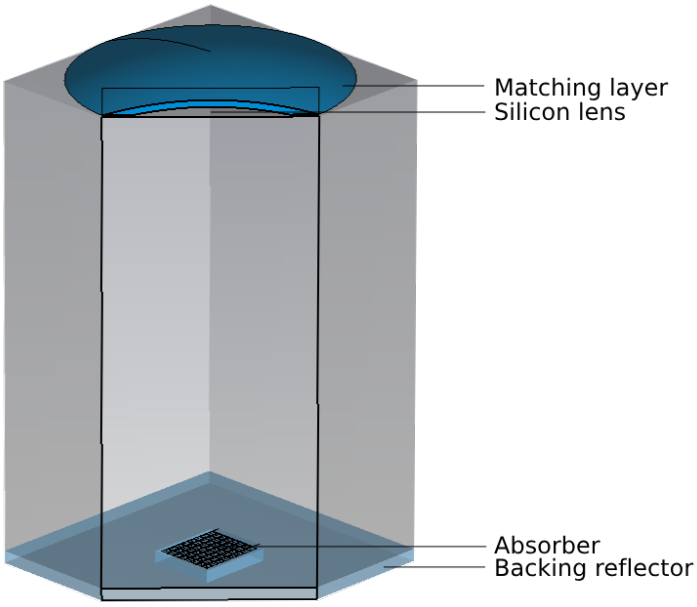

Fig. 2.18: A lens-absorber setup in CST, consisting of a silicon elliptical lens with a diameter of $D_{lens} = 1.4\mathrm{mm}$, an f-number of $f_{\#} = 2$, an ideal quarter wavelength matching layer, and coupled to an absorber with a side-length of $w = 2\lambda_d f_{\#}$. The absorber is made of $21nm$ thick Aluminium with a line width of $0.6\mu\mathrm{m}$. The lens absorber is terminated with a quarter wavelength backing reflector.

As mentioned in Sec. 2.2, although the analytical GO technique could offer an even faster model with certain approximations, the validity region for these approximations do not fully cover the lens design scenarios in this thesis. Therefore, for the remainder of this section, only the numerical GO technique has been used and validated.

The first step in the validation of the GOFO model, was to verify whether the GOFO model focuses the incoming field correctly. When plotting the calculated rays derived using the raytracing technique as shown in Fig. 2.19, two things are expected to happen: for the broadside case, all rays should focus perfectly on top of the absorber, since elliptical lenses focus all rays to the same focal point. Secondly, for off-broadside cases, the focus should shift along the domain of the absorber. For larger scanning angles, certain rays may start to defocus slightly. However, due to the f-number selected for this design, the lens is rather shallow, leading to a negligible defocusing of the rays. Both these expectations were met in Fig. 2.19.

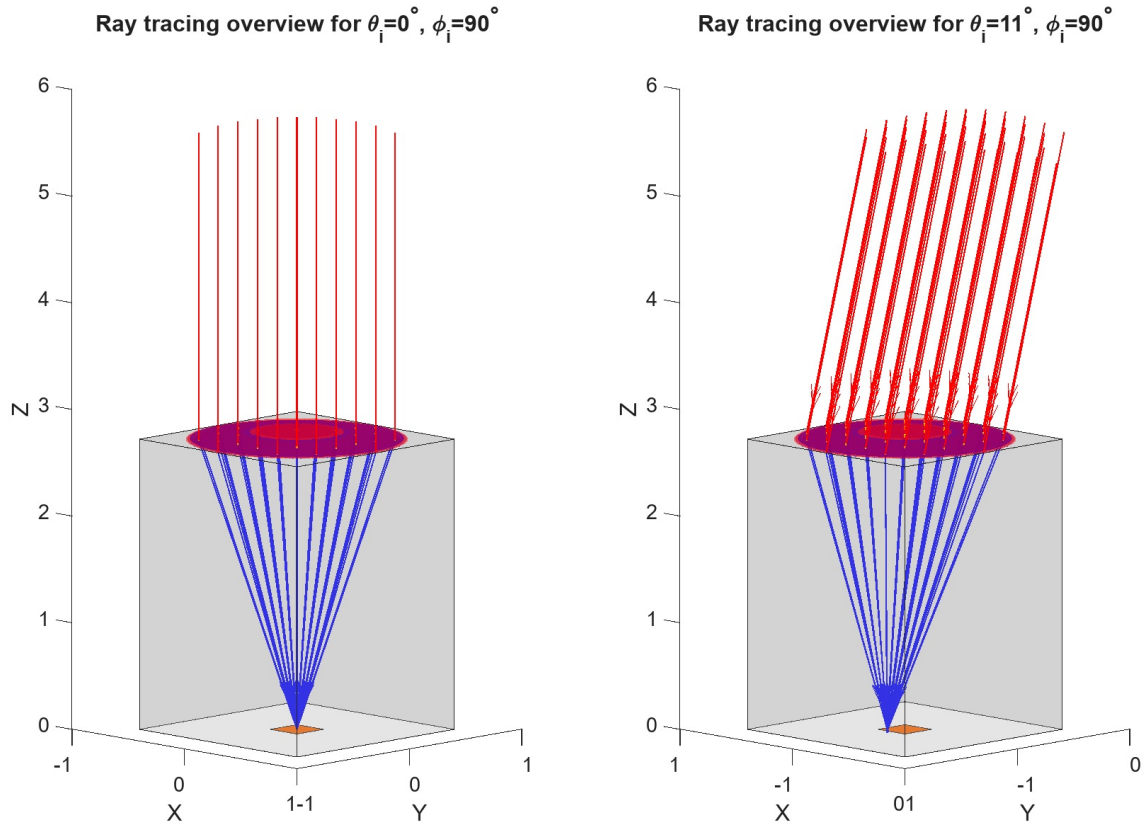

(a) The result of the raytracing algorithm for incident angles equal to $\theta_i = 0^\circ$ and $\phi_i = 90^\circ$

(b) The result of the raytracing algorithm for incident angles equal to $\theta_i = 11^\circ$ and $\phi_i = 90^\circ$

Fig. 2.19: Results of the raytracing algorithm for a lens with a diameter of $D_{lens} = 1.4\text{mm}$ and an f-number of $f_\# = 2$. An arbitrary absorber with side length $w = 2\lambda_d f_\#$ is placed in the focal plane of the lens. The incident rays are highlighted in red, while the rays of the scattered field inside the lens are highlighted in blue. The reflected rays have been omitted for clarity.

In order to validate whether the Plane Wave Spectrum (PWS) representation of the focal field is calculated accurately by the GOFO model, the pattern in reception of the lens-absorber under test was evaluated, and compared to the same situation in CST. Using the GOFO model, the full angular response can be evaluated rather quickly, as calculating the absorbed power for a single angle of incidence only takes a few seconds. Since the exact same simulation in CST can take 1-2 days for a single angle of incidence, depending on the angle of incidence, only three different angles of incidence were simulated and compared to the full angular response evaluated using the GOFO technique. When comparing the results generated by both techniques shown in Fig. 2.20, the difference between the results produced

are negligible. Validating that the GOFO technique, in combination with the Floquet Wave model, leads to an accurate model for the design phase and evaluation of the performance of existing lens-absorber designs.

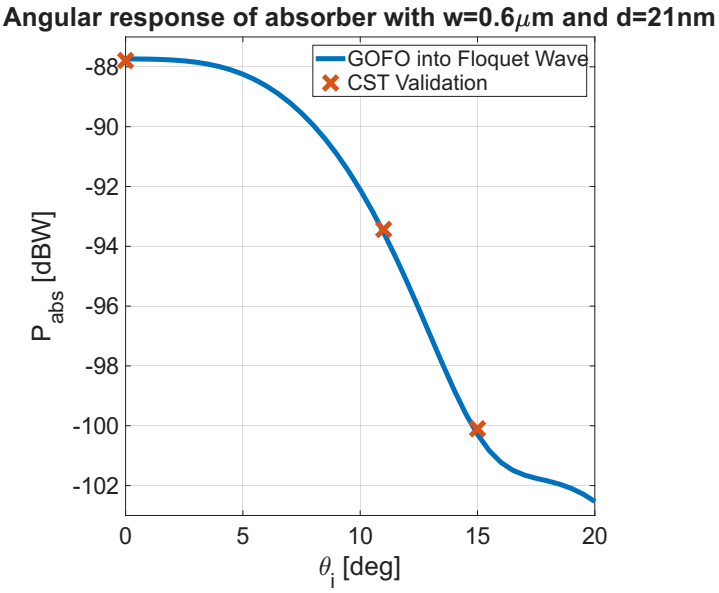

Fig. 2.20: The unnormalised angular response of a lens-absorber, with a lens with a diameter $D_{lens} = 1.4\text{mm}$ and an f-number $f_{\#} = 2$, coupled to one of the absorber designs from this chapter, made using 21nm thick Aluminium with a line width of $w = 0.6\mu\text{m}$. The angular response has been simulated using the models presented in this chapter (indicated with the blue line), and verified for 3 cases using CST (indicated by the orange crosses).

Analysis of the Lens-Absorber designs

As discussed before in Sec. 2.3.2, the silicon elliptical lenses are defined by 2 main parameters: the diameter (D_{lens}) and the f-number ($f_{\#}$) of the lens. In the aforementioned section, these two parameters were already fixed; the diameter was fixed by the measurement equipment used (1.4mm-1.5mm), and the f-number was fixed by the flat region in the angular response of the absorbers (an f-number of around 2). Therefore, for the remainder of this chapter, the lenses used will have a diameter of 1.4mm, and an f-number of 2.

The only parameter that still requires tuning, is the side length of the absorber. As described in Sec. 2.3.2, the side length of the absorber impacts the two main efficiencies discussed in this thesis: the focusing efficiency, and the aperture efficiency. As the latter is of interest for this thesis, the main objective is the optimisation of this performance criterion. As shown in Sec. 2.3.2, the aperture efficiency of a lens-absorber increases as the side length of the absorber increases. After evaluating the aperture efficiency of the aforementioned lens-absorber and varying the side length of the absorber, the result shown in Fig. 2.21 was obtained. The result confirms that as the absorber size increases, the aperture efficiency increases. Another key observation, is that the aperture efficiency curve flattens after an absorber side length of $w \approx 2\lambda_d f_{\#}$ has been reached. Although focusing efficiency is not of priority, in order to still retain some focusing without losing much aperture efficiency, the absorber side lengths have been chosen about $w = 2\lambda_d f_{\#}$, considering the periodicity of the unit cells.

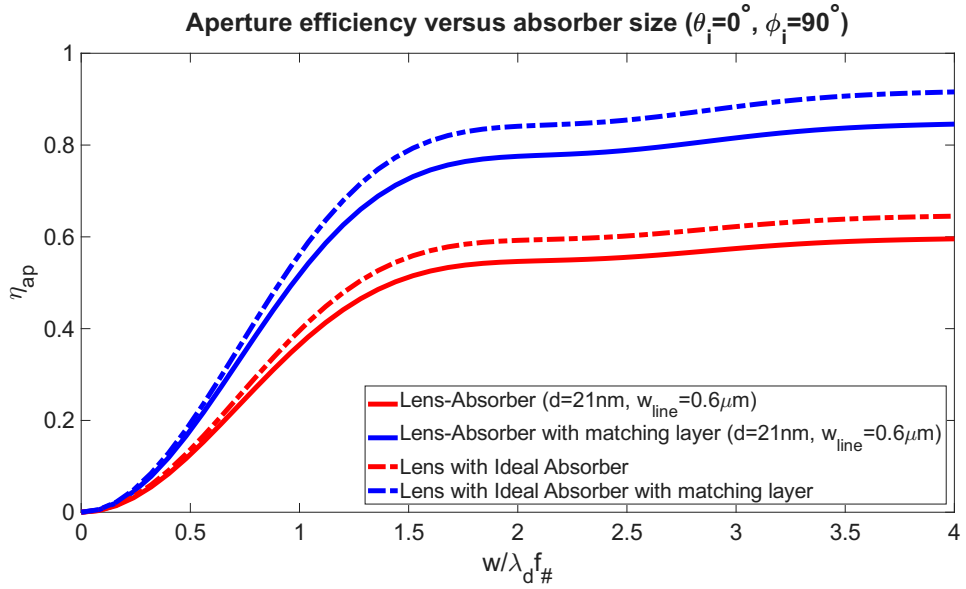

Fig. 2.21: Aperture efficiency of a lens-absorber as a function of side length of the absorber, with a lens with a diameter of $D_{lens} = 1.4\text{mm}$ and an f-number of $f_\# = 2$, coupled to an ideal absorber (shown with solid lines) and to the absorber design made with 21nm thick Aluminium and a line width of $0.6\mu\text{m}$ (shown with dashed lines). The figure compares the two absorbers, and shows the effect of a matching layer (red without matching layer, blue with matching layer) on the aperture efficiency of the lens-absorber.

Using Fig. 2.21, the effect of the matching layer on the performance of the lens-absorber can be studied as well. When comparing the aperture efficiency for a side length of $w = 2\lambda_d f_\#$, the efficiency increases from $\eta_{ap,\text{no matching}} = 0.546$ to $\eta_{ap,\text{matching}} = 0.775$, which is an improvement by a factor of ≈ 1.4. This additional performance is especially important when realizing that the lens-absorber will be coupled to other (quasi-)optical devices, each of which have additional losses due to their coupling.

Although the matching layer improves the overall performance of the lens-absorber at 1.5 THz, the $\lambda/4$ dependency of the matching layer does impose a limiting factor on the eventual bandwidth of the device. To increase the bandwidth, a matching layer with a larger bandwidth was added to the lens as proposed in Sec. 2.3.2. The effect of the matching layer can be approximated by assuming that the matching layer is exactly $\lambda/4$ for each frequency of interest, thus removing the frequency dependency of the matching layer. The effect of this wideband frusta layer is made clear when comparing Fig. 2.22a to Fig. 2.22b. Although the bandwidth is still limited by other factors, such as the $\lambda/4$ backing reflector, the bandwidth has clearly improved, especially at larger frequencies. For the remainder of this chapter, the lens-absorbers can be assumed to use the wideband frusta layer.

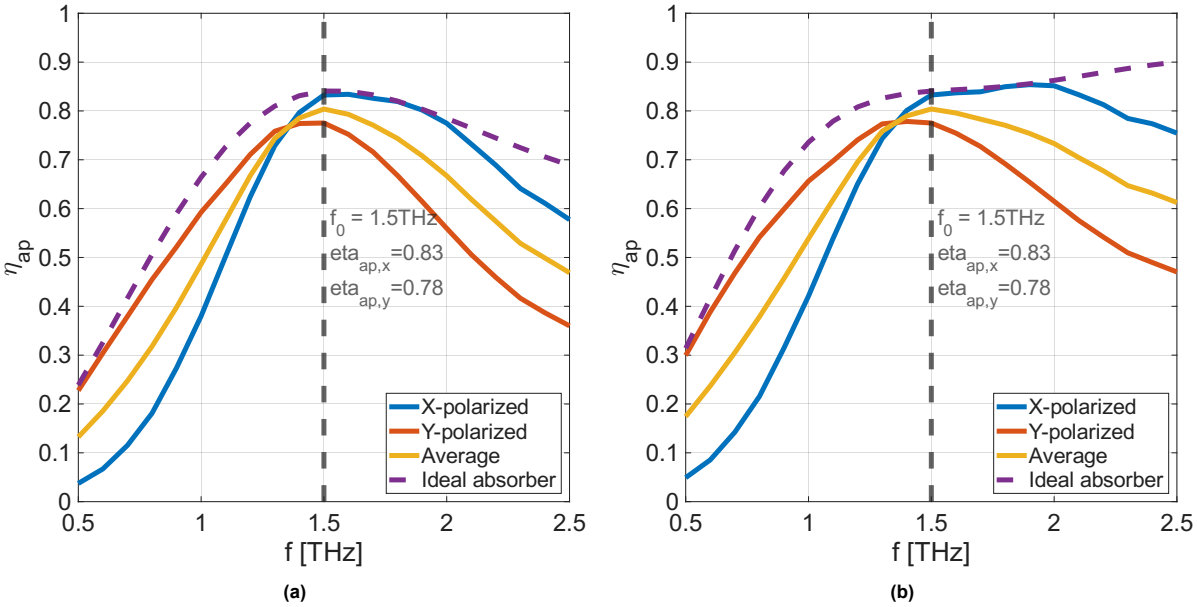

Fig. 2.22: Aperture efficiency of a lens-absorber as a function of frequency for plane waves from broadside direction with x- and y-polarisation, with a lens with a diameter of $D_{lens} = 1.4mm$ and an f-number of $f_{\#} = 2$ coupled to the absorber design with 21nm thick Aluminium and a line width of $0.6\mu\text{m}$, with a side length of $w = 2\lambda_d f_{\#}$. To compare the effect of the type of matching layer on the bandwidth of the detector, the lens-absorber is shown with (a) a quarter wavelength matching layer designed at 1.5 THz, and (b) an ideal matching layer that is a quarter of a wavelength thick for every frequency. To indicate the maximum possible aperture efficiency with the provided lens and matching layer, the absorber was replaced with an ideal absorber of the same size, and shown in purple.

Another observation that can be made from Fig. 2.22b, is the frequency dependency of the aperture efficiency of an ideal absorber, which describes the theoretical limit for these design parameters. Especially for the lower end of the frequency range, the maximum possible efficiency drops drastically. Since the aperture efficiency has been calculated for a lens-absorber designed at 1.5 THz, all design parameters remain fixed including the size of the absorber. As visible in Fig. 2.21, the selected side length of $w = 2\lambda_d f_{\#}$ is right on the edge of the flattening region of the aperture efficiency versus side length curve. For lower frequencies, the wavelength increases, thus an absorber designed for 1.5 THz becomes smaller in terms of wavelength. The aperture efficiency drops rapidly for absorbers smaller than $w = 2\lambda_d f_{\#}$, therefore the bandwidth at the lower end of the frequency range is limited by the size of the absorber.

With all bandwidth limiting factors in mind, it is important to set requirements on the bandwidth needed at the start of the absorber design process. Especially as lower frequencies in the bandwidth of the lens-absorber are limited by the size of the absorber, it might be beneficial to optimise a unit-cell design for a lower frequency instead, or increase the absorber size slightly to compensate for the losses at lower frequencies.

2.4.4. Absorber-MKID Designs

Using the 4 unit cell designs discussed in Sec. 2.4.2, for which the design parameters of the complete absorber structure can be found in App. F, similar absorber structures as shown in Sec. 2.3.3 were constructed. For each of these structures, the following requirements were met:

- Each design must use an integer amount of unit cells along the width and height of the absorber
- Each design shall have a width and height of at least $w = 2\lambda_d f_{\#}$, as discussed in Sec. 2.4.3
- The number of unit cells along the width and height of the absorbers shall be odd, to ensure a unit cell at the center of the absorber which is located at the focal point of the lens

Based on these requirements, 4 structures were constructed and simulated in Sonnet to obtain the microwave input impedance of the absorber structure, to be able to calculate the MKID resonant frequency as described in Sec. 2.3.3. Since these devices contain a large amount of Aluminium, the

imaginary part of the impedance of the structure will be much larger than for other detectors such as antennas. This will also have an effect on the resonance behaviour of the device, as the resonance will be pushed to lower frequencies.

To study the effect of the proposed absorbers on possible MKID designs, an MKID was designed for each absorber, with a resonance frequency located at $f_{MKID} = 3$ GHz, using Eq. 2.31 to tune the length of the NbTiN transmission line. The outcome of these designs is shown in Fig. 2.23.

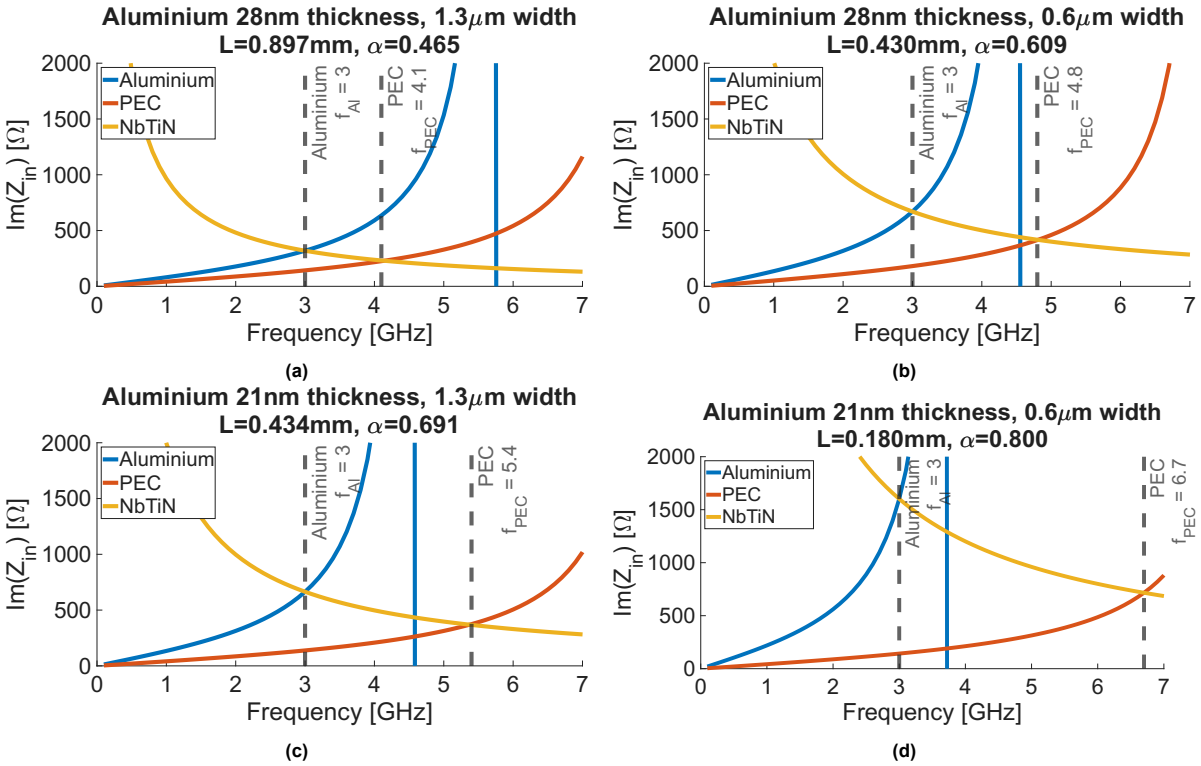

Fig. 2.23: Analysis of designs of MKIDs for each of the absorbers designed in this section, for which the design parameters of the complete absorber structure can be found in App. F, at a resonance frequency of 3 GHz. The length L of the transmission line section in these MKIDs are indicated in the titles of the figures. The yellow lines indicate the imaginary input impedance of the transmission line section of the MKID and the blue lines indicate the imaginary input impedance of the absorber structure. The red lines indicate the imaginary input impedance of the absorber structure after replacing all Aluminium with PEC. The resonance frequency f_{PEC} obtained in the MKID when using PEC instead of Aluminium is used to calculate the kinetic inductance fraction α, indicated in the titles of the figures.

A device that is predominantly inductive has an associated self-resonance frequency due to additional capacitances in the device. Once the capacitance of the absorber structure resonates with the inductance, the imaginary impedance increases drastically, making the device appear as an open-circuit. A predominantly inductive device can only be used as an inductor up to this self-resonance frequency. As shown in the figure above, the absorber structures have a relatively low self-resonance frequency located around 4-6 GHz. Due to this lower self-resonance, the maximum possible resonance frequencies of MKIDs that can be designed with these absorbers will also be relatively low, as some length of the NbTiN transmission line has to be reserved to implement the coupler of the MKID. A transmission line length of 500 μm is a reasonable lower limit, allowing resonant frequencies up to 2 GHz for the design with a thickness of 21 nm and a line width of 0.6 μm. This is close to the frequency ranges of the measurement equipment available at SRON that have an operating range of roughly 2-4 GHz.

Fig. 2.23 also indicates the effect of the thickness and line width of the unit-cell designs on the self-resonance of the device. For thinner materials with narrower lines, the self-resonance is located almost 2 GHz lower compared to thicker and wider lines. Taking into the account the aforementioned issue, this introduces a trade-off between absorber performance and range of possible MKID resonance frequencies. For a larger bandwidth, the self-resonance is shifted lower, thus leading to a limited number

of MKIDs that can be designed for the measurement equipment available.

Another advantage of selecting a design with thinner and narrower meandering lines, is the higher kinetic inductance fraction α, which is almost twice as high for $f_{MKID} = 3$ GHz compared to the design with thicker and wider meandering lines. The kinetic inductance fraction, which is defined as

$$\alpha = \frac{L_k}{L_k + L_g} \tag{2.33}$$

where L_k is the kinetic inductance and L_g is the geometric inductance, has an impact on the sensitivity of the device: a higher kinetic inductance fraction results in a higher sensitivity [27]. For the designs shown in Fig. 2.23, which are based on transmission line resonators, the kinetic inductance fraction has been calculated using

$$\alpha = 1 - \delta F^2 \tag{2.34}$$

which has been derived in App. E, where δF is defined as the ratio between the resonant frequency of the actual MKID (defined for clarity as f_{Al} in Fig. 2.23), and the resonance frequency of the exact same device after replacing all Aluminium with PEC material (defined as f_{PEC} in Fig. 2.23):

$$\delta F = \frac{f_{Al}}{f_{PEC}} \tag{2.35}$$

Taking into account all aforementioned trade-offs, the decision was made to select two final lens-absorber designs: both unit-cell designs with Aluminium with a thickness of $21\mathrm{nm}$. Since the design with narrower meandering lines has the widest bandwidth, this design is most promising for future missions. This design with 0.8 $\mu\mathrm{m}$ will yield a more sensitive device, which will also saturate at lower radiation powers. Hence, this design is less suitable for experiments measuring the radiation pattern, since these require radiation from the laboratory environment to couple to the detector, which will always be a significant amount of radiation power. Additionally, as this design has a self-resonance close to the lower limits of the measurement equipment at SRON, this design has been employed only in lens-absorber arrays with few pixels. To test the capabilities of the lens-absorbers to be integrated into larger arrays, the unit-cell design with 1.3 $\mu\mathrm{m}$ wide lines has been chosen. It is important to note that for the POEMM mission, the longest wavelength is at 113 $\mu\mathrm{m}$ [5], almost twice shorter than the presented 200 $\mu\mathrm{m}$ design. Even a narrow line design will be possible for large arrays due to the significantly smaller absorber size.

3

Fabrication of 1.5 THz Detectors

In this chapter the implementation of the lens-absorber coupled MKIDs designed in Ch. 2 is discussed. The design and fabrication will be presented for 3 different configurations:

1. Detectors with lenses with a conventional quarter wavelength anti-reflective coating
2. Detectors with a wideband, mechanically machined coating
3. Detectors with a backshort, to increase the coupling efficiency

A total of 3 different experiments will have to be performed, that are applicable to all 3 design configurations:

1. Measure the radiation coupling efficiency and NEP using a low power, low temperature calibration source. This experiment can be performed using both designs presented in Ch. 2 with 0.6 μm and 1.3 μm line widths
2. Measure the multi-moded beam pattern, which can be performed using the design with a 1.3 μm line width presented in Ch. 2
3. Design a large array to measure the scalability of the designs

Due to fabrication constraints no experiments will be discussed in the context of this thesis, but the chapter will focus on the principle of the detector assembly, fabrication of anti-reflective coating, and the tooling designed to automatically generate MKID arrays of arbitrary size.

3.1. Lens and Substrate Design

In Ch. 2, 4 different absorber designs have been presented, of which 2 have been selected as potential candidates for fabrication, each with Aluminium thickness of 21 nm. Both of these designs have been selected to be fabricated in order to perform the experiments discussed.

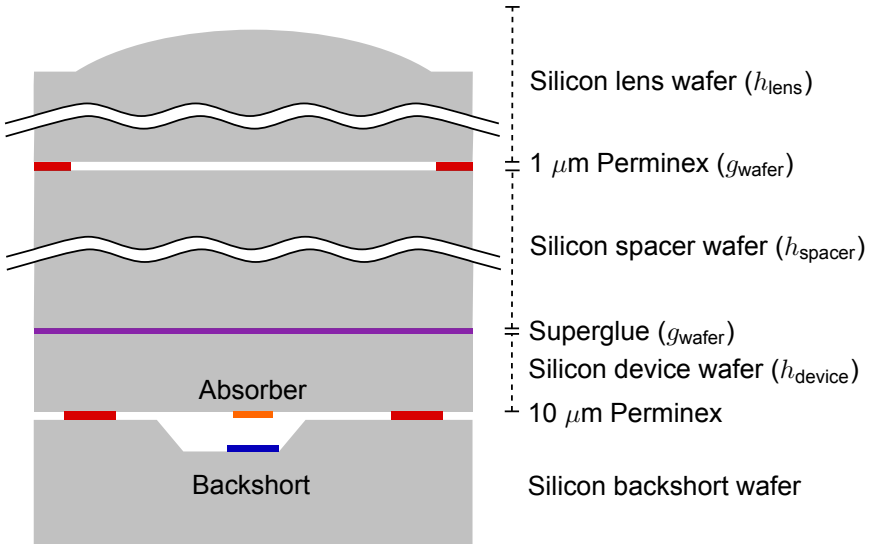

Fig. 3.1: Diagram of the stratification of the detectors, consisting of a wafer for the elliptical lens, spacer between the detector and lens, the absorber, and finally the backshort layer.

The stratification of the lens-absorbers is shown in Fig. 3.1, which consists of multiple Silicon wafers of various thicknesses. Due to the stratification, the lens and the absorbers can be fabricated separately, which allows for a simplified fabrication process and the reuse of the fabricated lenses. The complete stratification consists of a lens wafer, a device wafer containing the absorber, the backshort wafer, and an additional spacer wafer to reach the height needed for a lens with a diameter close to $D_{lens} = 1.4\mathrm{mm}$ and an f-number of $f_{\#} = 2$. The spacer wafer and the lens wafer are connected using a Perminex layer, and the device wafer is connected to the backshort wafer in a similar fashion. The device wafer is connected to the lenses using superglue, which can be dissolved with acetone, such that the lenses can be detached. This way the lenses can be reused for different absorber designs. In addition, since the effect of the matching layer will be studied, lenses with and without a matching layer should be swapped out easily.

Between the device layer and spacer wafer, an additional β-Ta mesh has been added, similar to the design in [2]. This mesh absorbs any THz radiation that is not coupled to the absorber but instead scattered into the chip, ensuring no other pixels will detect the scattered radiation [4].

3.1.1. Lens Designs

Due to the dimensions of the different wafers, and in particular the tolerances of each of the wafer thicknesses, the lenses designed in Ch. 2 cannot be exactly reproduced. Additionally, since the fabrication method that is used to make the lenses removes material from the top of the wafer, an additional margin should be taken into account at the top of the lens wafer as a safeguard in case too much material is removed. These various parameters and margins, including the gaps between different wafers due to the Perminex and superglue, are provided in Tab. 3.1

Parameter	Value (μm)
h_{lens}	1064
h_{spacer}	1523
h_{device}	350 ± 25
g_{wafer}	1
m_{lens}	20

Tab. 3.1: Considered parameters for the full lens stratification. The parameters h_{lens}, h_{spacer}, and h_{device} are the heights of the lens, spacer, and device substrate, respectively. The g_{wafer} parameters is the gap-size between the different wafers, and m_{lens} is the margin taken into account for the thickness of the lens wafer.

For the final lens design, the worst-case parameter values are chosen, therefore all margins and tolerances are subtracted from the parameter values. As stated in Sec. 2.3.2, lenses had to be chosen with a diameter D_{lens} in the range of 1.4mm to 1.5mm, and an f-number that approaches $f_{\#} = 2$. Using the restrictions in place by the dimensions, margins, and tolerances, a design was selected with $D_{lens} = 1.4\text{mm}$ and $f_{\#} = 2.041$.

A second lens design was made where the matching layer discussed in Sec. 2.3.2 had to be added to the design. For the frusta matching layer, a scaled-down version of the design presented in [24] was used, which dimensions are shown in Fig. 3.2a. This frusta layer is realized by taking an elliptical lens design without a matching layer, and shifting the ellipsoid upwards by h_{frusta}. This way, the elliptical shape of the lens can be manufactured first, afterwards the grooves are cut into the silicon leading to the final elliptical lens with frusta layer. Due to this frusta layer, an additional h_{frusta} must be subtracted from the total height of the stratification, and a new design must be made accordingly. The same diameter was selected as for the lens without the matching layer, leading to a final design with $D_{lens} = 1.4\text{mm}$ and $f_{\#} = 2.007$.

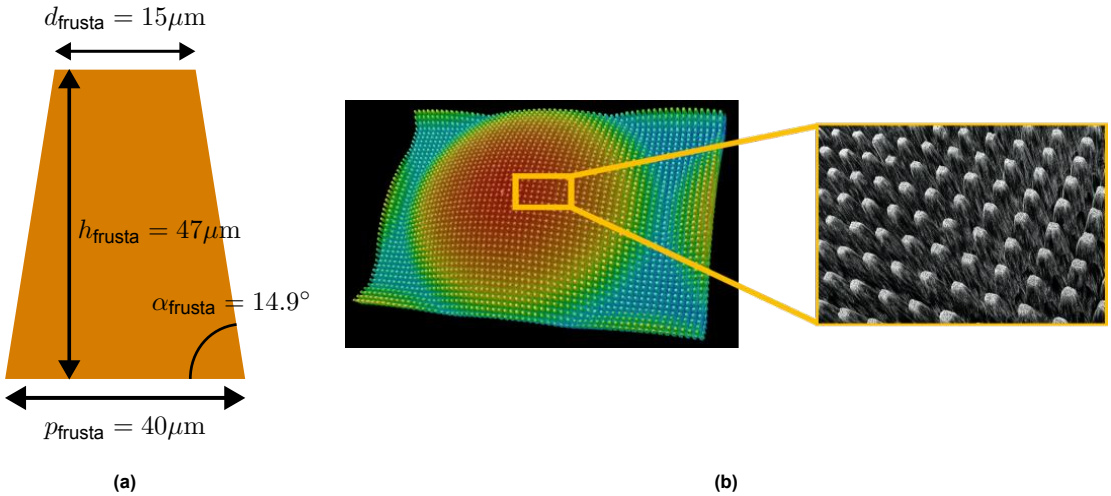

Fig. 3.2: A frusta matching layer, that provides anti-reflective properties at a large bandwidth. Figure shows a (a) diagram of a single unit cell of the frusta matching layer and its dimensions, and (b) a 3D picture of a frusta lens taken from [25].

3.1.2. Backshort Design

As discussed in Ch. 2, a large portion of the radiation transmits through the absorber limiting the absorption efficiency. By adding a backshort to the design, the absorption efficiency can be improved. To add this backshort to the lens-absorber, an additional wafer is glued to the bottom of the detector wafer using Perminex. A groove has been cut in the backshort wafer underneath the absorber, which can be seen in Fig. 3.3. The groove has a depth equal to a quarter of the wavelength of free space, and has slanted walls. The groove itself is wider than the absorber, as can be seen in Fig. 3.3, and only a portion of this groove is covered with a $500\mu\mathrm{m}$ by $500\mu\mathrm{m}$ square Aluminium layer that serves as a reflector. The reason why only a portion is covered by Aluminium, is to ensure minimal coupling between the transmission line of the MKID and the Aluminium slab, as coupling to the reflector might change the resonance behaviour of the MKID.

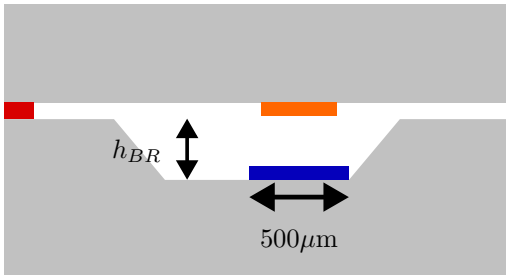

Fig. 3.3: Diagram of the backshort added to the design. The Aluminium reflector is $500\mu\mathrm{m}$ wide, and aligned to the center of the absorber while not being present above the MKID's CPW transmission line.

3.2. Automated Mask Generation

The detectors designed in this thesis will be employed in large arrays to provide both imaging as well as spectroscopic capabilities. Designing the chips that contain many of these detectors is a tedious process, especially once multiple different design iterations must be fabricated. Taking into account the fact that in the missions discussed in this thesis, multiple different designs will have to be employed for different frequencies, designing each of these chips manually is a tedious task and prone to errors. Therefore, a pipeline has been developed that can automatically generate mask designs using the mask definition format CIF [31] based on a simple definition of the absorber geometry.

3.2.1. Definition File

To simplify the storage and distribution of different absorber files, a parameter file was defined, written in the JSON format, to store the absorber geometry, and dimensions related to the complete absorber structure. The JSON format can be parsed by most programming languages and is human readable, simplifying the use and distribution of the design definitions. The format, which can be seen in App. H, consists of three major parts: the absorber unit cell dimensions as shown in Fig. 3.4a, the absorber structure dimensions as shown in Fig. 3.4b, and information on the materials used. The file also contains some additional information, such as whether the masks should be generated in an inverted matter, and an identifier for the design.

The simplicity and small size of the JSON definition files ensure maintainability, while providing the possibility to combine multiple different absorber designs in the future to generate masks for future FIR missions.

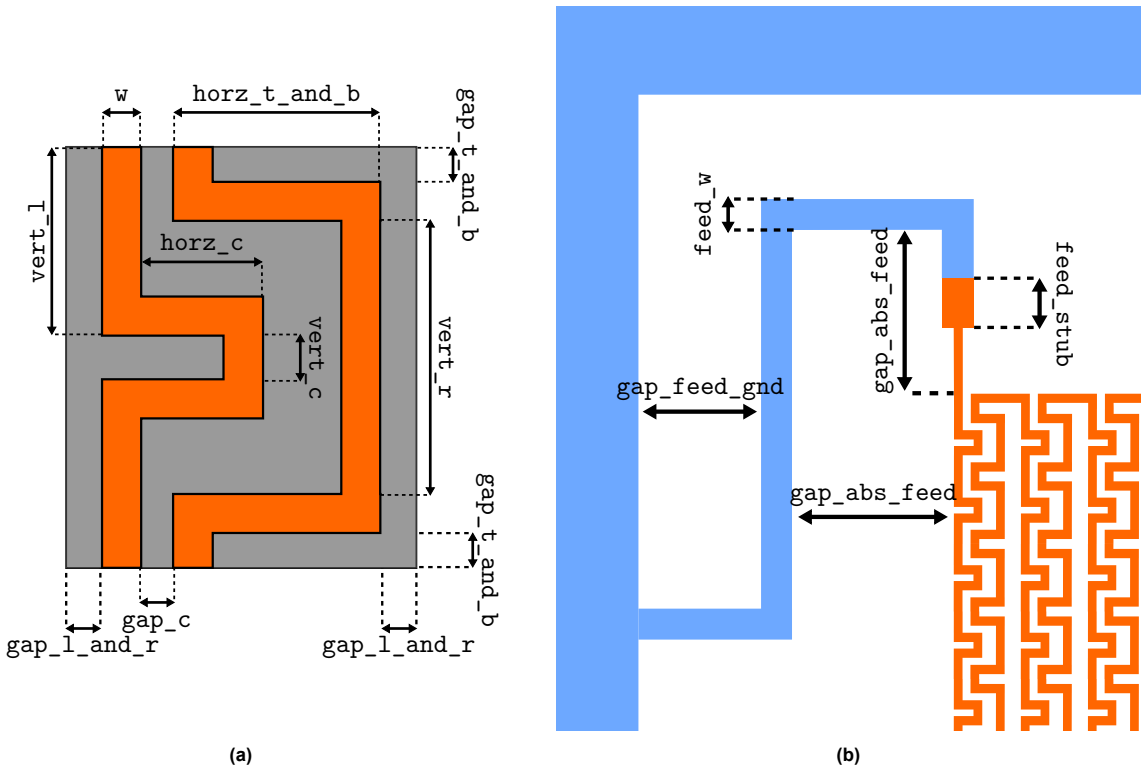

Fig. 3.4: Definitions of the dimensions contained in the JSON which are discussed in App. H for (a) a unit-cell of the absorber and (b) dimensions of the feeding lines of the absorber structure. In both figures the Aluminium is coloured orange, and the NbTiN is coloured blue.

3.2.2. Mask Generation Pipeline

When provided with a JSON definition file of the absorber, the Automatic Mask Generation tool uses a pipeline to automatically generate a mask for a predefined range of MKID resonance frequencies. The tool uses text inputs in its main script to define the KID shape, frequencies, Q-factors, and other related parameters, and an option to select a given geometry defined in a JSON definition file. A diagram of this pipeline is shown in Fig. 3.5.

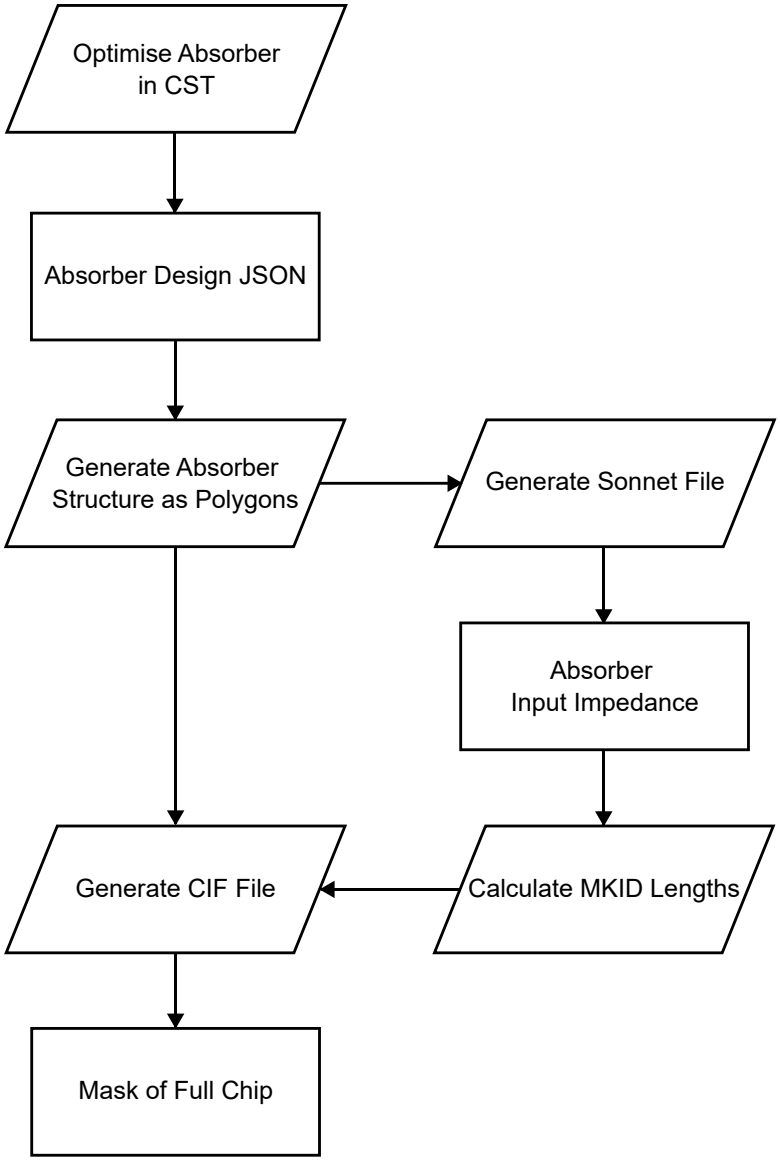

Fig. 3.5: Complete pipeline of automatic mask generation. By providing a JSON with design and material parameters a mask can be generated automatically.

Using the definition of the unit cells of the absorber, and the definition of the absorber structure, the tool generates a polygon structure of the complete absorber structure (which is similar to what was shown in Fig. 2.12). This polygon structure is used in two instances: to perform a microwave simulation in Sonnet of the absorber structure to determine the self-resonance of the absorber structure (as discussed in Sec. 2.3.3), and to create the CIF definition of the absorber structure. Using the output of the Sonnet simulation the lengths of each of the MKID transmission lines can be calculated and used to generate the CIF definition of the complete mask.

An example of a mask generated using the tool is shown in Fig. 3.6a, with a zoom-in on a single detector in Fig. 3.6b. This tool is employed to prepare multiple lens absorber masks for the future experiments at 1.5 THz. The tool is also easily adaptable for any other absorber design: the process in Fig. 3.5 needs to be repeated for a new set of wavelength and bandwidth requirements, resulting in a new geometry. These geometry parameters can be stored in a new JSON definition file, which can than be used by the developed tool to generate any MKID array needed.

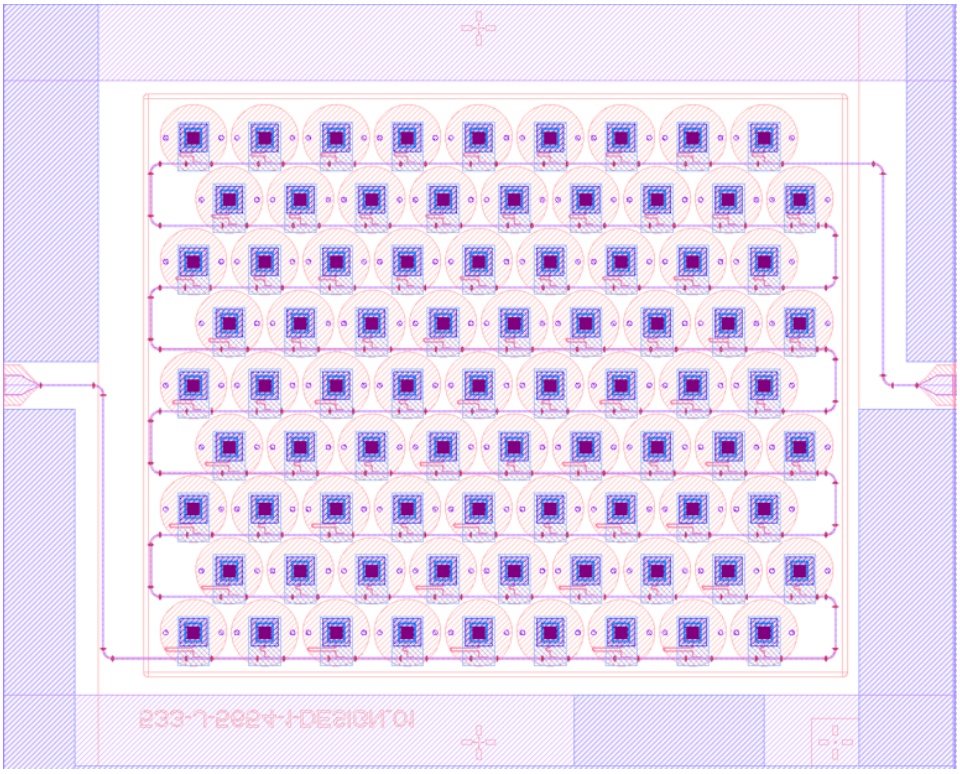

(a)

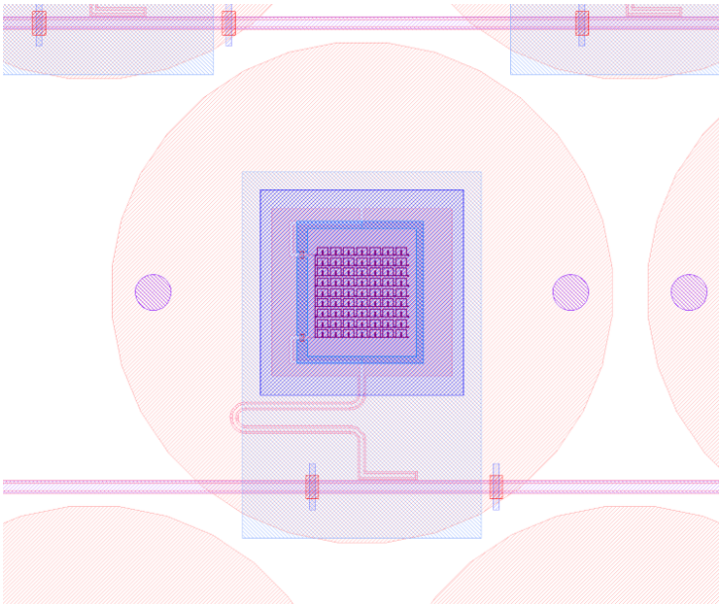

(b)

Fig. 3.6: Mask generated for a chip consisting of 81 lens-absorbers, see Sec. 3.3.3. using the design presented in Ch. 2 with $21\mathrm{nm}$ thick Aluminium and $1.3\mu\mathrm{m}$ wide lines. The full mask is shown in (a), and a zoom-in on a single detector is shown in (b).

3.3. Chip Designs

Using the tool presented in Sec. 3.2, a total of 3 chip designs were generated, according to the design configurations discussed in the introduction of this chapter. The design parameters for these chip designs will be briefly discussed here.

3.3.1. Chip 1: Radiation Coupling and NEP Measurements

This chip will be used to measure the performance of the lens-absorbers. The chip will be fabricated multiple times such that the performance of the absorber design can be measured once with a backshort and frusta matching layer, and once without a backshort and frusta matching layer to compare the effect of the backshort and matching layer on the performance of the detector.

- Absorber design: $21\ \mathrm{nm}$ thick Aluminium with a line width of $0.6\ \mu\mathrm{m}$, as defined in Sec. F.1
- Array design: 5 by 3 KIDs (15 KIDs total), hexagonally spaced with a $1.5\ \mathrm{mm}$ pitch
- KID Q-factor: 120000
- KID resonance frequencies: 2 GHz - 2.2 GHz
- KID frequency spacing $\mathrm{d}f$: $\mathrm{d}f/f = 1 \times 10^{-2}$ ($\mathrm{d}f$ scales with KID frequency)

3.3.2. Chip 2: Multi-Moded Pattern Measurements

This chip will be used to perform measurements on the pattern in reception of the lens-absorbers.

- Absorber design: $21\ \mathrm{nm}$ thick Aluminium with a line width of $1.3\ \mu\mathrm{m}$, as defined in Sec. F.2
- Array design: 5 by 3 KIDs (15 KIDs total), hexagonally spaced with a $1.5\ \mathrm{mm}$ pitch
- KID Q-factor: 40000
- KID resonance frequencies: 2.02 GHz - 2.90 GHz
- KID frequency spacing $\mathrm{d}f$: $\mathrm{d}f/f = 2.5 \times 10^{-2}$ ($\mathrm{d}f$ scales with KID frequency)

3.3.3. Chip 3: Large Array for Scalability

This chip will be used to test the scalability of the absorber designs, and to measure the overall yield of the absorber coupled MKIDs.

- Absorber design: $21\ \mathrm{nm}$ thick Aluminium with a line width of $1.3\ \mu\mathrm{m}$, as defined in Sec. F.2
- Array design: 9 by 9 KIDs (81 KIDs total), hexagonally spaced with a $1.5\ \mathrm{mm}$ pitch
- KID Q-factor: 200000
- KID resonance frequencies: 2.1 GHz - 3.2 GHz
- KID frequency spacing $\mathrm{d}f$: $\mathrm{d}f/f = 5 \times 10^{-3}$ ($\mathrm{d}f$ scales with KID frequency)

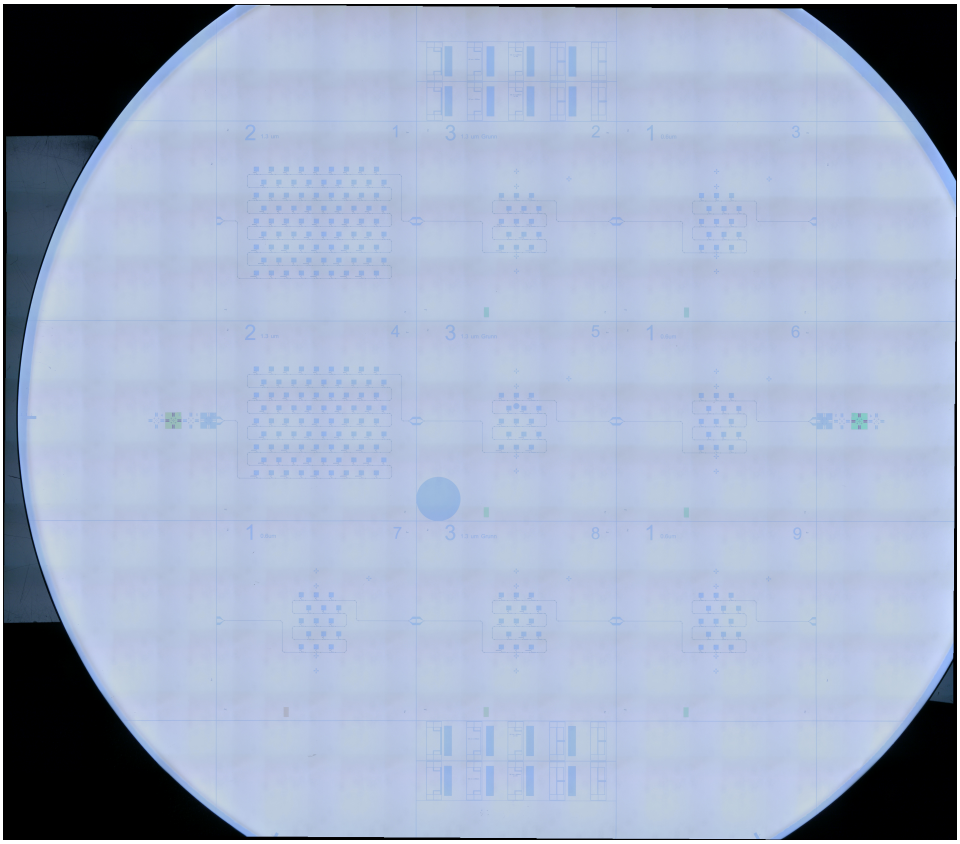

(a)

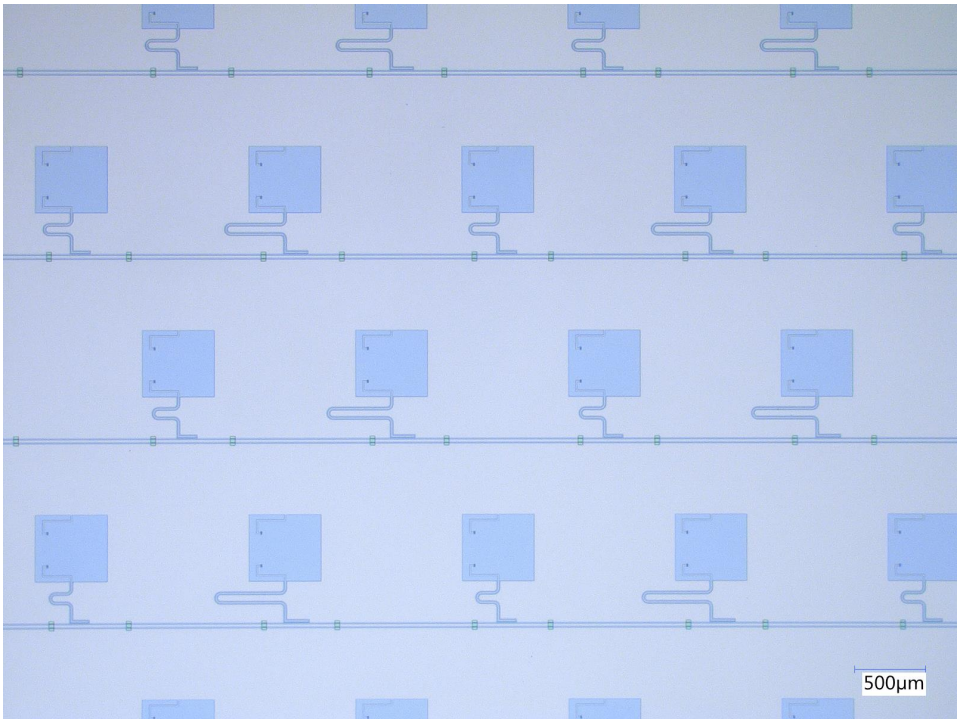

(b)

Fig. 3.7: SEM pictures of the current state of the chip fabrication. The chips in the picture do currently not contain any Aluminium, as this is one of the last steps in the fabrication process. (a) shows the different chip designs, and (b) is a close-up picture of some of the detectors of Chip 3 discussed in Sec. 3.3.3.

4

Optimisation Techniques for Coupling to Optical Systems of Future FIR Missions

The missions discussed in this thesis have one specific requirement in common: requiring an FIR instrument capable of performing imaging spectrometry. To fulfill this goal, a 2D imaging array can be designed using the detectors discussed in this thesis, where the detectors along one axis will perform imaging in the spatial domain, while the detectors along the other axis perform imaging in the frequency domain, i.e. spectrometry.

To ensure that each detector will only receive a limited spectral band, a dispersive element is required capable of providing a high resolution in terms of frequency. Commonly, an element such as a diffraction grating is used as a dispersive element, however, the diffraction grating is typically capable of providing spectra with a limited resolution ($R = f/\,\mathrm{d}f \leq 1000$) [8] and [32]. Therefore, more advanced dispersive elements were investigated, one of which is proposed for the missions discussed in this thesis: the Virtually Imaged Phased Array (VIPA). The VIPA is a simple design of a dispersive element, consisting of two (partially) reflective plates, capable of providing a large angular-dispersion versus wavelength [8].

Although the VIPA offers the high resolution that is required in the aforementioned missions, the device is certainly not ideal. Issues with higher order modes, phase aberrations in the fields focused on the detector, and dependencies to non-uniform material parameters in the (partially) reflective plates can complicate the coupling of the detectors to the VIPA, and reduce the overall efficiency of the instrument. In this chapter, an initial analysis is performed on the VIPA coupling to detectors, and various optimisation techniques will be discussed to improve this coupling between the detectors designed in this thesis and the VIPA that is currently being developed for FIR missions.

4.1. The Virtually Imaged Phased Array

As briefly touched upon in the introduction of this chapter, the VIPA is a dispersive element resembling a Fabry-Perot etalon, consisting of two parallel plates placed under a certain angle [8], [32], and [33]. One of these plates is fully reflective, while the other plate is partially reflective. As visible in Fig. 4.1, when the VIPA is illuminated by a collimated beam, which is focused slightly behind the VIPA and propagates through a window in the fully reflective plate, the field will start to reflect between the two plates and propagate upwards. Each time the field reflects on the partially reflective plate, part of the incoming field will be able to propagate through the VIPA. Due to the multiple back-and-forth reflections, a series of divergent beams are transmitted from the partially reflective plate, which is illustrated in Fig. 4.1 by means of beams with different colours.

Due to the interference between these beams, an output is obtained which varies with wavelength, where each wavelength has a narrow peak of energy. This output, which has its interference pattern focused at infinity, is focused on a focal plane using an additional focusing element, leading to an interference pattern with a large angular-dispersion versus wavelength.

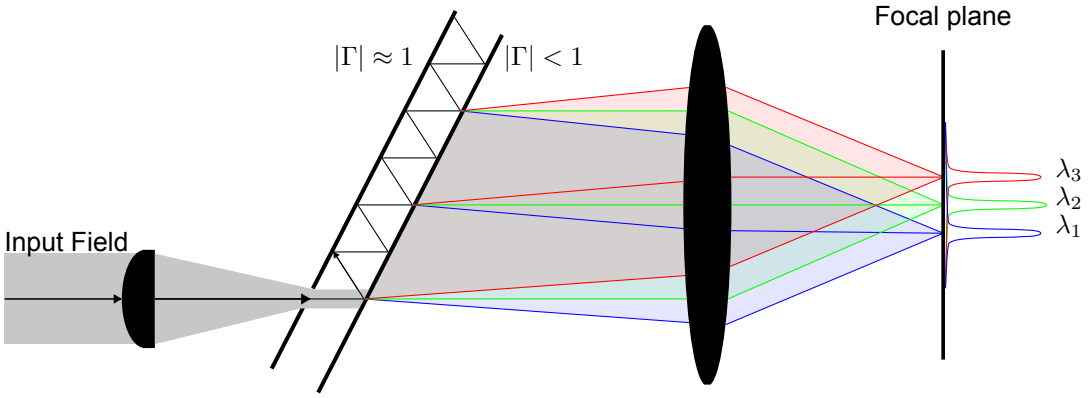

Fig. 4.1: A schematic representation of a VIPA. The output consists of divergent beams of different wavelengths, of which 3 have been shown in red, green, and blue. The interference pattern between these beams leads to an output with a large angular-dispersion versus wavelength, where each wavelength has a narrow distribution when focused on a focal plane.

Due to the narrow angular distributions of each wavelength, the output of the VIPA can be represented and modelled by multiple virtual images of the incoming field [8] and [32]. The interference of these virtual images at the output of the VIPA is an accurate description of its behaviour, which is shown in the schematic in Fig. 4.2, thus leading to the device's name: the Virtually Imaged Phased Array.

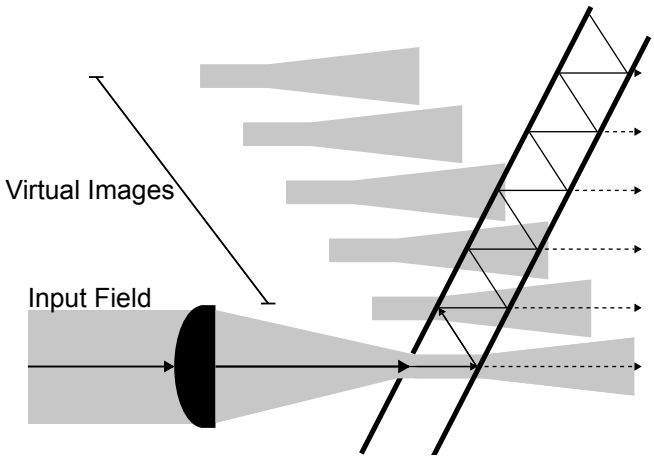

Fig. 4.2: A schematic of the Virtual Image representation of the VIPA. The different sources will interfere, leading to the interference pattern at the output of the VIPA.

Although the device is capable of providing a large angular dispersion versus wavelength, the device is based on interference patterns at the output of the VIPA. Since the interference pattern of interest is a local phenomenon at the focal plane of the focusing lens, non-idealities in the used materials, fabrication inaccuracies, lens misalignments, temperature dependencies, and off-broadside scanning angles at the input of the VIPA will introduce aberrations in the interference pattern shown at the focal plane of the VIPA [8] and [32]. In addition, the interference between the divergent beams does not lead to a single distribution for each wavelength. Each wavelength is produced at multiple higher order modes, in other words, the VIPA produces radiation of the same wavelength at different output angles. Usually, the fundamental mode contains almost all the energy available for a certain wavelength, however, the aforementioned non-idealities can change the distribution of energy between the different modes.

To show the extend of the aberrations and the higher order modes in the output of the VIPA, two cases will be presented here: the output of the VIPA focused on a center element of a Focal Plane Array (FPA) at the focal plane of the VIPA, and the output of the VIPA focused on an element at the edge of the same FPA. Since there is currently no working VIPA available, a mostly ideal model of the VIPA is used to generate outputs of the VIPA [34]. The model has generated fields for detectors with a 1 mm pitch, in other words, lenses with a diameter of 1 mm. These generated fields are evaluated at the focal plane of the focusing element after the VIPA (see Fig. 4.1), and should therefore still be propagated towards the surface of the silicon lenses of the lens-absorber.

At the center of an FPA the field shown in Fig. 4.3 is obtained. As visible, the field is dominated by its fundamental mode, which is focused in the center of the x-axis. There is a slight curve upwards when studying the side-lobes of the beam, which can be explained by the fact that this is a divergent beam propagating under an angle. As this beam propagates to the focal plane, it “smears” across the focal plane, leading to the slightly curved pattern. Studying the phase of this field, it is clear that the field is heavily dominated by a linear phase. Most of this phase can still be removed, as will be discussed in Sec. 4.2.

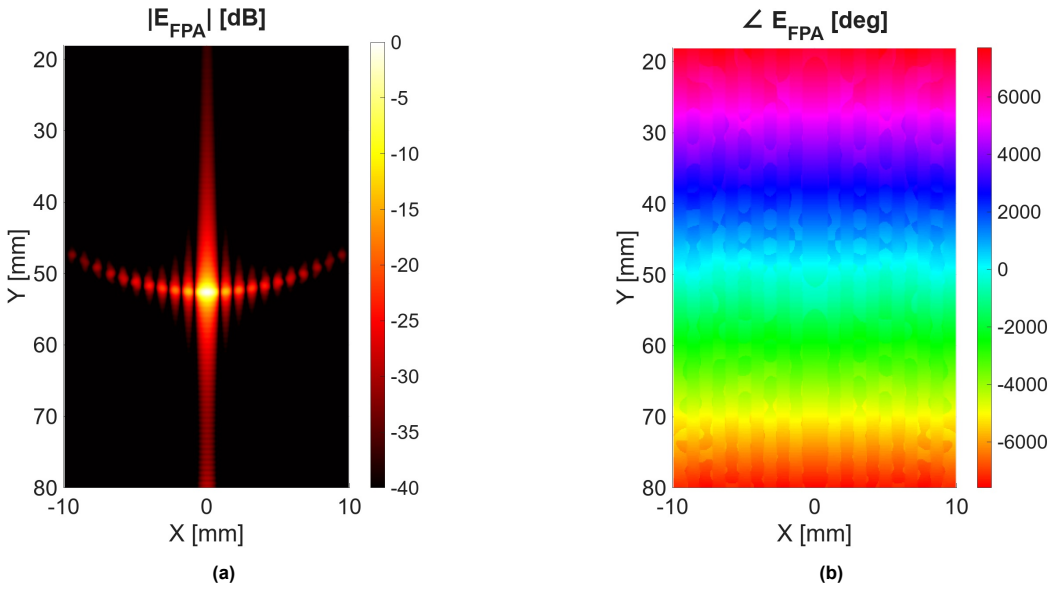

Fig. 4.3: Output of the VIPA for a center pixel at the focal plane of the focusing lens, at $\lambda_0 = 112\mu\mathrm{m}$: (a) amplitude, and (b) phase distributions for a center pixel.

At an edge pixel of an FPA the effect of larger scanning angles on the performance of the VIPA will become clearer. To show this, an output of the VIPA was generated towards the edge of the FoV of the VIPA: at spatial direction of $0.5°$ along the x-axis and at a spectral direction of $7.2°$ along the y-axis. This leads to the field shown in Fig. 4.4. Due to the steering in the transmitted field, the pattern has deteriorated further. The curvature in the pattern is much more present in Fig. 4.4a compared to Fig. 4.3a, and the main lobe has reshaped from more circular to elliptical, which will be studied in more

detail later. Although the phase is still dominated by a linear phase, as will be shown later, another phase component is also present which has an additional effect on the coupling to the detector.

Apart from the aberrations in the field due to the large scanning angle, another issue appears in this situation. As visible in Fig. 4.4a, apart from the fundamental mode, a second higher order mode has appeared in the output of the VIPA. This can cause issues at two levels: first of all, fields at this wavelength could also couple to detectors dedicated to observe a different frequency, limiting the FoV of the VIPA. A second problem involves the overall efficiency of the imaging-spectrometer. Due to this dominant higher order mode, almost 50% of the incoming field is transmitted to a higher order mode, this means that the overall efficiency for larger scanning angles will reduce by almost 50%. Even if the coupling between the VIPA and the detectors is ideal, the efficiency of the full system will still be affected by the scanning loss of the VIPA due to the higher order modes. Thus, maximising the coupling between the detector and the VIPA for these angles is necessary. On the other hand, VIPA designs that favour less power in higher order modes with more aberrated fundamental mode could also lead to overall better coupling performance.

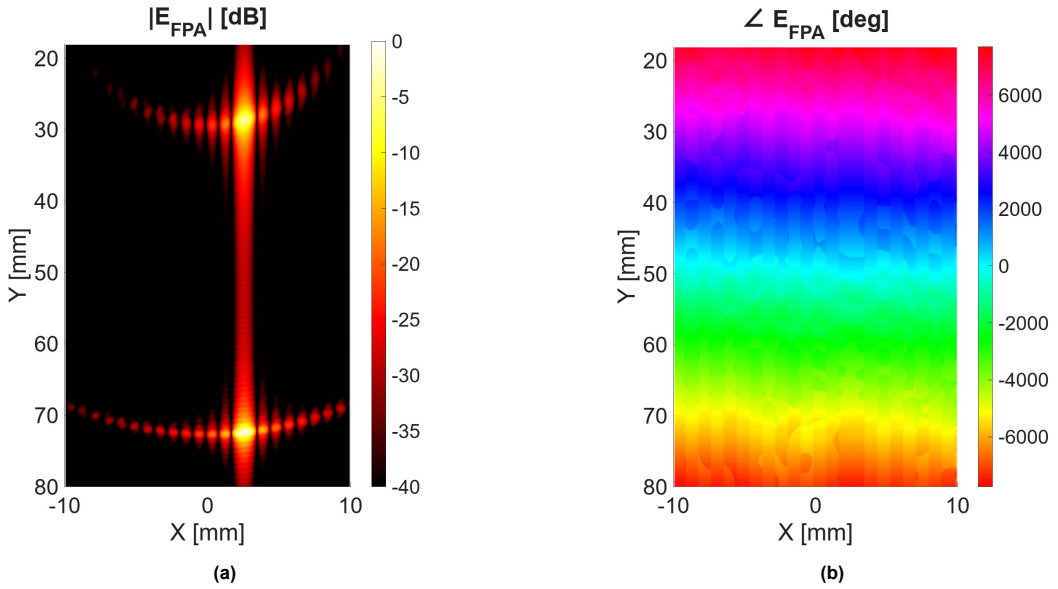

Fig. 4.4: Output of the VIPA for an edge pixel towards the edge of the FoV of the VIPA with a spatial direction of $0.5°$ along the x-axis at a spectral direction of $7.2°$ along the y-axis. This leads to the first mode propagating towards $x = 2.53\text{mm}$ and $y = 72.30\text{mm}$. The field is observed at the focal plane of the focusing lens at $\lambda_0 = 112\mu\text{m}$: (a) amplitude, and (b) phase distributions for an edge pixel.

To study these deteriorations in more detail, the field is studied as if focused onto a detector with an aperture-size of 1 mm. Moreover, the phase that varies linearly has been removed to study the more complex aberrations in the field, which leads to the field shown in Fig. 4.5. The reshaped main lobe that is focused on the lens is stretched to a more elliptical shape, the effect of this is negligible as the phase of the main lobe has more of an impact on the coupling to the detector. As shown in Fig. 4.5b, an additional diagonal phase shift with a slight curvature is part of the main lobe. This additional phase shift might reduce the coupling between the detector and the incoming field.

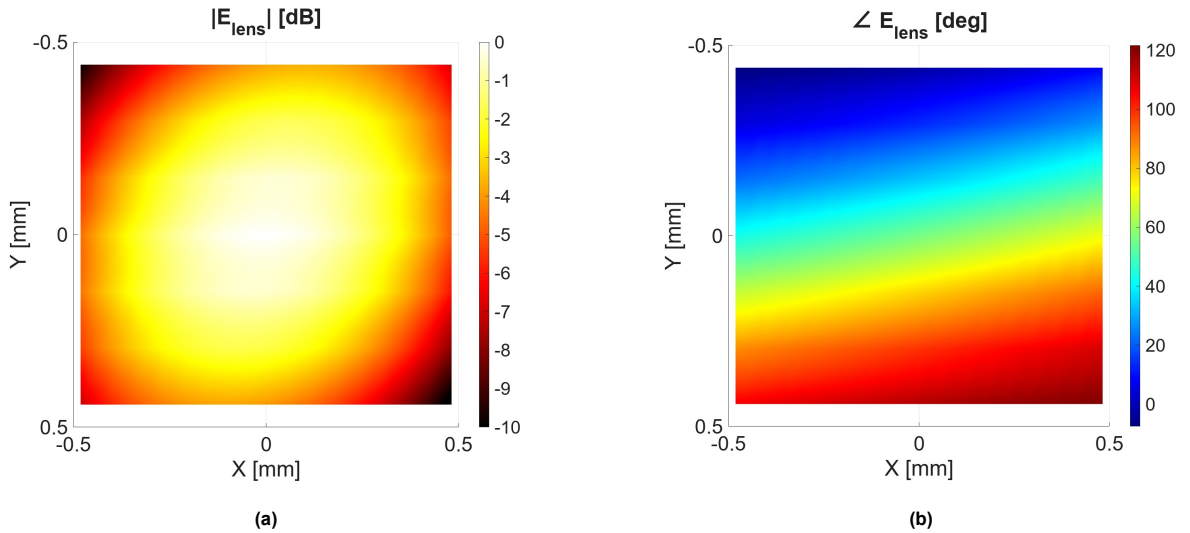

Fig. 4.5: Part of the main lobe of the fundamental mode in the output of the VIPA, with a footprint of $1\text{mm} \times 1\text{mm}$, which is the field captured by a lens with a diameter of $D_{lens} = 1\text{mm}$. The data is generated for an edge pixel towards the edge of the FoV of the VIPA with a spatial direction of $0.5°$ along the x-axis at a spectral direction of $7.2°$ along the y-axis. The field is observed at the focal plane of the focusing lens at $\lambda_0 = 112\mu\text{m}$: (a) amplitude, and (b) phase distributions without the linearly varying phase.

4.2. Optimisation Techniques

4.2.1. Linear Phase

The effect of a field with a linearly varying phase propagating into an elliptical lens can be observed as a lateral displacement along the focal plane of the lens. To mitigate the effect of this lateral displacement the absorber should be displaced along the focal plane to the new focus of the incoming field. In order to estimate where the absorber should be displaced towards, the position where the transmitted rays are focused, which will be referred to as the flash point, can be estimated by applying Snell's law [35].

For a plane wave propagating towards a lens with a direction of incidence defined by θ_{inc} and ϕ_{inc}, the direction of propagation of the field that is transmitted into the lens can be calculated using:

$$\theta_t = \sin^{-1}\left(\frac{1}{\sqrt{\epsilon_r}}\sin\theta_{inc}\right) \tag{4.1}$$

where ϵ_r is the relative permittivity of the material of the lens. From this direction of propagation and the distance between the focal plane and the top of the lens, the flash point can be approximated using:

$$\vec{\rho}_{fp}(\theta_{inc}, \phi_{inc}) = r(\theta = 0)\tan\theta_t\left(\cos\phi_{inc}\hat{x} + \sin\phi_{inc}\hat{y}\right) \tag{4.2}$$

where $r(\theta = 0)$ is the distance between the focal plane and the top of the lens. In the case of an elliptical lens, this distance can be determined using

$$r(\theta) = \frac{a(1-e^2)}{1 - e\cos\theta} \tag{4.3}$$

where a is the semi-major axis of the lens, e is the eccentricity of the lens given by $e = 1/\sqrt{\epsilon_r}$, and θ is the elevation angle that parameterizes the lens surface with respect to its lower focus. Substituting this equation into Eq. 4.2 results in the final expression to estimate the flash point in an elliptical lens:

$$\vec{\rho}_{fp}(\theta_{inc}, \phi_{inc}) = a(1+e)\tan\left(\sin^{-1}\left(\frac{1}{\sqrt{\epsilon_r}}\sin\theta_{inc}\right)\right)\left(\cos\phi_{inc}\hat{x} + \sin\phi_{inc}\hat{y}\right) \tag{4.4}$$

This equation is defined for a plane wave incident on the lens with a certain direction of incidence defined by θ_{inc} and ϕ_{inc}. The field coming from the VIPA can be approximated as a plane wave with a a linearly varying phase along the aperture of the lens. Due to this linearly varying phase, the incident field is equivalent to a plane wave propagating at a certain direction. As such, by determining the slope of the plane wave, an equivalent direction of propagation can be estimated.

For an incoming plane wave with a certain direction of incidence, the phase of the plane wave can be defined as

$$e^{-j\vec{k}\cdot\vec{r}} = e^{j\theta_{phase}(\vec{r})} \tag{4.5}$$

where $\vec{k} = k_0 \left(\sin\theta_{inc}\cos\phi_{inc}\hat{x} + \sin\theta_{inc}\sin\phi_{inc}\hat{y} + \cos\theta_{inc}\hat{z}\right)$, and $\theta_{phase}(\vec{r})$ is the linear phase on the plane wave as a function of the position along the aperture defined by $\vec{r}$. By evaluating the incoming field at $z = 0$, the equation can be rewritten and simplified to:

$$e^{-jk_0[x\sin\theta_{inc}\cos\phi_{inc}+y\sin\theta_{inc}\sin\phi_{inc}]} = e^{j\theta_{phase}(x,y)} \tag{4.6}$$

where x and y are positions at the aperture of the lens. Thus, by finding an expression for the phase on a planar surface, the linearly varying phase can be represented as an equivalent direction of propagation by solving:

$$k_0\left[x\sin\theta_{inc}\cos\phi_{inc} + y\sin\theta_{inc}\sin\phi_{inc}\right] = \theta_{phase}(x,y) \tag{4.7}$$

This direction of propagation, expressed by θ_{inc} and ϕ_{inc}, can be used in combination with Eq. 4.4 to find an estimate of the focus on the focal plane in the lens. This estimate can be used as an initial value to move the absorber along the focal plane, until the aperture efficiency of the device is maximised.

4.2.2. Complex Phase Aberrations

If the incoming field is dominated by more complex phase aberrations, displacement of the absorber along the focal plane alone will not improve the performance of the device effectively. More complex phase aberrations will introduce different phase depending on the location at the aperture, leading to a focal field that will no longer approach an airy pattern. To correct for these phase aberrations, the surface of the lens can be changed, such that each incoming ray will experience a different path length towards the focus of the lens. The different path lengths will apply a different phase for each ray, such that the phase matching can be improved, and therefore the reception of the resulting focal field can be improved.

Although it is possible to apply non-symmetrical shaping to lenses [35], this thesis will focus on rotationally symmetric shaping only to simplify the fabrication of the lenses. To implement this, the surface of the lens can be expressed as a conic surface with additional higher order polynomials [36]:

$$z = \frac{c\rho^2}{1+\sqrt{1+\kappa c^2\rho^2}} + a_0 + \sum_{i=1}^{N} a_i\rho^{2i} \tag{4.8}$$

where c is the curvature of the lens, κ is the conical constant of the lens, α_0 is the vertical offset of the surface, a_i are the N weights of the added polynomial, and $\rho = \sqrt{x^2+y^2}$ is the radial distance from the center of the lens. To optimise the surface of the lens, an optimisation algorithm is utilised that, for a given incident field, determines an optimal solution that minimises a certain cost function. Since this thesis' main focus is on the aperture efficiency of the detector, as discussed in Ch. 2, the cost function in this chapter will be defined as the inverse of the aperture efficiency for a given lens with a custom surface. Similar shaping techniques are validated and well understood in previous works for antenna based systems [36], [37], and [38].

To find an optimal shape of the lens, the GOFO technique discussed in Ch. 2 is used, where instead of an elliptical lens a lens with a surface defined using Eq. 4.8 is used. As an initial value, the optimiser

is initialised with an elliptical lens, such that $c = -\frac{a}{b^2}$, $\kappa = \left(\frac{b}{a}\right)^2$, and $a_0 = a + c$, where a and b are the semi-major and minor axes of the elliptical lens, respectively, and $c = a \cdot e$.

To optimise the lens for a certain incoming field, the incoming field is modelled as a plane wave at the aperture of the lens. To do so, the complex amplitude of the incoming field is used as the complex amplitude of the plane wave, leading to an incident field on the lens surface that resembles a plane wave with a non-uniform amplitude defined by

$$\vec{E}_{inc}(x, y) = E_{ap}(x, y) e^{-jk_0 \Delta d(x,y)} \hat{e} \tag{4.9}$$

where $E_{ap}(x, y)$ is the complex amplitude at the coordinates x and y of the aperture of the lens, $\Delta d(x, y)$ is the distance between the aperture of the lens and the surface of the lens at x and y, and $\hat{e}$ is the chosen polarisation of the incoming plane wave. For an illustration of this field incident on an arbitrary lens, refer to Fig. 4.6.

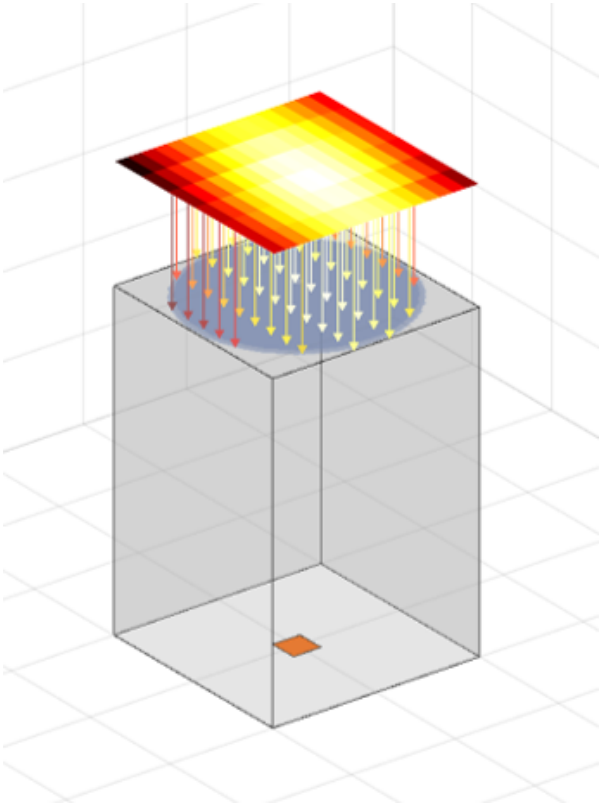

Fig. 4.6: An illustration of a lens-absorber fed by an incident field for which the surface of the lens should be optimised for. The silicon lens is represented as the gray coloured material, and focuses the incoming field onto the absorber located at the focal plane of the lens, indicated as an orange coloured rectangle. To propagate the incident field into the GOFO model, the incoming field is represented as a plane wave with a non-uniform amplitude equal to the complex amplitude of the incoming field, in other words, a plane wave where the complex amplitude depends on the x and y location of the surface of the lens.

4.3. Applying Optimisation Techniques to VIPA Fields

To study the effect of the proposed optimisation techniques on the presented VIPA fields in Sec. 4.1, a lens-absorber was modelled with an elliptical lens with a diameter of $D_{lens} = 1\text{mm}$ and an f-number of $f_\# = 2$. In addition, an ideal matching layer was added on top of the lens. Since the type of the absorber will only impact the maximum possible aperture efficiency that can be obtained, an ideal absorber with a side-length of $w = 2\lambda_d f_\#$ was placed at to focal point of the lens. As shown in Sec. 2.3.2, the power absorbed by an ideal absorber relates to the side-length of the absorber and to the field that is focused by the lens on top of the absorber domain. This simplifies the calculation of the aperture efficiency of the lens-absorber, and is therefore used to speed up any optimisation steps presented in this chapter.

As shown above, the incoming phase-front for both the center and edge pixel is dominated by a linearly varying phase shift. According to the method in Sec. 4.2.1, the effect of this phase-front can be practically removed by applying a lateral displacement to the absorber along the focal plane. To confirm this, the flash point for the center pixel was estimated by approximating the equivalent angle of incidence due to the linearly varying phase-front. The aperture efficiency was calculated for a range of lateral displacements around the initial estimate, leading to the result shown in Fig. 4.7. Using this method, the effect of the linearly varying phase has been reduced and the aperture efficiency has been increased from $\eta_{ap,center} = 81.9\%$ to $\eta_{ap,center} = 84.9\%$ for the center case.

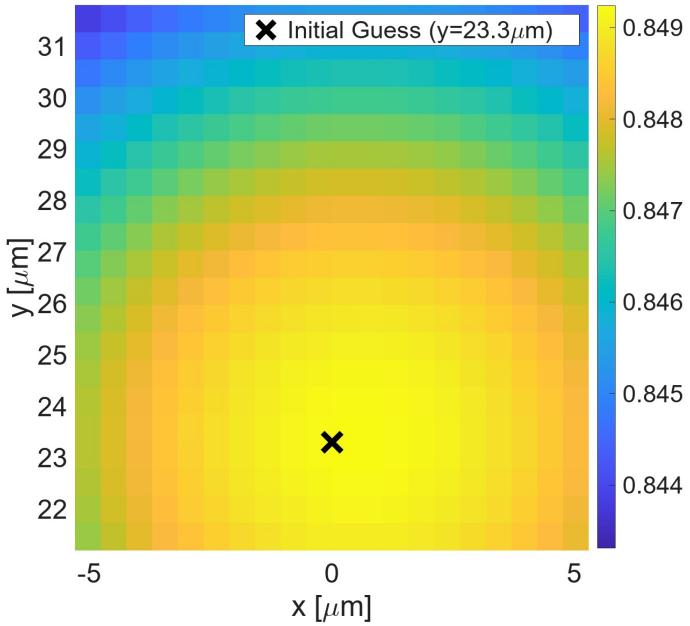

Fig. 4.7: The aperture efficiency (η_{ap}) of the lens-absorber for different lateral displacements, when evaluating the center case of the VIPA, with the initial guess highlighted using the black cross.

Next to this, the possibility to improve more complex phase-fronts is especially interesting. Therefore, for the remainder of this section, the focus will be purely on the lens-shaping technique presented in Sec. 4.2.2.

To test the impact of lens-shaping on the more complex phase aberrations, the linearly varying phase shifts have been removed from the VIPA fields, and the VIPA fields were propagated into the lens-absorber setup. For each generated lens surface the aperture efficiency was calculated, the inverse of which was used as a cost function to determine the quality of the found solution. Since there is a high number of solutions possible due to the high number of parameters in Eq. 4.8, the solution-set was limited by setting the bounds on the different parameters, which are provided in Tab. 4.1. It is worth mentioning that weights for higher order polynomials are related to their corresponding order leading to larger search ranges.

Parameter	Lower bound	Upper bound
c	$0.8c_{\text{elliptical}}$	$1.3c_{\text{elliptical}}$
κ	$0.8\kappa_{\text{elliptical}}$	$1.3\kappa_{\text{elliptical}}$
a_0	$0.8a_{0,\text{elliptical}}$	$1.3a_{0,\text{elliptical}}$
a_1	$-100\lambda_0$	$100\lambda_0$
a_2	$-1000\lambda_0$	$1000\lambda_0$
a_3	$-10000\lambda_0$	$10000\lambda_0$

Tab. 4.1: The bounds set on the possible values for different parameters of the lens-shaping optimisation, for a lens surface with a polynomial with 3 non-zero coefficients. The values $c_{\text{elliptical}}$, $\kappa_{\text{elliptical}}$, and $a_{0,\text{elliptical}}$ have been determined for an elliptical lens with a diameter of $D_{lens} = 1\text{mm}$ and an f-number of $f_{\#} = 2$.

After removing the linearly varying phase, the two cases have aperture efficiencies before applying any lens shaping of $\eta_{ap,center} = 84.9\%$ and $\eta_{ap,edge} = 82.0\%$ for the center and edge case, respectively. Since the difference between these two aperture efficiencies is small, and the efficiencies are close to what is maximally possible for an ideal absorber of side-length $w = 2\lambda_d f_{\#}$ as shown in Fig. 2.21, the effect of the complex aberrations in the phase-front is small.

After applying the lens-shaping optimisation on the two cases presented, the aperture efficiencies have been increased to $\eta_{ap,center} = 86.4\%$ and $\eta_{ap,edge} = 86.2\%$. To determine how this increase in efficiency was obtained, the shape of the lens should be studied. As shown in Fig. 4.8, the optimised lenses are both very similar. The lenses are still very close to an elliptical lens, and since the diameter of the lens was fixed to 1 mm, the lens' f-number has decreased. This means that, since the side-length of the absorber was fixed, the side-length has increased in terms of $\lambda_d f_{\#}$. Thus, following Fig. 2.21, the aperture efficiency has increased. This suggest that the optimiser is capable of finding more optimal lens-surfaces, and has done this by changing the f-number of the lens.

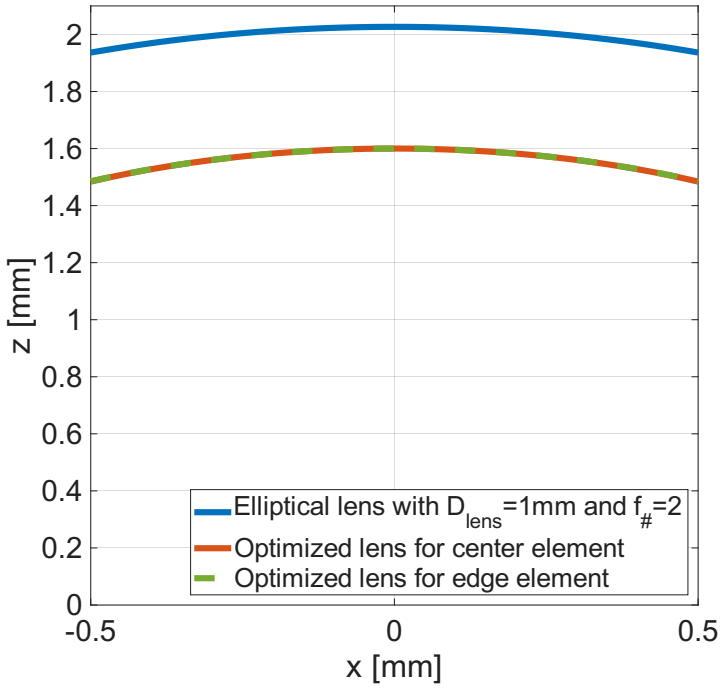

Fig. 4.8: The distance between the focal plane of the lens, and the surface of the lens, for an elliptical lens with $D_{lens} = 1\text{mm}$ and an f-number of $f_{\#} = 2$, and both optimised lenses for the center and edge elements respectively

The effect of this smaller f-number becomes especially apparent when comparing the focal field of the lens for the original elliptical lens, and the optimised lenses. Comparing Fig. 4.9a to Fig. 4.9b shows

that the lens focuses more of the field onto the same domain. This means that for the same absorber size, a larger fraction of the incoming power is received by the absorber.

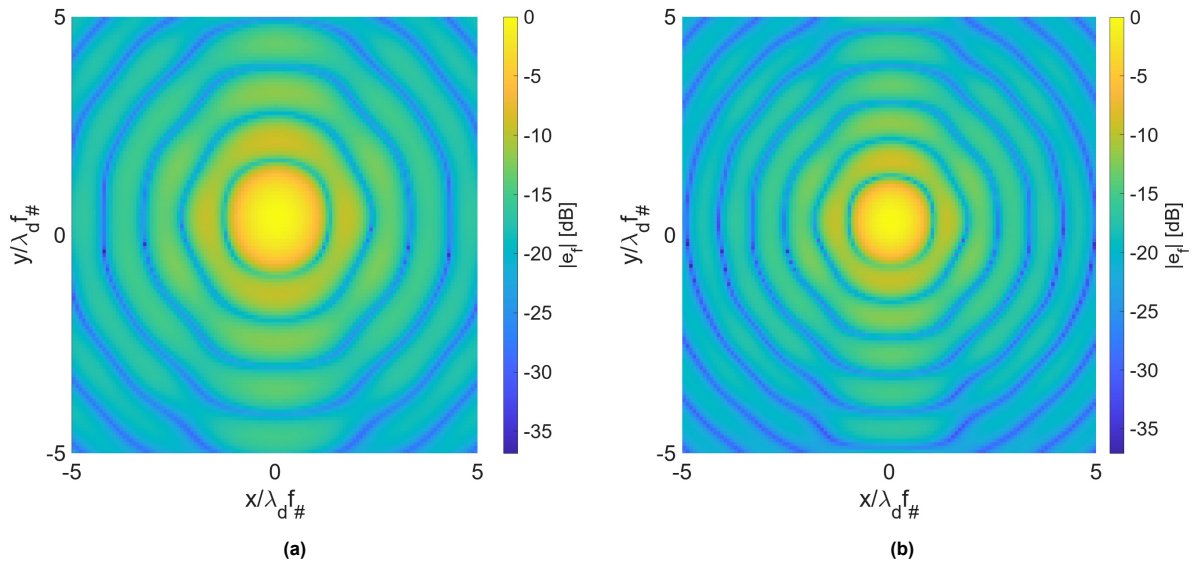

Fig. 4.9: (a) The focal field obtained from the original elliptical lens with $D_{lens} = 1\text{mm}$ and $f_{\#} = 2$, and (b) from the optimised lens for the center pixel.

Although the aperture efficiency is improved as shown above, the focusing efficiency decreases as the effective size of the absorber increases in terms of $\lambda_d f_{\#}$ as the f-number of the lens decreases. In case the focusing efficiency should not deteriorate during the optimisation, the inverse of the focusing efficiency could be added to the optimisation algorithm as a second cost function.

A full overview of the aperture efficiency of both the center and edge case before any optimisations and after applying each additional optimisation step can be found in Tab. 4.2.

	No optimisation	**Displacement of Absorber**	**Displacement and Lens Shaping**
$\eta_{ap,\textbf{center}}$	81.9%	84.9%	86.4%
$\eta_{ap,\textbf{edge}}$	79.0%	82.0%	86.2%

Tab. 4.2: The aperture efficiency for the center case ($\eta_{ap,\text{center}}$) and the edge case ($\eta_{ap,\text{edge}}$) before any optimisation, and after applying an additional optimisation step

4.3.1. Discussion on the Coupling Between VIPA and Lens-Absorbers

Although there are phase aberrations in the VIPA fields presented in this chapter, the aperture efficiency of the lens-absorber does not seem to be affected much, as shown in Tab. 4.2. This could be explained by the fact that absorbers are less sensitive to phase than antennas, however, it should be taken into account here that the model that is used to generate the fields is relatively ideal. Any non-idealities such as non-uniform refraction indexes and fabrication errors such as misalignments of the optical components are not taken into account, and could in theory reduce the quality of the field transmitted by the VIPA further, especially once the angle of incidence on the VIPA is increased. Since more power will be lost to higher order modes of the VIPA, as shown here close to 50% is lost reducing the effective aperture efficiency of the edge case to $\approx 43.1\%$, it is important to maximise the coupling between the VIPA and the detectors. Moreover, as mentioned before, the possibility to modify and correct for the phase aberrations in the VIPA output using the surface of lens FPAs, opens up a new design route for the VIPA. In particular, VIPA designs with less power at their higher order modes at the cost of more aberrations in the main mode could lead to much better overall optical coupling.

Once a more realistic model is employed for the VIPA, or once actual measurements have been performed on a fabricated VIPA, further research should be done on the coupling to the lens-absorbers. In the case that the coupling reduces for non-ideal scenarios, the techniques presented in this chapter can be used to analyse and improve the performance of the real instrument.

5

Analysing the Modal Description of Multi-Mode Detectors

A power detector is usually sensitive to a field in a certain state of coherence. This state of coherence, which can be described by a incoherent superposition of modes, can be defined as the modal description of a power detector. A mode in this context is a solution of Maxwell's equations, defining a radiative, coherent field which has a specific definition of its electric and magnetic fields. For most antenna-based detectors, this modal description is simple as most behave as single mode devices. For the detectors discussed in this thesis a single mode description is no longer accurate. Absorber based detectors in particular are usually multi-moded, having sensitivities to multiple modes.

While this multi-mode behaviour allows the detector to capture incoming power from more modes, it also subjects the detector to unwanted incoming radiation in the form of thermal noise from the optical chain and cryostat, stray-light spilled into the instrument, and sources from unwanted directions scattering towards the detector. Moreover, as each optical device in the optical chain has its own modal description, the modal description of the lens-absorber could describe how the detector couples to the optical chain of the instrument.

To help understanding how multi-mode detectors couple to certain modes and unwanted radiation, a modal description of the detectors is needed. A technique capable of extracting such a description is the Energy Absorption Interferometry (EAI) technique [39], which is an experimental technique that can be described as aperture interferometry in reverse. Although EAI is an experimental technique, to better understand the meaning behind the modal description a model is needed that can reproduce the modal description obtained by EAI. Since constructing such a model requires many simulations of the detector under test, employing the GOFO and Floquet Wave based techniques discussed in this thesis would speed up the process drastically.

5.1. EAI theory

When a detector is illuminated by an arbitrary incoming field, the field can be represented by an angular distribution, $\vec{E}$. The power received by this detector can be described as [39]:

$$P = \iint \overline{\overline{DRF}}^{\dagger}(\hat{\Omega}_1, \hat{\Omega}_2) : \overline{\overline{\mathcal{E}}}(\hat{\Omega}_1, \hat{\Omega}_2)\, \mathrm{d}^2\hat{\Omega}_1\, \mathrm{d}^2\hat{\Omega}_2 \tag{5.1}$$

where the double dot denotes complete tensor contraction, † is the Hermitian adjoint, and $\Omega_{1/2}$ indicate two directions of incidence of the incoming field. This equation will be simplified later in this section, and is needed to introduce the working principle of EAI. In this equation, the incoming field is described by the angular correlation dyadic of the electric field on top of the detector:

$$\overline{\overline{\mathcal{E}}}(\hat{\Omega}_1, \hat{\Omega}_2) = \left\langle \vec{E}(\hat{\Omega}_1)\vec{E}^*(\hat{\Omega}_2) \right\rangle \tag{5.2}$$

where $\langle . \rangle$ represents the ensemble average over the directions $\Omega_{1/2}$, and $\overline{\overline{DRF}}(\hat{\Omega}_1, \hat{\Omega}_2)$ is a dyadic function describing the response of the device to an arbitrary field. This Detector Response Function (DRF) can be interpreted as a second-order correlation function describing the sensitivity to spatial correlations in the incoming field.

All partially-coherent fields can be decomposed as a set of spatially coherent fields, which are referred to as coherent modes [39] and [40]. Since the incoming field $\vec{E}$ can be assumed to be at least partially coherent, and the DRF is the correlation function of this field, the DRF itself can be decomposed in a similar fashion. This decomposition describes the DRF by a set of eigenvalues and eigenfunctions, described as:

$$\overline{\overline{DRF}}(\hat{\Omega}_1, \hat{\Omega}_2) = \sum_m \alpha_m R_m(\hat{\Omega}_1) R_m^*(\hat{\Omega}_2) \tag{5.3}$$

In this decomposition, the eigenvalues α_m describe the power carried in mode m, while eigenfunction R_m describes the pattern of the mth natural mode of the detector. Thus, by obtaining the DRF, the modal description of the detector can be obtained.

5.1.1. Obtaining the DRF

Since the DRF can be described as a correlation function, each element in the DRF can be obtained by manually performing the spatial correlation of two sources, and finding the power absorbed by the detector for each combination of source positions.

When the detector is illuminated by two plane wave sources, propagating from directions $\hat{\Omega}_1$ and $\hat{\Omega}_2$, the incident field on top of the detector can be represented by:

$$\begin{aligned} \vec{E}_{inc}(\hat{\Omega}_1, \hat{\Omega}_2) &= \vec{E}_1(\hat{\Omega}_1) + \vec{E}_2(\hat{\Omega}_2) \\ &= E_1 e^{-j\vec{k}_1\cdot\vec{r}} e^{-j\Delta\phi/2}\hat{p}_1 + E_2 e^{-j\vec{k}_2\cdot\vec{r}} e^{j\Delta\phi/2}\hat{p}_2 \end{aligned} \tag{5.4}$$

where $E_{1/2}$ represent the complex amplitudes, $\hat{p}_{1/2}$ the polarisations, and $\Delta\phi$ the phase difference between the plane waves which is assumed to be controllable, and $\vec{k}_{1/2}$ are the propagation vectors corresponding to directions $\hat{\Omega}_{1/2}$. For different directions of incidence, this field will form a fringe on top of the device. This field will propagate into the device, and the response to it will form an element in the DRF.

The DRF itself is a complex function, as it will describe the response to a complex incident field. Since the detectors under test are only capable of measuring the power of an incident field, any phase information is lost and therefore the argument of each element in the DRF cannot be directly extracted. In order to obtain the argument of each element in the DRF, the possibility to control the phase difference between the two sources is used.

The power that is absorbed by the detector when illuminated by the incident field of Eq. 5.4 can be described by [39]:

$$\begin{aligned} P =& |E_1|^2 \left[\hat{p}_1 \cdot \overline{\overline{DRF}}(\hat{\Omega}_1, \hat{\Omega}_1) \cdot \hat{p}_1\right] + |E_2|^2 \left[\hat{p}_2 \cdot \overline{\overline{DRF}}(\hat{\Omega}_2, \hat{\Omega}_2) \cdot \hat{p}_2\right] \\ &+ 2\Re\left\{E_1^* E_2 e^{j\Delta\phi} \hat{p}_1 \cdot \overline{\overline{DRF}}(\hat{\Omega}_1, \hat{\Omega}_2) \cdot \hat{p}_2\right\} \end{aligned} \tag{5.5}$$

The most interesting term in this equation is the third term, which can be rewritten for clarity as:

$$\begin{aligned} P_{3rd} &= 2\Re\left\{E_1^* E_2 e^{j\Delta\phi} \hat{p}_1 \cdot \overline{\overline{DRF}}(\hat{\Omega}_1, \hat{\Omega}_2) \cdot \hat{p}_2\right\} \\ &= \left|A(\hat{\Omega}_1, \hat{\Omega}_2)\right| \cos\left(\Delta\phi + \operatorname{Arg} A(\hat{\Omega}_1, \hat{\Omega}_2)\right) \end{aligned} \tag{5.6}$$

where $A(\hat{\Omega}_1, \hat{\Omega}_2)$ is the complex amplitude due to the incoming plane waves and the DRF for directions $\hat{\Omega}_1$ and $\hat{\Omega}_2$. The detector output will trace a cosine as the controllable phase difference $\Delta\phi$ is varied from 0 to 360 degrees. The incoming plane waves will, in combination with the applied DRF, introduce an additional phase shift. Thus, by extracting the amplitude and phase of the cosine that results from sweeping $\Delta\phi$, the complex elements in the DRF can be found, which are consequently equal to:

$$\begin{aligned} \left|A(\hat{\Omega}_1, \hat{\Omega}_2)\right| &= 2\,|E_1|\,|E_2| \left|\hat{p}_1 \cdot \overline{\overline{DRF}}(\hat{\Omega}_1, \hat{\Omega}_2) \cdot \hat{p}_2\right| \\ \operatorname{Arg} A(\hat{\Omega}_1, \hat{\Omega}_2) &= \operatorname{Arg}\left(E_1^* E_2 \hat{p}_1 \cdot \overline{\overline{DRF}}(\hat{\Omega}_1, \hat{\Omega}_2) \cdot \hat{p}_2\right) \end{aligned} \tag{5.7}$$

5.2. Modelling EAI Measurements

As described in Eq. 5.6 and Eq. 5.7, obtaining an accurate representation of the DRF of a device under test relies on multiple different parameters. The device has to be illuminated by two sources, scanning the aperture of the complete device. For each source combination, the phase difference between the sources has to be varied between 0 and 360 degrees. The combination of all this data leads to a highly dimensional dataset.

The DRF itself will be used to create a modal representation of the device under test, this modal representation has to be obtained using the decomposition in Eq. 5.3. As will be discussed later in this section, the method used to obtain this decomposition is called the Singular Value Decomposition (SVD). This method will be more effective the more data there is available, and it is difficult to predict the resolution of the data required to converge to an accurate modal description of the device.

Combining the amount of data required per measurement with the uncertainties measurements themselves introduce, trying to get an understanding of the meaning behind the modal description, and how this modal description can be used to further aid in the analysis and optimisation of Quasi-Optical systems is a difficult task. Therefore, the decision was made to introduce a model that can be used to perform EAI on various Quasi-Optical systems, to start an initial investigation into EAI, the meaning behind the DRF and its modal description, and to establish a baseline for future measurements with the EAI technique.

5.2.1. Analysis of the EAI Modelling Tool

The detector under test is illuminated by two plane waves, $\vec{E}_1$ and $\vec{E}_2$ as described in Eq. 5.4. The angles of incidence, polarisation, and additional phase of these two plane waves can each be varied. After combining the two plane waves at the surface of the device under test, the resulting field $\vec{E}_{inc}$ has a unique set of complex amplitudes and directions of propagation depending on the location at the aperture of the device. The complex amplitudes are determined by simply adding the components of each of these plane waves. The directions of propagation are determined by calculating the Poynting vector of the newly constructed field:

$$\vec{S} = \frac{1}{2}\Re\left\{\vec{E}_{inc} \times \vec{H}^*_{inc}\right\} \tag{5.8}$$

where $\vec{H}_{inc}$ is the magnetic component of the field at the aperture of the device under test. This magnetic field is constructed by combining the magnetic fields of the incoming plane waves, each of which is calculated using:

$$\vec{H}_{PW} = \frac{1}{\eta_0}\hat{s}_{PW} \times \vec{E}_{PW} \tag{5.9}$$

where η_0 is the characteristic impedance of free space, and $\hat{s}_{PW}$ is the direction of propagation of the incoming plane wave. After calculating the Poynting vector using the incident electric and magnetic field, the directions of propagation of the incident field are calculated using:

$$\hat{s}_{inc} = \frac{\vec{S}}{|\vec{S}|} \tag{5.10}$$

This newly constructed field is propagated using the GOFO model described in Ch. 2, which can be coupled to any detector, such as an antenna or one of the absorbers designed in this thesis. The power received by the detector is used to calculate each element in the DRF. As stated in Sec. 5.1.1, each element in the DRF is a complex value, which is obtained by varying the phase difference $\Delta\phi$ between the two incident plane waves. Storing the power received for each value of $\Delta\phi$ leads to a cosine with an associated amplitude and phase. For actual measurement scenarios, this cosine will have a frequency depending on how fast $\Delta\phi$ is swept between 0 and 360 degrees. In addition, any inaccuracies due to the measurements and noise mean that the amplitude and phase should be extracted by fitting the data to a cosine [41]. In this model, there is no duration associated to the frequency sweep, and no

noise will be present in the data. Therefore, in order to extract the amplitude and phase of the cosine, the Discrete Fourier Transform (DFT) is used instead.

Since the first element of this transform equals the 0 Hz component, the second element contains the amplitude and phase information of the cosine in terms of $\Delta\phi$. From this element in the DFT, the amplitude and phase of this cosine are defined as:

$$\begin{aligned} \left|A(\hat{\Omega}_1, \hat{\Omega}_2)\right| &= \frac{2\left|\mathcal{F}_2\left\{P_{RX}\left(\hat{\Omega}_1, \hat{\Omega}_2, \Delta\phi\right)\right\}\right|}{N} \\ \operatorname{Arg} A(\hat{\Omega}_1, \hat{\Omega}_2) &= \operatorname{Arg}\left(\mathcal{F}_2\left\{P_{RX}\left(\hat{\Omega}_1, \hat{\Omega}_2, \Delta\phi\right)\right\}\right) \end{aligned} \tag{5.11}$$

where $\mathcal{F}_2\left\{P_{RX}\left(\hat{\Omega}_1, \hat{\Omega}_2, \Delta\phi\right)\right\}$ is the second element of the Discrete Fourier Transform of the received power, and N are the number of samples in $P_{RX}\left(\hat{\Omega}_1, \hat{\Omega}_2, \Delta\phi\right)$. Afterwards, using the definitions discussed in Sec. 5.1.1, the DRF of the device under test is constructed.

To obtain the complete DRF, the two sources are scanned across a large enough domain along the aperture of the device under test. This can be done either by scanning the sources along a plane, or by scanning it in spherical coordinates, and vary the elevation and azimuthal angles of the sources. The effect of the size of the domain on the resulting DRF will be discussed in Sec. 5.2.2. Since any pattern in reception in this thesis is represented with respect to the spherical coordinates θ and ϕ, the remainder of this chapter will scan the sources in the spherical coordinate system. This allows for easier comparison with previously observed results.

5.2.2. Extracting the Modal Description

As described in Sec. 5.1, a modal description of the device under test can be constructed by deriving the eigendecomposition of the DRF. Since the derived DRF is not necessarily a diagonizable matrix, especially in the case where the DRF is derived from measurements, the eigendecomposition cannot be directly computed. Instead, the Singular Value Decomposition (SVD) is applied that is capable of performing an equivalent decomposition to the eigendecomposition of any DRF. Although the SVD is commonly defined for decompositions of matrices, an equivalent SVD exists for tensor datasets as defined in [42], which will be needed once the DRF of the full aperture of the device is constructed. However, as will be discussed later, the focus in this chapter will be on extracting the DRF for plane waves incident from single ϕ-cuts, leading to a DRF in matrix form. Thus, for the remainder of this section, the matrix form SVD will be discussed. Due to the equivalence between the tensor form SVD and the matrix form SVD, any conclusions drawn in this section will also hold for the tensor form SVD.

The SVD is defined as a factorization of the $k \times l$ matrix DRF in the form of:

$$DRF = USV^{\dagger} \tag{5.12}$$

where U is a $k \times k$ complex unitary matrix, S is a $k \times l$ diagonal matrix, and $V^{\dagger}$ is the conjugate transpose of V, which is an $l \times l$ complex unitary matrix. The matrices U and S are particularly important in relation to the eigendecomposition shown in Sec. 5.1. The columns in the matrix U can be related to the eigenfunctions $R_m(\hat{\Omega}_1)$ of the DRF, where the elements in the diagonal of S relate to the eigenvalues α_m of the DRF. Since the two sources in this model will be swept across the same domain, the choice was made to use the same number of samples per source, thus the dimensions of the resulting DRF will be equal to one another (in the equation above it means that $k = l$). This allows for a same order of resolution in terms of number of modes as in the resolution of the patterns extracted.

There is a side-effect on the accuracy by using this decomposition. Specifically, the accuracy of the patterns of each of the modes and the number of modes extracted are heavily impacted by the amount of data stored in the DRF. Combining this large dataset with the fact that the phase difference between the sources will have to be swept for each combination of source locations to extract the argument of each element in the DRF, the total dataset will be even larger. Therefore, the decision was made to only

focus on single ϕ-cuts for the simulations and validations in this thesis. This leads to a DRF that is no longer in tensor form but in matrix form, reducing the number of simulations. Although this could have an effect on the accuracy of the extracted modal description since a complete dimension is missing from the DRF, it does allow for initial studies on the results of the EAI model.

5.3. Validating the EAI Modelling Tool

Before any initial experiments could be done with the EAI tool, a test case had to be analysed to validate the EAI tool, and to explore the modal descriptions that can be produced from a generated DRF. In order to validate the EAI tool, the DRF of a source had to be generated that is already well understood. Since any type of absorber, which is a multi-moded device, is not well described, a single moded device was selected instead: an ideal Gaussian Beam coupled to an elliptical lens as seen in Fig. 5.1.

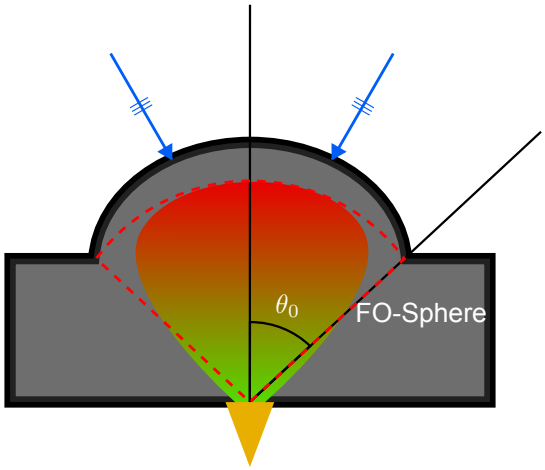

Fig. 5.1: An illustration of performing EAI on the Gaussian fed lens-antenna. The power received by the antenna from the two incoming plane waves (indicated by the two arrows) is calculated by applying an antenna in reception formalism between the field in transmission of the Gaussian feed, and the GO-fields evaluated on the FO-sphere indicated by the red dashed lines.

The lens, which is a Silicon elliptical lens with a diameter of 1.5mm and an f-number of 2, is coupled to a Gaussian beam which is defined as:

$$\vec{E}_{gauss} = E_0 e^{-\left(\left(\frac{u}{u_0}\right)^2+\left(\frac{v}{v_0}\right)^2\right)}(\sin\phi\hat{\theta}+\cos\phi\hat{\phi}) \tag{5.13}$$

where u_0 and v_0 are the parameters defining the directivity of the beam, E_0 is the amplitude of the electric field, and $u = \sin\theta\cos\phi$ and $v = \sin\theta\sin\phi$ are the UV coordinates defined in terms of the spherical coordinates θ and ϕ. For this detector, the directivity of the feed has been designed for a good match to the lens, thus, $u_0 = v_0$ such that the normalised farfield of the Gaussian feed is -11dB at $\theta = \theta_0$.

In order to construct the DRF, the power received by the Gaussian feed is evaluated. To calculate this power, antenna in reception formalism is applied as discussed in [13]. Here, a reaction integral on the FO-sphere is evaluated that defines the Thévenin open circuit voltage V_{oc} of the antenna:

$$V_{oc}(\theta,\phi)I_0 = \frac{2}{\eta_d}\int_0^{2\pi}\int_0^{\theta_0}\vec{E}^{Tx}_{gauss}(\theta,\phi)\cdot\vec{E}_{GO}(\theta,\phi)R^2_{FO}\sin\theta\,\mathrm{d}\theta\,\mathrm{d}\phi \tag{5.14}$$

where η_d is the characteristic impedance of the Silicon lens, $\vec{E}^{Tx}_{gauss}$ is the farfield of the Gaussian antenna in transmission, $\vec{E}_{GO}$ are the GO-fields on the FO-sphere, and R_{FO} is the radius of the FO-sphere. $\vec{E}^{Tx}_{gauss}$ is calculated by propagating the Gaussian field $\vec{E}_{gauss}$ defined in Eq. 5.13 to the FO-sphere. With the open-circuit voltage obtained, the power delivered to the load can be calculated using:

$$P_L = \frac{|V_{oc} I_0|^2}{16 P_{rad}} \tag{5.15}$$

where I_0 is an arbitray current used to feed the antenna, and P_{rad} is the total power radiated by the Gaussian feed, in case it is fed with a current I_0, defined as:

$$P_{rad} = \frac{1}{2\eta_d} \int_0^{2\pi} \int_0^{\pi} \left| \vec{E}^{TX}_{gauss} \right|^2 R_{FO}^2 \sin\theta \, \mathrm{d}\theta \, \mathrm{d}\phi \tag{5.16}$$

With this model for the Gaussian feed in place, EAI could be applied to extract the DRF of the lens-antenna. As stated in Sec. 5.2.2, the EAI tool designed is only used to extract single ϕ-cuts from devices under test, due to the highly dimensional datasets that EAI generates. Therefore, three different ϕ-cuts were simulated to validate and explore the modal descriptions generated by the method: $0°$, $45°$, and $90°$.

5.3.1. Modal Description of Gaussian-Beam Fed Lens

After running the EAI tool for the three different scenarios ($\phi = 0°$, $\phi = 45°$, and $\phi = 90°$), the modal description of the device was extracted by evaluating the Singular Value Decomposition on the obtained DRFs to perform a similar decomposition as seen in Eq. 5.3. This resulted into three different values: U, S, and V. The columns of U and the columns of V can be interpreted as $R_m(\hat{\Omega}_1)$ and $R_m(\hat{\Omega}_2)$ respectively, and the elements on the diagonal of the diagonal matrix S can be interpreted as α_m ($\alpha_m = S_{mm}$).

The values in S can be described as a sensitivity of the detector to the mth spatial mode, and is best evaluated by normalising these values to the sensitivity to the first spatial mode, and describing the other modes in terms of this first mode. Doing this for the three cases described before, leads to the results shown in Fig. 5.2, where the sensitivities of the detector to first 10 spatial modes relative to the first spatial mode are shown.

The first notable observation, is that the detector is clearly very few-moded. The higher order modes after the first mode drop off quickly, correlating with the fact that the Gaussian feed is a single moded device. There is an interesting phenomenon visible when observing the first few higher order modes: for the $\phi = 0°$ case, the device seems to be less sensitive to these modes than for the other 2 cases. In order to explain this, the patterns associated with these modes should be studied.

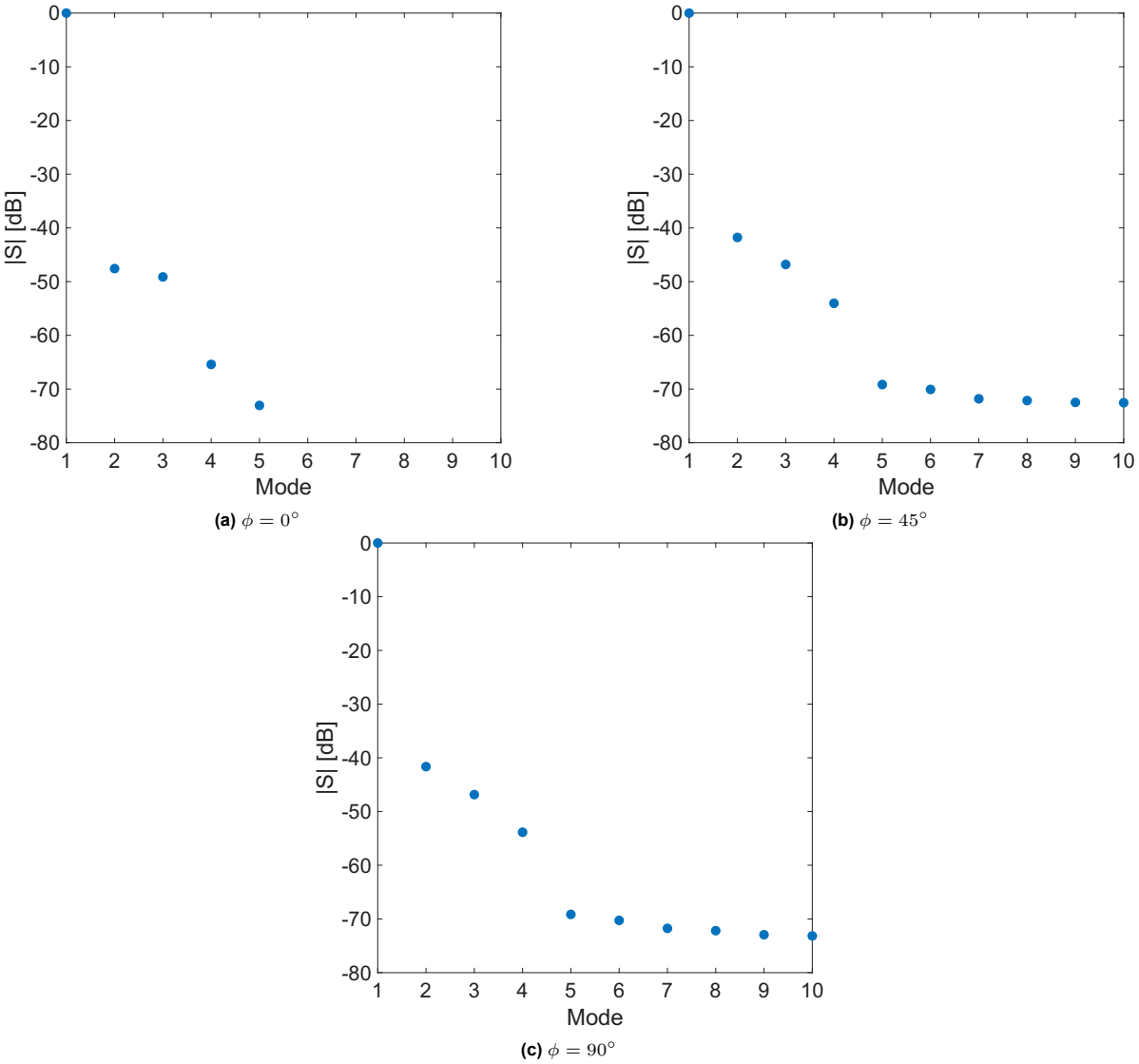

(a) $\phi = 0°$ **(b)** $\phi = 45°$ **(c)** $\phi = 90°$

Fig. 5.2: The sensitivities of the Gaussian fed lens to the first 10 spatial modes, normalised to the sensitivity of the device to the first spatial mode, for three different ϕ-cuts: (a) $\phi = 0°$, (b) $\phi = 45°$, and (c) $\phi = 90°$

In order to extract the patterns for each of these modes, the eigenfunctions described by the columns of $U(= R_m(\hat{\Omega}_1))$ should be studied. By multiplying each of these eigenfunctions with their associated eigenvalues stored in S, an equivalent to the patterns in reception for each of these modes can be calculated. For the three ϕ-cuts, these patterns are shown in Fig. 5.3 for the first 5 spatial modes.

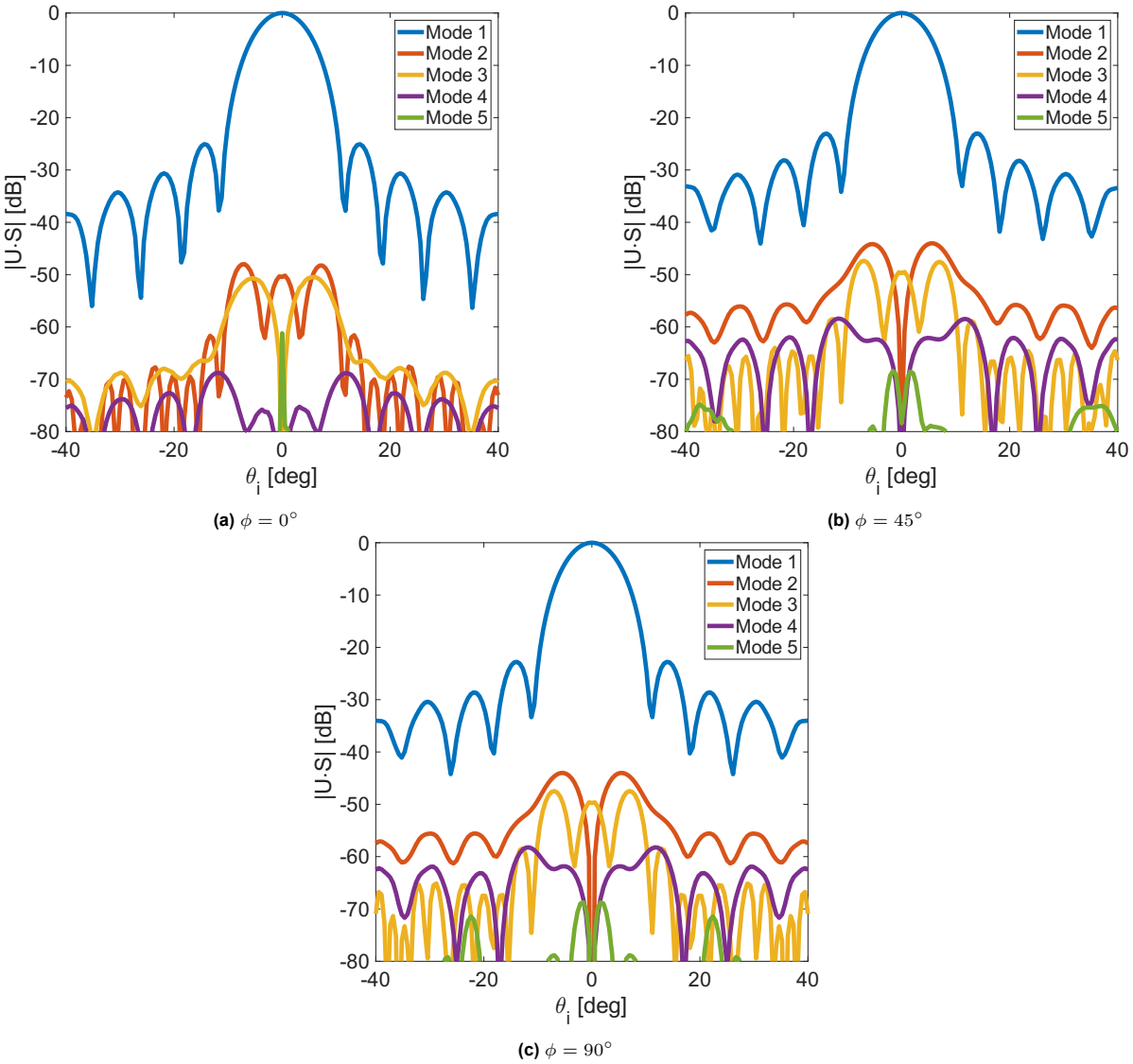

(a) $\phi = 0°$

(b) $\phi = 45°$

(c) $\phi = 90°$

Fig. 5.3: The patterns of the first 5 spatial modes of the Gaussian fed lens antenna, extracted for three different ϕ-cuts: (a) $\phi = 0°$, (b) $\phi = 45°$, and (c) $\phi = 90°$

Another confirmation that the EAI method is able to extract the single moded device, is that the patterns of the first spatial mode as shown in Fig. 5.3 are very close to the pattern one would expect for the Gaussian fed lens: a pattern close to an airy pattern. By studying the sensitivities shown in Fig. 5.2, a difference was observed between the higher order modes for the $\phi = 0°$ case and the other two cases. The same difference can be observed by comparing Fig. 5.3a to Fig. 5.3b and Fig. 5.3c. In the latter two cases, a pattern more similar to a cross-polarisation pattern can be observed, which is less prominent when studying Fig. 5.3a. This has to do with the incoming polarisation of the plane waves used to scan each of these cuts. For a plane wave, the polarisation can be set to have either a θ or ϕ polarisation, this is done by choosing η to be either 0 or $\pi/2$ respectively in the following equation:

$$\hat{p}_i = \cos\eta\hat{\theta} + \sin\eta\hat{\phi} \tag{5.17}$$

This equation can be converted to a vector in cartesian coordinates for clarity, resulting in:

$$\hat{p}_i = \begin{cases} \cos\theta_i\cos\phi_i\hat{x} + \cos\theta_i\sin\phi_i\hat{y} - \sin\theta_i\hat{z}, & \text{for } \eta = 0 \\ -\sin\phi_i\hat{x} + \cos\phi_i\hat{y} & \text{for } \eta = \pi/2 \end{cases} \tag{5.18}$$

In order to couple best to the Gaussian feed, the incoming plane waves should be mostly y-polarised. For the $\phi = 0°$ case this is possible by selecting a plane wave that is ϕ polarised ($\eta = \pi/2$), however, for the other two cases, the incoming plane wave will always contain more than 1 polarisation in cartesian coordinates. Thus, such incoming plane waves couple more to the cross-polarisation response of the Gaussian fed lens, resulting in a more prominent cross-polarisation in the modal description.

Since the EAI tool developed is capable of extracting the different spatial modes of a device under test, a final validation is performed to reconstruct the total pattern in reception. To do so, the spatial patterns shown in Fig. 5.3 are superpositioned incoherently:

$$P = \sum_m |U_m \cdot S_{mm}|^2 = \sum_m |R_m \cdot \alpha_m|^2 \tag{5.19}$$

where U_m is the mth column of the matrix U. In Fig. 5.4, for the three described ϕ-cuts, the patterns in reception are compared to the output of Eq. 5.19.

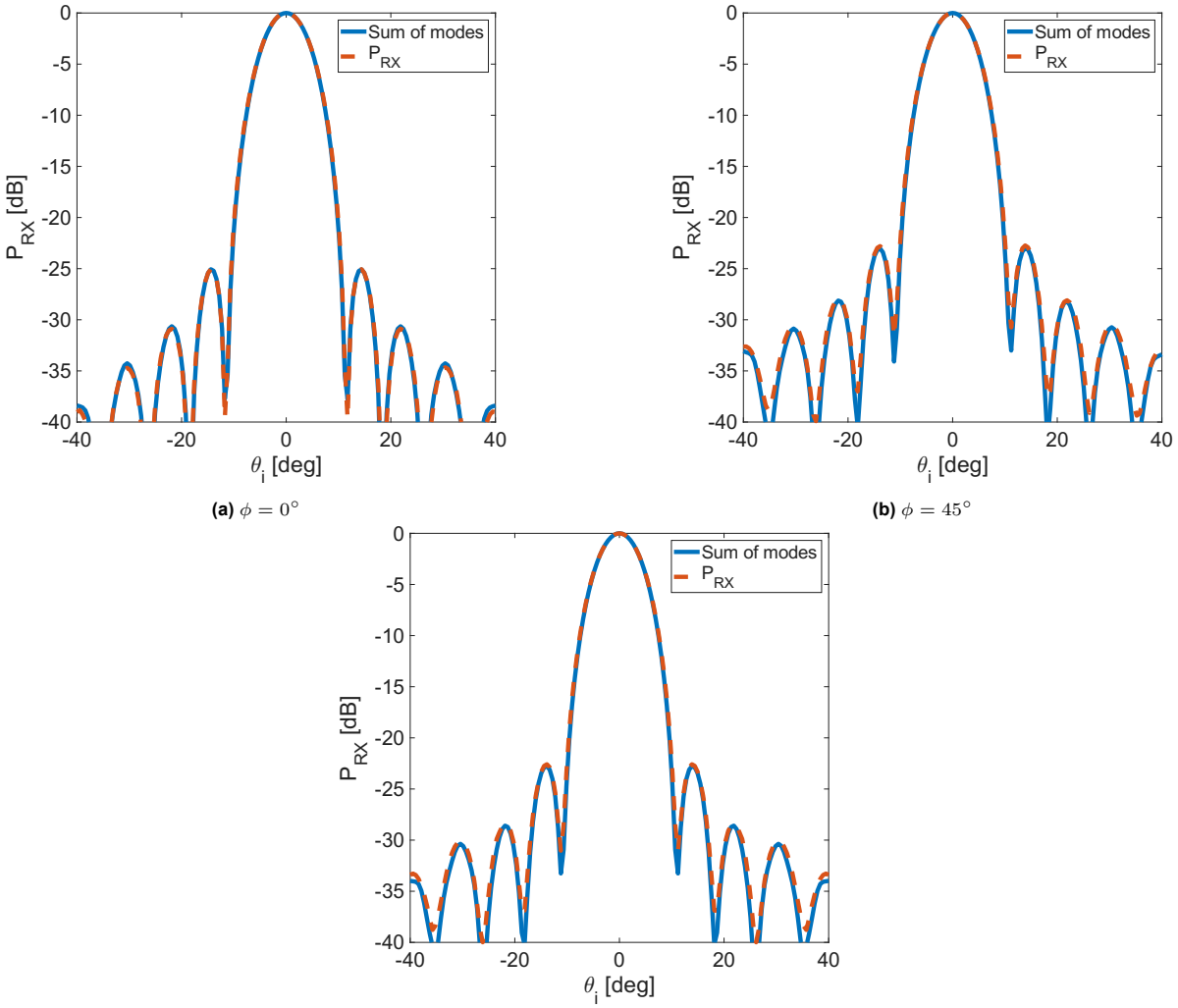

(a) $\phi = 0°$

(b) $\phi = 45°$

(c) $\phi = 90°$

Fig. 5.4: A comparison between a reconstruction of the patterns in reception using the extracted patterns of each of the spatial modes (blue), and the actual patterns in reception (orange) for three different ϕ-cuts: (a) $\phi = 0°$, (b) $\phi = 45°$, and (c) $\phi = 90°$

The patterns shown are almost exactly the same as the patterns in reception of the device itself. There are some minor differences, especially for larger scanning angles. These discrepancies are attributed to the numerical accuracy of the EAI method due to its finite number of simulations. In particular, as

discussed earlier in this chapter, the EAI method is very sensitive to the amount of data provided to extract the modal description. The decomposition might have introduced certain artifacts and losses of data, simply by not being fed with enough samples for an accurate decomposition. Another contributor could be due to single ϕ-cut extraction of the DRF. The complete DRF should be extracted for the full aperture of the device, and the patterns and sensitivities of each of the spatial modes could be missing a dimension worth of information on the coupling to spatial correlations to the incoming field. Since the device discussed here is mostly single moded with a single polarisation, the effect of missing a dimension of data will be small, however, this effect might be larger for higher-moded devices responsive to more than one polarisation.

Although there are slight deviations, these deviations are very small, and therefore it can be concluded that, the EAI tool developed is capable of accurately extracting a modal description of devices under test.

5.4. Investigating the Modal Description of Lens-Absorbers

One of the main goals of using EAI is to study the modal description of multi-mode detectors, such as the absorbers designed in this thesis, and study the effect of various design parameters of these detectors on the modal description. As an initial study, this section will focus on the analysis of one of the absorbers designed in Ch. 2, the absorber design with a line width of $0.6\mu\mathrm{m}$ and a thickness of $21\mathrm{nm}$. This leads to the setup shown in Fig. 5.5.

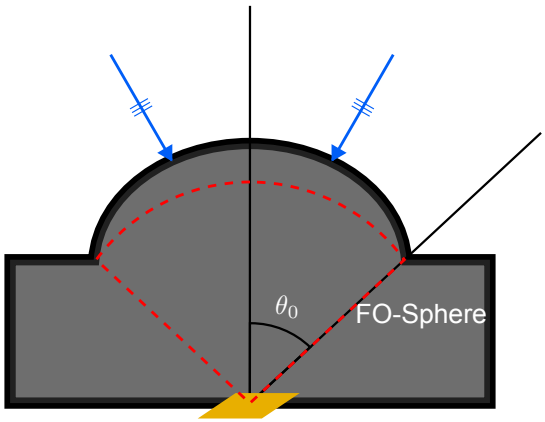

Fig. 5.5: An illustration of performing EAI on the lens-absorber. The power received by the absorber by the two incoming plane waves (indicated by the two arrows) is calculated by applying the method discussed in Ch. 2.

As a baseline, the modal description of this absorber was evaluated for the complete detector designed in Ch. 2: the absorber has a side-length of $2\lambda_d f_{\#}$, and is coupled to a lens with a diameter of $1.4mm$ and an f-number of 2. The result of this investigation can be observed in Fig. 5.6.

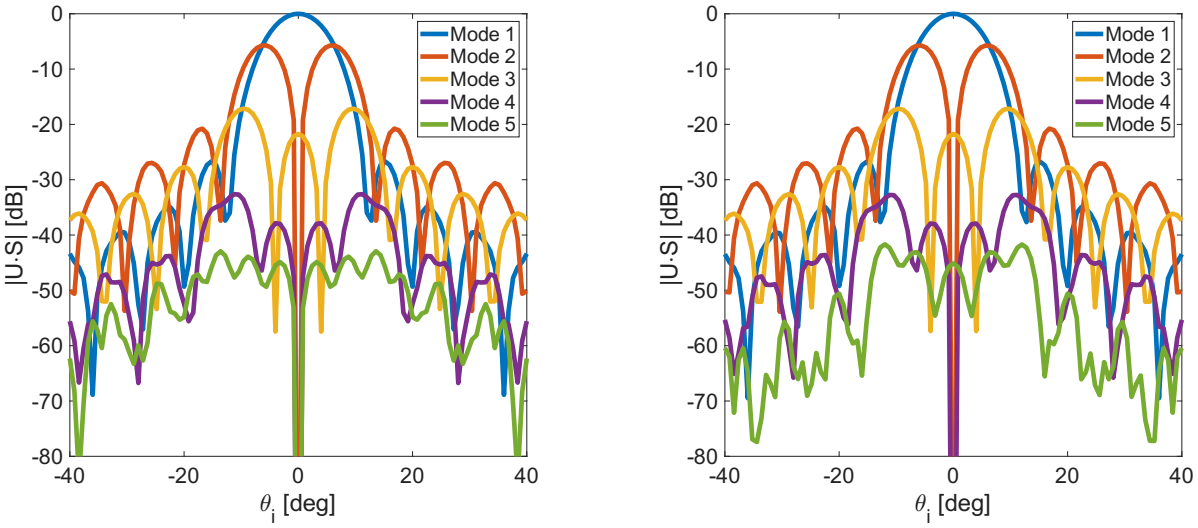

(a) $\phi = 0°$ **(b)** $\phi = 90°$

Fig. 5.6: The modal description for the first 5 spatial modes, for two ϕ-cuts: (a) $\phi = 0°$, (b) $\phi = 90°$, extracted for the lens-absorber designed in Sec. 2.4

Comparing the results shown above to the Gaussian fed lens in Sec. 5.3, there is a distinct difference between a few-moded device and a higher-moded device such as an absorber: the higher order spatial modes shown in Fig. 5.6 are more prominent with respect to the first order spatial mode. As discussed in Ch. 2, lens-absorbers have wider patterns in reception when comparing them to the patterns in reception of lens-antennas. Wider patterns mean that the detector couples more to fields coming in from off-broadside incidence. The effect of this can be seen in Fig. 5.6 by the higher sensitivity to the higher-order spatial modes, which in turn appear to widen the pattern by adding onto the first spatial mode. The sensitivity to the higher-order modes are especially visible when studying Fig. 5.7, where the sensitivity drops off slower compared to Fig. 5.2.

The difference between the two cases ($\phi = 0°$ and $\phi = 90°$) appears to be small, therefore, for the remainder of this chapter, the results discussed will focus on only the $\phi = 0°$-cut.

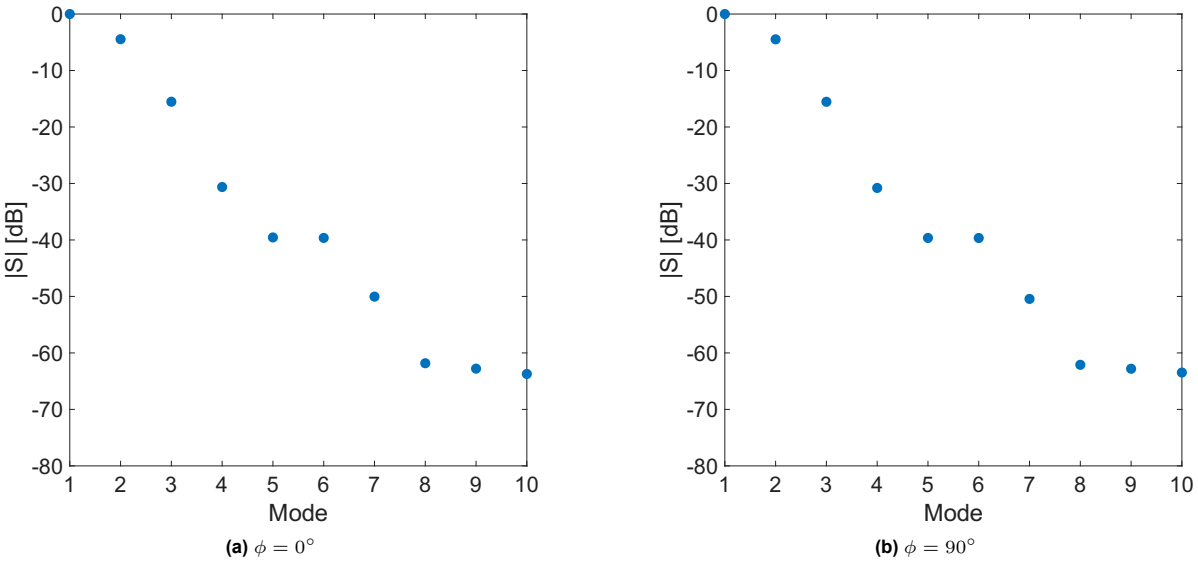

(a) $\phi = 0°$ **(b)** $\phi = 90°$

Fig. 5.7: The sensitivities of the lens-absorber designed in Sec. 2.4 to the first 10 spatial modes, normalised to the sensitivity of the device to the first spatial mode, for two different ϕ-cuts: (a) $\phi = 0°$, (b) $\phi = 90°$

5.4.1. Effect of Absorber Width on the Modal Description

As discussed in Ch. 2, the patterns in reception of lens-absorbers are wider when the side-length of the absorbers is increased. This widening leads to a higher sensitivity to fields coming from directions not located at the broadside of the device. This higher sensitivity to off-broadside incidence can be explained by a higher sensitivity to higher order spatial modes, by comparing the modal description shown in Fig. 5.6 and Fig. 5.7 with the modal descriptions presented in Sec. 5.3.1. To determine how the sensitivity to higher order modes relates to the size of the absorber, the size of the absorber was changed in the EAI simulations, while keeping all other parameters fixed. Next, the total number of spatial modes with a sensitivity higher than 10% of the fundamental spatial mode was used as a figure of merit to describe the number of modes for each absorber size.

The first case of interest is an absorber with an infinitesimal size. As discussed in Ch. 2, the smaller an absorber, the closer the pattern in reception will resemble an airy pattern. To investigate this case, the modal description of an absorber with a size of $0.001\lambda_d f_\#$ was derived using the EAI tool, and is shown in Fig. 5.8.

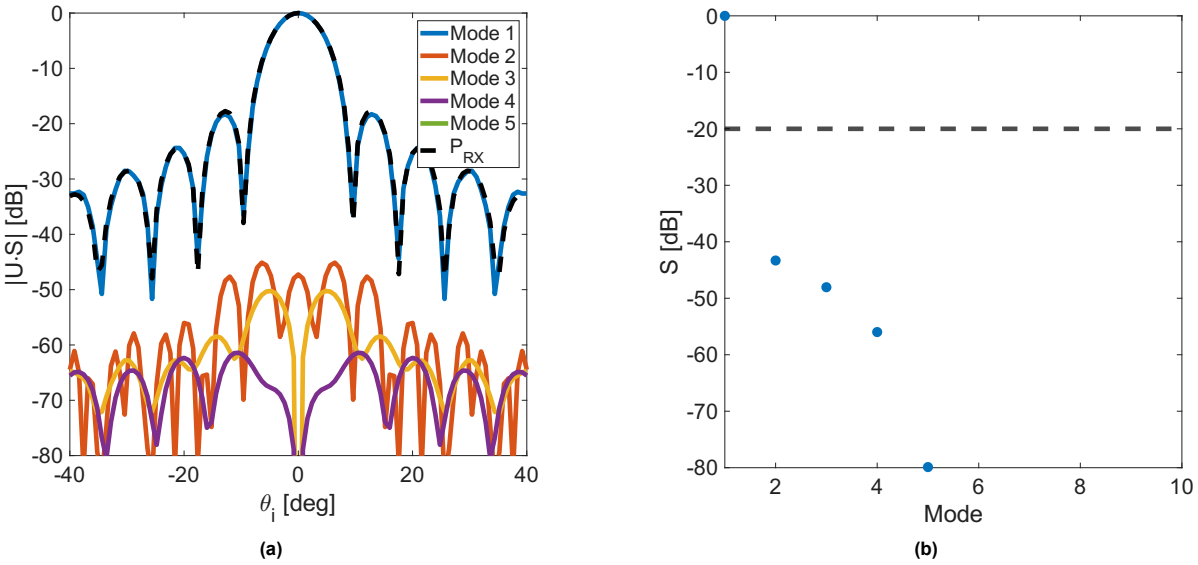

Fig. 5.8: The modal description derives for the lens-absorber designed in Sec. 2.4 with a width of $w = 0.001\lambda_d f_\#$. (a) The patterns in reception for the first five spatial modes. The full pattern in reception has been plotted for reference in black, normalised to the maximum value. (b) The sensitivities of the first 10 spatial modes, normalised to the fundamental spatial mode. Indicating the threshold of 10% in black, used to count the number of modes in the device.

The decomposition shown in Fig. 5.8a displays a far more single moded device, as visible in Fig. 5.8b the difference between the fundamental mode and the first higher order mode is more than -40dB. Due to this, the pattern in reception is dominated by the fundamental mode, leading to a pattern that resembles an airy pattern. Therefore, this confirms the hypothesis that an absorber of infinitesimal size is less sensitive to off-broadside incidence, and is therefore less sensitive to higher order spatial modes.

The opposite is also true: once the size of the absorber is increased, the width of the pattern in reception increases and therefore the device is more sensitive to off-broadside incidence. According to the just confirmed relation between the width of the pattern in reception and the sensitivity to higher order spatial modes, this should lead to a modal description with far more prominent higher order spatial modes. To confirm this, an absorber with size $5\lambda_d f_\#$ was modelled using the EAI tool, of which the result is shown in Fig. 5.9.

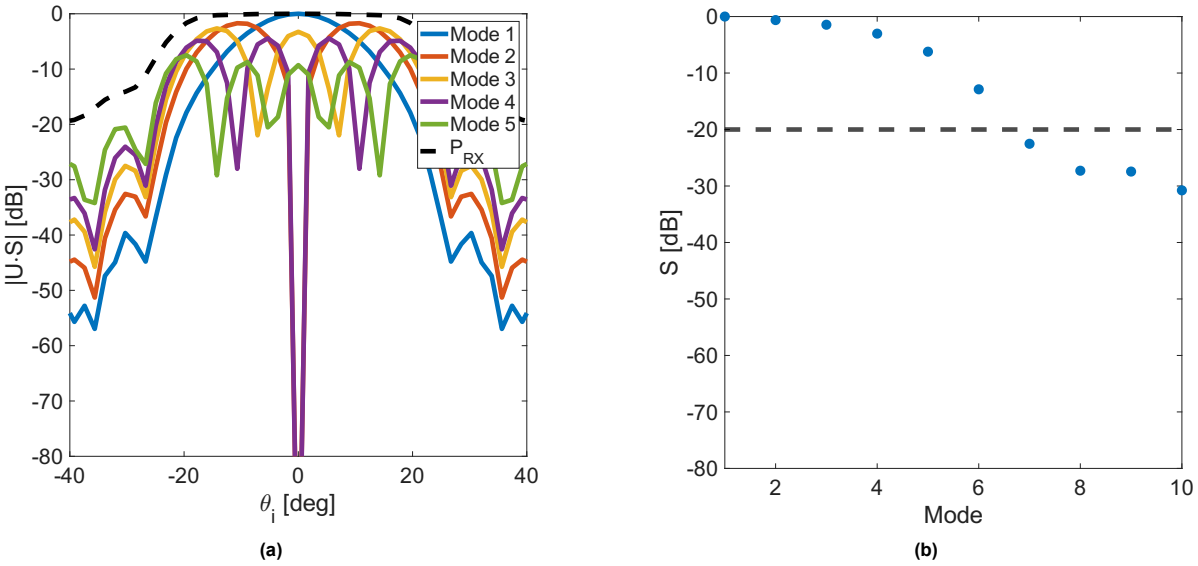

Fig. 5.9: The modal description derives for the lens-absorber designed in Sec. 2.4 with a width of $w = 5\lambda_d f_\#$. (a) The patterns in reception for the first five spatial modes. The full pattern in reception has been plotted for reference in black, normalised to the maximum value. (b) The sensitivities of the first 10 spatial modes, normalised to the fundamental spatial mode. Indicating the threshold of 10% in black, used to count the number of modes in the device.

Due to the device having a very large absorber, the pattern in reception is wide, as shown in Fig. 5.9a. As a result, the higher order patterns in reception are much closer to the fundamental mode, as shown in both Fig. 5.9a and Fig. 5.9b. These higher order modes add a noticeable sensitivity to larger angles of incidence, leading to a widening of the total pattern in reception. Another interesting observation relates to the fundamental mode of the device: the fundamental mode is widening. The reason for this could simply be that the fundamental mode is not necessarily equal for different devices, however, perhaps more likely, the EAI method is struggling to extract accurate modal descriptions for devices with wider main lobes. Further investigations into this behaviour will be performed in future work.

As shown in Fig. 5.9b, the sensitivity for higher order modes drops off far slower compared to the small absorber shown in Fig. 5.8b. A total of 4 higher order modes, with a sensitivity above 10% of the fundamental mode are identified. To demonstrate the relation between larger absorbers and the sensitivity to higher order modes more clearly, Fig. 5.10 shows the number of modes with a sensitivity above 10% versus the width of the absorber. Although the relation between the number of modes and the size is seemingly linear, it should be kept in mind that extracting modal descriptions is more difficult for larger absorbers with a wide pattern in reception. Therefore, results are limited to absorbers up to $w = 10\lambda_d f_\#$.

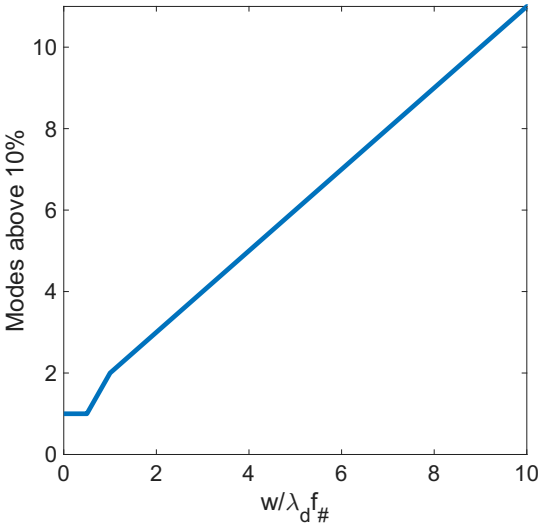

Fig. 5.10: The number of modes with a sensitivity above 10% of the fundamental mode versus the width of the absorber

As discussed in Sec. 5.2.2, an issue with generating an accurate modal description is that at least one extra side-lobe should be visible in the pattern of reception, or the change in amplitude and phase in the DRF is too small for an accurate decomposition. Once the absorber size increases to extremely large sizes, larger than $5\lambda_d f_{\#}$, the patterns become very wide, such that EAI is having difficulty decomposing the DRF into an accurate modal description of the lens-absorber. This is also what happens when investigating the lens-absorber shown in Fig. 5.11. For large lens-absorbers, the patterns in reception seem to be so widened, that the EAI tool decomposes the DRF into patterns that do no longer resemble patterns observed for smaller absorbers.

The reason behind the model breaking down is unclear, it could be related to the amount of data needed to extract a more accurate modal description. However, with these wide patterns in reception, the change in both the amplitude and phase of the DRF is small. Therefore, it is reasonable to assume that the SVD is simply no longer capable of accurately decomposing the data into natural modes in reception.

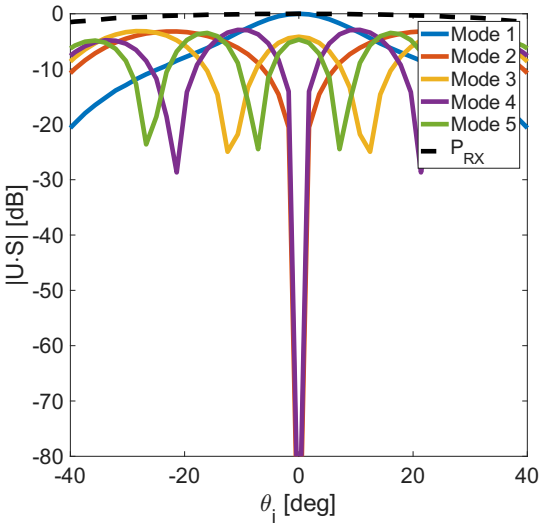

Fig. 5.11: The patterns in reception for the first five spatial modes of the lens-absorber designed in Sec. 2.4 with a width of $w = 10\lambda_d f_{\#}$. The full pattern in reception has been plotted for reference in black, normalised to the maximum value.

5.4.2. Verifying Aperture Size on Modal Description

In case all design parameters for a lens-absorber are fixed, one could state that changing the diameter of the lens, which in turn could increase or decrease the directivity of the lens-absorber, could change the sensitivity to a number of spatial modes. However, the sensitivity to these spatial modes is mostly limited by the device coupled to the lens, which in this case is the absorber. To verify this hypothesis, a set of simulations were performed on the lens-absorber designed in Ch. 2, where all design parameters were fixed, except for the diameter of the lens. When applying the same methodology as used in Sec. 5.4.1, where the number of modes with a sensitivity above 10% are counted, the result as shown in Fig. 5.12 is obtained.

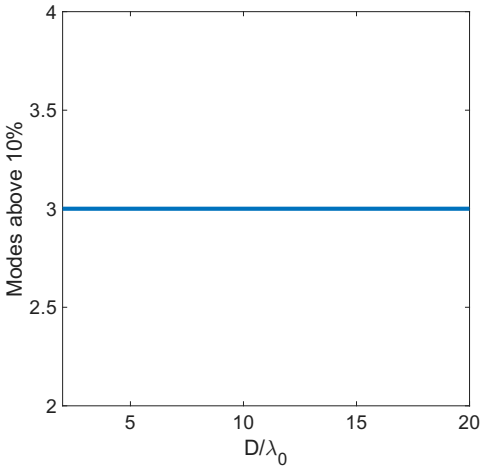

Fig. 5.12: The number of modes with a sensitivity above 10% of the fundamental mode versus the diameter of the lens

Although the result shown above confirms the hypothesis that the sensitivity to spatial modes is not affected by a change in lens diameter, as the modal description is dominated by the absorber side-length, the change in directivity will impact the patterns of the modal description. First of all, due to the changing shape of the detector pattern, the shape of the modes will become more directive as well. An example of this can be seen in Fig. 5.13, where the modal description of a lens-absorber with a diameter of $D_{lens} = 7\lambda_0$ is compared to the modal description of a lens-absorber with $D_{lens} = 15\lambda_0$. In this figure, the directivity of the different modes increases, while the sensitivity to the modes stays the same.

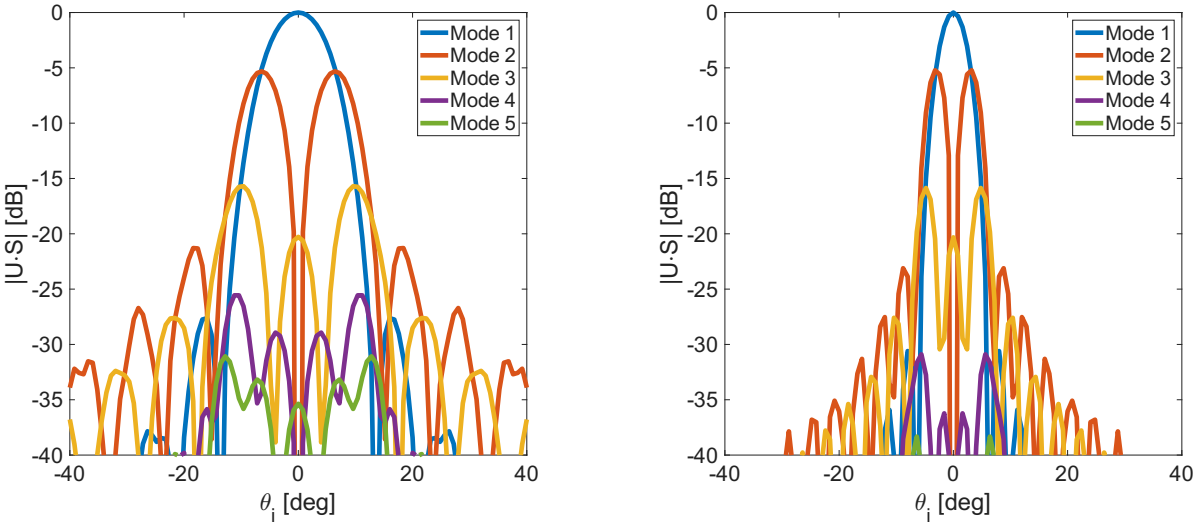

(a) Lens-absorber with $D_{lens} = 7\lambda_0$

(b) Lens-absorber with $D_{lens} = 15\lambda_0$

Fig. 5.13: The modal description for two lenses with different diameter: (a) $D_{lens} = 7\lambda_0$ and (b) $D_{lens} = 15\lambda_0$

An important side-effect that should be pointed out is that due to the increase in directivity, the number of side-lobes in the patterns increases. Due to this, the resolution of the pattern in reception and the patterns of the modal description decreases as the number of samples taken to derive the DRF remains the same. The lower resolution can reduce the accuracy of the extracted modal description, thus the directivity should be taken into account when determining the number of samples needed, or a lens with a smaller diameter should be used for the EAI method to increase the accuracy.

6

Conclusion

The FIR frequency range offers valuable insights into the formation of planets, galaxies, and the universe as we know it. To effectively study this range, detectors with stringent requirements on the sensitivity are needed, with a Noise Equivalent Power on the order of $10^{-20}\mathrm{W}/\sqrt{\mathrm{Hz}}$. In previous works, such detectors, specifically lens-absorber coupled MKIDs, have been designed to operate at 6.98 THz and 12 THz for the POEMM high-altitude balloon mission and the PRIMA space-probe mission. Since these missions require detection down to 1.5 THz and absorber MKIDs at the lower frequency band offer unique challenges, this thesis focused on the development of lens-absorber coupled MKIDs at 1.5 THz. Additionally, the coupling of these detectors to an advanced dispersive element is studied: the VIPA, and techniques have been presented to optimise the performance and coupling to this Quasi-Optical device. Finally, an initial investigation is performed on the multi-moded nature of the lens-absorbers, in an attempt to establish a baseline for future measurements and the possibility to optimise the pattern of these detectors with a novel approach.

6.1. Lens-Absorber Coupled MKIDs for 1.5 THz

Lens-absorber coupled MKID designs were presented in Ch. 2 to operate at 1.5 THz, a key frequency for the discussed missions. High-resistivity silicon was chosen for the lens material due to its low loss at THz frequencies, while Aluminium was selected for the absorber to achieve the necessary NEP across a wide range of loading conditions. More traditional absorber designs, such as the patch absorber or strip absorber, are unsuitable at these frequencies, due to the major impedance mismatch between silicon and the sheet resistance of Aluminium. Instead, meandering-line absorbers were designed, which offer more flexibility in tuning the input impedance for efficient absorption. To maximise the absorption efficiency of the absorbers, a quarter-wavelength backing reflector was introduced to capture the power that would have transmitted through the absorber.

A design strategy was presented to fine-tune the absorption efficiency of absorbers, which was used to design four different absorber geometries. These designs vary in Aluminium thickness (21 nm and 28 nm) and in line width (0.6 $\mu\mathrm{m}$ and 1.3 $\mu\mathrm{m}$) to investigate the impact of fabrication constraints. All designs achieved high absorption efficiency at 1.5 THz ($\eta_{abs,\mathrm{avg}} > 0.95$), with the thinner 21 nm designs offering broader bandwidths ($\mathrm{BW}_{\text{-1dB}} = 1.38$ THz and 1.12 THz for 0.6 $\mu\mathrm{m}$ and 1.3 $\mu\mathrm{m}$ line widths, respectively). Although the designs with thinner Aluminium provide a large bandwidth for TeraHertz frequencies, the larger inductance of these designs also limits the range of possible resonance frequencies of the MKIDs. The lower resonance frequencies can be an advantage, as lower frequency readouts are cheaper and consume less power, however, in some cases higher readout frequencies are needed for practical cases. This was the case in this work, since SRON's systems operate in a 2-4 GHz band.

The lens geometry was optimised using a GOFO model for the lens in combination with a Floquet Wave based model, which was validated against commercial EM solvers. An elliptical lens was chosen for its ability to focus incoming rays at a single focal point. The lens diameter was chosen with the measurement equipment in mind ($D_{lens} = 1.4\mathrm{mm}$), and its f-number was selected to ensure that the

angular region seen by the absorber is below the critical angle of the Silicon-air interface ($f_{\#} = 2$). To reduce reflection on the surface of the lens, a frusta matching layer was added which is capable of providing matching over a large bandwidth (above 3:1), and is compatible with the low operating temperatures in the cryostat.

Since there is a trade-off between the aperture efficiency and focusing efficiency of lens-absorbers, when selecting the side-length of the absorber, a side-length of $w = 2\lambda_d f_{\#}$ was chosen which provides a high aperture efficiency of $\eta_{ap,x} = 0.83$ and $\eta_{ap,y} = 0.78$ for x- and y-polarised plane waves, respectively, while still maintaining acceptable focus quality.

Currently, 3 different chip design are being fabricated to (1) test the radiation coupling and the NEP of the lens-absorbers with and without the matching layer and backshort, (2) perform multi-moded pattern measurements of the lens-absorbers, and (3) test the scalability of the absorber coupled MKIDs for larger arrays. Moreover, 2 lens designs are being fabricated: one with and one without a matching layer.

6.2. Optimisation Techniques for Coupling to Optical Systems of Future FIR Missions

For the discussed FIR missions, the Virtually Imaged Phased Array (VIPA) serves as a dispersive element, capable of separating radiation with a large angular-dispersion versus wavelength. While VIPA offers high angular dispersion, it also introduces various non-idealities such as aberrations in the transmitted fields, and part of the radiation is transmitted to higher-order modes, which can significantly reduce the efficiency of the instrument.

Although the effect of the higher-order modes cannot be directly mitigated by the detectors, two optimisation techniques have been presented in Ch. 4 to mitigate various phase aberrations: a lateral displacement of the absorber along the focal plane to correct for linear phase errors, and a lens-shaping technique to correct for more complex phase aberrations. The techniques have been applied to both a central and an edge element of the spatial array. Without optimisation, the aperture efficiencies were already high: $\eta_{ap,\text{center}} = 0.819$ and $\eta_{ap,\text{edge}} = 0.790$ for the center and edge cases, respectively. However, applying the techniques still showed potential: after applying lateral displacement, the edge case was increased to $\eta_{ap,\text{edge}} = 0.820$, and further lens-shaping improved the efficiency to $\eta_{ap,\text{edge}} = 0.862$.

The importance of these optimisations is particularly evident in the edge case, where higher-order modes contain close to 50% of the radiated power, resulting in an effective aperture efficiency that is reduced by 50%. In addition to this, the model used to generate the fields shown in this thesis was relatively ideal. Once a more realistic model or data of an actual VIPA is available, the proposed optimisation steps discussed in this thesis should be applied. Additionally, the optimisation techniques discussed here could be employed as degrees of freedom to relax requirements on the VIPA's output field in favour of reduced power contained in its higher order modes. This approach could lead to an improvement of overall coupling after applying the presented optimisation techniques.

6.3. Analysing the Modal Description of Multi-Mode Detectors

In Ch. 5, an initial investigation into the Energy Absorption Interferometry (EAI) method was performed by designing a modelling tool capable of applying EAI to various detectors. The EAI technique is an experimental technique that can be used to extract the modal description of detectors, which is of interest for multi-mode detectors such as lens-absorbers. By understanding the distribution of power between different natural modes and the patterns of these modes, the EAI method could offer insights into the performance and optimisation of multi-mode detectors.

The EAI tool was validated for a Gaussian fed lens-antenna, which is a single-mode device. The modal description was successfully extracted for 3 different azimuth cuts of farfield patterns, which all resembled the modal description of a few-moded device. The pattern in reception of the lens-antenna was also recovered from these modal descriptions, proving the working principle of the EAI modelling tool.

The EAI tool was also applied on one of the lens-absorber designs from Ch. 2, revealing a modal

description with higher sensitivities to higher-order modes. Each of these modes contributes to the widening of the patterns in reception of the lens-absorbers, due to the increased off-broadside sensitivity of the higher-order modes. To study how a lower focusing efficiency for larger absorber relates to the modal description of the lens-absorber, the modal description was extracted for absorbers with various side lengths. This experiment confirmed that small absorbers approach single-moded devices, and that larger absorbers become more sensitive to higher order natural modes. Analysis also confirmed that the diameter of the lens has minimal impact on the modal description of the lens-absorbers, as the sensitivity to higher order modes remained the same for larger lenses, while the directivity of the patterns of the modal description increased.

The EAI technique shows potential to optimise the pattern of multi-mode detectors by considering their modal description.

6.4. Future Work

This thesis contributes to the field of FIR detection by developing and analysing lens-absorber coupled MKIDs. In addition to this, the thesis highlights challenges in instrument and detector design, such as coupling to complex (Quasi-)Optical devices, and introduces optimisation techniques that could be applied in future research.

6.4.1. Lens-Absorber Coupled MKIDs

Currently, the designed lens-absorber coupled MKIDs are being fabricated. Once finished, their performance (aperture efficiency, focusing efficiency, NEP) will be experimentally determined. One final design should be selected for the future FIR missions and, together with the previously designed 6.98 THz and 12 THz lens-absorbers, should be integrated into an actual instrument. The previously designed 6.98 THz and 12 THz lens-absorbers could also be improved by applying techniques discussed in this thesis. Currently, these absorbers are designed without a backing reflector, which reduces the absorption efficiency of these devices. Using the software developed in this thesis to design the detectors and to generate the mask files, any detector can be re-designed and fabricated fast and efficiently.

6.4.2. Mid-Infrared Lens-Absorbers

The design procedure for lens-absorbers discussed in this thesis can also be applied for Mid-Infrared (MIR) missions. Currently, the detectors used at these wavelengths are not optimised for MIR detection [43], reducing the overall efficiency of these devices.

6.4.3. VIPA Optimisation

Future work should focus on the optimisation techniques presented in this thesis once a more realistic model of the VIPA is available, or once experimental data of the VIPA's output is obtained. Furthermore, investigating the potential to degrade the quality of the transmitted fields of the VIPA to reduce the higher-order modes radiated by the VIPA would be a compelling case study.

6.4.4. EAI

The experimental EAI technique could be applied to one of the fabricated lens-absorbers, and the resulting modal description could be compared with the simulated model presented in this thesis. Additionally, the possibility to use a modal description to optimise the performance of lens-absorbers could be studied further. Finally, since EAI is only applied to single azimuthal cuts, methods could be researched that could aid in dealing with large, high-dimensional datasets, such that the modal description can be extracted for the complete aperture of a device.

References

[1] D. Farrah, K. E. Smith, D. Ardila, *et al.*, "Review: Far-infrared instrumentation and technological development for the next decade," en, *J. Astron. Telesc. Instrum. Syst.*, vol. 5, no. 02, p. 1, Apr. 2019, ISSN: 2329-4124. DOI: 10.1117/1.JATIS.5.2.020901. [Online]. Available: https://www.spiedigitallibrary.org/journals/Journal-of-Astronomical-Telescopes-Instruments-and-Systems/volume-5/issue-02/020901/Review--far-infrared-instrumentation-and-technological-development-for-the/10.1117/1.JATIS.5.2.020901.full.

[2] J. J. A. Baselmans, F. Facchin, A. Pascual Laguna, *et al.*, "Ultra-sensitive THz microwave kinetic inductance detectors for future space telescopes," en, *Astronomy & Astrophysics*, vol. 665, 2022, ISSN: 0004-6361. DOI: 10.1051/0004-6361/202243840. [Online]. Available: https://repository.tudelft.nl/islandora/object/uuid%3A9d071ef6-cb32-498c-986a-b96031891b4a.

[3] P. K. Day, N. F. Cothard, C. Albert, *et al.*, *A 25-micron single photon sensitive kinetic inductance detector*, en, May 2024. [Online]. Available: http://arxiv.org/abs/2404.10246.

[4] J. J. A. Baselmans, J. Bueno, S. J. C. Yates, *et al.*, "A kilo-pixel imaging system for future space based far-infrared observatories using microwave kinetic inductance detectors," en, *A&A*, vol. 601, A89, May 2017, ISSN: 0004-6361, 1432-0746. DOI: 10.1051/0004-6361/201629653. [Online]. Available: http://www.aanda.org/10.1051/0004-6361/201629653.

[5] *POEMM - a NASA stratospheric balloon mission with TU Delft/SRON detectors*, Jul. 2024. [Online]. Available: https://terahertz.tudelft.nl/News/indexitem.php?mi=652.

[6] G. J. Stacey, *The planetary origins and evolution multispectral monochrometer (POEMM) | SPIE Astronomical Telescopes + Instrumentation*, Jun. 2024. [Online]. Available: https://spie-org.tudelft.idm.oclc.org/astronomical-telescopes-instrumentation/presentation/The-planetary-origins-and-evolution-multispectral-monochrometer-POEMM/13102-192#_=_.

[7] A. Moullet, T. Kataria, D. Lis, *et al.*, *PRIMA General Observer Science Book*, arXiv:2310.20572 [astro-ph], Oct. 2023. DOI: 10.48550/arXiv.2310.20572. [Online]. Available: http://arxiv.org/abs/2310.20572.

[8] F. E. Office and F. Ltd, "Virtually Imaged Phased Array," en, *FUJITSU Sci. Tech. J.*, 1999.

[9] S. O. Dabironezare, S. v. Berkel, P. M. Echternach, P. K. Day, C. M. Bradford, and J. J. Baselmans, "Lens Absorber Coupled MKIDs for Far Infrared Imaging Spectroscopy," in *2023 48th International Conference on Infrared, Millimeter, and Terahertz Waves (IRMMW-THz)*, ISSN: 2162-2035, Sep. 2023, pp. 1–2. DOI: 10.1109/IRMMW-THz57677.2023.10299178. [Online]. Available: https://ieeexplore-ieee-org.tudelft.idm.oclc.org/document/10299178.

[10] C. Molero, M. García-Vigueras, R. Rodríguez-Berral, F. Mesa, and N. Llombart, "Equivalent Circuit Approach for Practical Applications of Meander-Line Gratings," *IEEE Antennas and Wireless Propagation Letters*, vol. 16, pp. 3088–3091, 2017, Conference Name: IEEE Antennas and Wireless Propagation Letters, ISSN: 1548-5757. DOI: 10.1109/LAWP.2017.2756438. [Online]. Available: https://ieeexplore-ieee-org.tudelft.idm.oclc.org/document/8055514.

[11] B. Blázquez, N. Llombart, D. Cavallo, A. Freni, and A. Neto, "A Rigorous Equivalent Network for Linearly Polarized THz Absorbers," *IEEE Transactions on Antennas and Propagation*, vol. 62, no. 10, pp. 5077–5088, Oct. 2014, Conference Name: IEEE Transactions on Antennas and Propagation, ISSN: 1558-2221. DOI: 10.1109/TAP.2014.2341292. [Online]. Available: https://ieeexplore-ieee-org.tudelft.idm.oclc.org/document/6861440.

[12] N. Llombart, S. O. Dabironezare, G. Carluccio, A. Freni, and A. Neto, "Reception Power Pattern of Distributed Absorbers in Focal Plane Arrays: A Fourier Optics Analysis," en, *IEEE Trans. Antennas Propagat.*, vol. 66, no. 11, pp. 5990–6002, Nov. 2018, ISSN: 0018-926X, 1558-2221. DOI: 10.1109/TAP.2018.2862359. [Online]. Available: https://ieeexplore.ieee.org/document/8424188/.

[13] S. O. Dabironezare, “Fourier Optics Field Representations for the Design of Wide Field-of-View Imagers at Sub-millimetre Wavelengths,” en, 2020. DOI: 10.4233/uuid:23c845e1-9546-4e86-ae77-e0f14272517b. [Online]. Available: https://repository.tudelft.nl/islandora/object/uuid%3A23c845e1-9546-4e86-ae77-e0f14272517b.

[14] H. Zhang, “A GO/FO Tool for Analyzing Quasi-optical Systems in Reception,” en, 2018. [Online]. Available: https://repository.tudelft.nl/islandora/object/uuid%3A997558e6-7f32-493a-9f84-57895636db28.

[15] A. Nagamune and P. Pathak, “An efficient plane wave spectral analysis to predict the focal region fields of parabolic reflector antennas for small and wide angle scanning,” en, *IEEE Trans. Antennas Propagat.*, vol. 38, no. 11, pp. 1746–1756, Nov. 1990, ISSN: 0018926X. DOI: 10.1109/8.102735. [Online]. Available: http://ieeexplore.ieee.org/document/102735/.

[16] C. A. Balanis, *Advanced engineering electromagnetics*. New York: Wiley, 1989, ISBN: 978-0-471-62194-2.

[17] W. S. Holland, D. Bintley, E. L. Chapin, *et al.*, “SCUBA-2: The 10 000 pixel bolometer camera on the James Clerk Maxwell Telescope,” en, *Monthly Notices of the Royal Astronomical Society*, vol. 430, no. 4, pp. 2513–2533, Apr. 2013, ISSN: 1365-2966, 0035-8711. DOI: 10.1093/mnras/sts612. [Online]. Available: http://academic.oup.com/mnras/article/430/4/2513/1090786/SCUBA2-the-10-000-pixel-bolometer-camera-on-the.

[18] B. Pu, K. Kim, S. Kim, and W. Nah, “Modeling and Parameter Extraction of Coplanar Symmetrical Meander Lines,” *IEEE Transactions on Electromagnetic Compatibility*, vol. 57, pp. 1–9, Jun. 2015. DOI: 10.1109/TEMC.2014.2383383.

[19] *CST Studio Suite*, en, Jul. 2023. [Online]. Available: https://www.3ds.com/products/simulia/cst-studio-suite.

[20] D. Rutledge and S. Schwarz, “Planar multimode detector arrays for infrared and millimeter-wave applications,” *IEEE Journal of Quantum Electronics*, vol. 17, no. 3, pp. 407–414, Mar. 1981, Conference Name: IEEE Journal of Quantum Electronics, ISSN: 1558-1713. DOI: 10.1109/JQE.1981.1071097. [Online]. Available: https://ieeexplore-ieee-org.tudelft.idm.oclc.org/document/1071097.

[21] M. ji, C. Musante, S. Yngvesson, A. Gatesman, and J. Waldman, “Study of Parylene as Antireflection Coating for Silicon Optics at THz Frequencies,” May 2000.

[22] N. T. Nguyen, R. Sauleau, and C. J. Martinez Perez, “Very Broadband Extended Hemispherical Lenses: Role of Matching Layers for Bandwidth Enlargement,” *IEEE Transactions on Antennas and Propagation*, vol. 57, no. 7, pp. 1907–1913, Jul. 2009, Conference Name: IEEE Transactions on Antennas and Propagation, ISSN: 1558-2221. DOI: 10.1109/TAP.2009.2021884. [Online]. Available: https://ieeexplore-ieee-org.tudelft.idm.oclc.org/document/4907040.

[23] H. Y. Yao, Z. Y. Chen, and T. H. Chang, “Broadband multilayer antireflection coating in THz region,” in *2015 40th International Conference on Infrared, Millimeter, and Terahertz waves (IRMMW-THz)*, ISSN: 2162-2035, Aug. 2015, pp. 1–2. DOI: 10.1109/IRMMW-THz.2015.7327632. [Online]. Available: https://ieeexplore-ieee-org.tudelft.idm.oclc.org/abstract/document/7327632.

[24] J. Bueno, S. Bosma, T. Buskamp-Alda, M. Alonso-delPino, and N. Llombart, “Broadband Lossless Matching Layer for Lens Arrays at THz Frequencies,” en, in *2022 47th International Conference on Infrared, Millimeter and Terahertz Waves (IRMMW-THz)*, Delft, Netherlands: IEEE, Aug. 2022, pp. 1–2, ISBN: 978-1-72819-427-1. DOI: 10.1109/IRMMW-THz50927.2022.9895659. [Online]. Available: https://ieeexplore.ieee.org/document/9895659/.

[25] J. Bueno, S. Bosma, T. Buskamp-Alda, M. Alonso-delPino, and N. Llombart, “Lossless Matching Layer for Silicon Lens Arrays at 500 GHz Using Laser Ablated Structures,” en, *IEEE Trans. THz Sci. Technol.*, vol. 12, no. 6, pp. 667–672, Nov. 2022, ISSN: 2156-342X, 2156-3446. DOI: 10.1109/TTHZ.2022.3202031. [Online]. Available: https://ieeexplore.ieee.org/document/9868802/.

[26] S. Hailey-Dunsheath, R. M. J. Janssen, J. Glenn, *et al.*, "Kinetic inductance detectors for the Origins Space Telescope," *JATIS*, vol. 7, no. 1, p. 011 015, Mar. 2021, Publisher: SPIE, ISSN: 2329-4124, 2329-4221. DOI: 10.1117/1.JATIS.7.1.011015. [Online]. Available: https://www-spiedigitallibrary-org.tudelft.idm.oclc.org/journals/Journal-of-Astronomical-Telescopes-Instruments-and-Systems/volume-7/issue-1/011015/Kinetic-inductance-detectors-for-the-Origins-Space-Telescope/10.1117/1.JATIS.7.1.011015.full.

[27] P. J. de Visser, "Quasiparticle dynamics in aluminium superconducting microwave resonators | TU Delft Repository," Ph.D. dissertation, TU Delft, Delft, Netherlands, Mar. 2014, ISBN: 978-90-8593-178-2.

[28] J. J. A. Baselmans, private communication, 2024.

[29] *Sonnet Software*. [Online]. Available: https://www.sonnetsoftware.com/.

[30] "Skin EffectNormal and Anomalous," en, in *Transmission Lines and Communication Networks*, IEEE, 2009, ISBN: 978-0-470-54674-1. DOI: 10.1109/9780470546741.ch4. [Online]. Available: https://ieeexplore.ieee.org/document/5263665.

[31] R. Sproull, R. Lyon, and S. Trimberger, *The Caltech Intermediate Form for LSI Layout Description*. Feb. 1980.

[32] I. Veenendaal, D. Naylor, B. Gom, *et al.*, "An angle-scanned cryogenic Fabry–Pérot interferometer for far-infrared astronomy," *Review of Scientific Instruments*, vol. 91, no. 8, p. 083 108, Aug. 2020, ISSN: 0034-6748. DOI: 10.1063/5.0012432. [Online]. Available: https://doi.org/10.1063/5.0012432.

[33] X. Hu, Q. Sun, J. Li, C. Li, Y. Liu, and J. Zhang, "Spectral dispersion modeling of virtually imaged phased array by using angular spectrum of plane waves," EN, *Opt. Express, OE*, vol. 23, no. 1, pp. 1–12, Jan. 2015, Publisher: Optica Publishing Group, ISSN: 1094-4087. DOI: 10.1364/OE.23.000001. [Online]. Available: https://opg.optica.org/oe/abstract.cfm?uri=oe-23-1-1.

[34] W. Jellema, private communication, 2024.

[35] H. Zhang, "Analysis and Design of Lens Antenna Systems for Applications at Millimeter and Submillimeter Wavelengths," en, Ph.D. dissertation, Delft University of Technology, 2024. DOI: 10.4233/UUID:5FB0DFE6-94CC-40F1-8773-91367B5E2FBA. [Online]. Available: http://resolver.tudelft.nl/uuid:5fb0dfe6-94cc-40f1-8773-91367b5e2fba.

[36] A. Mavropoulou, "On the Design of Lens Array Architectures for the TIFUUN Imaging Spectrometer," en, 2023. [Online]. Available: https://repository.tudelft.nl/islandora/object/uuid%3A8ee45f53-2f1a-4300-9e86-b8ba4781c1cc.

[37] S. O. Dabironezare, G. Carluccio, A. Freni, A. Neto, and N. Llombart, "Coherent Fourier Optics Model for the Synthesis of Large Format Lens-Based Focal Plane Arrays," *IEEE Transactions on Antennas and Propagation*, vol. 69, no. 2, pp. 734–746, Feb. 2021, Conference Name: IEEE Transactions on Antennas and Propagation, ISSN: 1558-2221. DOI: 10.1109/TAP.2020.3016501. [Online]. Available: https://ieeexplore-ieee-org.tudelft.idm.oclc.org/document/9171563.

[38] H. Zhang, S. O. Dabironezare, J. J. Baselmans, and N. Llombart, "Focal Plane Array of Shaped Quartz Lenses for Wide Field-of-view Sub-millimeter Imaging Systems," *IEEE Transactions on Antennas and Propagation*, vol. 72, no. 2, pp. 1263–1274, 2023, ISSN: 0018-926X. DOI: 10.1109/TAP.2023.3334391. [Online]. Available: http://www.scopus.com/inward/record.url?scp=85179029577&partnerID=8YFLogxK.

[39] C. N. Thomas and S. Withington, "Experimental Demonstration of an Interferometric Technique for Characterizing the Full Optical Behavior of Multi-Mode Power Detectors," *IEEE Transactions on Terahertz Science and Technology*, vol. 2, no. 1, pp. 50–60, Jan. 2012, Conference Name: IEEE Transactions on Terahertz Science and Technology, ISSN: 2156-3446. DOI: 10.1109/TTHZ.2011.2177693. [Online]. Available: https://ieeexplore.ieee.org/document/6109369.

[40] “Second-order coherence theory of vector electromagnetic fields,” in *Optical Coherence and Quantum Optics*, E. Wolf and L. Mandel, Eds., Cambridge: Cambridge University Press, 1995, pp. 340–374, ISBN: 978-0-521-41711-2. DOI: 10.1017/CBO9781139644105.007. [Online]. Available: https://www.cambridge.org/core/books/optical-coherence-and-quantum-optics/secondorder-coherence-theory-of-vector-electromagnetic-fields/B76D3E96E0333E8FDF0679A72DA834CD.

[41] I. Veenendaal, E. Castillo-Dominguez, S. J. Yates, B. Lap, and W. Jellema, “Applying Energy Absorption Interferometry to THz Direct Detectors Using Photomixers,” *IEEE Transactions on Terahertz Science and Technology*, vol. 13, no. 6, pp. 594–604, Nov. 2023, Conference Name: IEEE Transactions on Terahertz Science and Technology, ISSN: 2156-3446. DOI: 10.1109/TTHZ.2023.3307568. [Online]. Available: https://ieeexplore.ieee.org/document/10227831.

[42] L. R. Tucker, “Some mathematical notes on three-mode factor analysis,” en, *Psychometrika*, vol. 31, no. 3, pp. 279–311, Sep. 1966, ISSN: 1860-0980. DOI: 10.1007/BF02289464. [Online]. Available: https://doi.org/10.1007/BF02289464.

[43] W. Ras, “Microwave Kinetic Inductance Detectors for the Mid-Infrared,” en, 2022.

A

Derivation of S-parameters for an asymmetric absorber

Using periodic array CST simulations, the Z-parameters of the absorbing layer can be obtained. In order to model the performance of the full lens-absorber structure, the S-parameters of the periodic structure in the presence of its stratification is needed.

To find the S-parameters of the absorbing structure, a Floquet-wave transmission line representation of the structure is used, which can be seen in Fig. A.1. The S-parameters are calculated at the top of the absorbing structure. For the remainder of the calculation, the bottom half of the structure, consisting of the transmission lines of length h_{BR} connected to the backing reflector with impedance Z_{BR}, will be represented by a set of impedances: Z_B^{TE} and Z_B^{TM}

$$Z_B^{TE/TM} = Z_0^{TE/TM} \frac{Z_{BR} + jZ_0^{TE/TM} \tan\left(k_0^{TE/TM} h_{BR}\right)}{Z_0^{TE/TM} + jZ_{BR} \tan\left(k_0^{TE/TM} h_{BR}\right)} \tag{A.1}$$

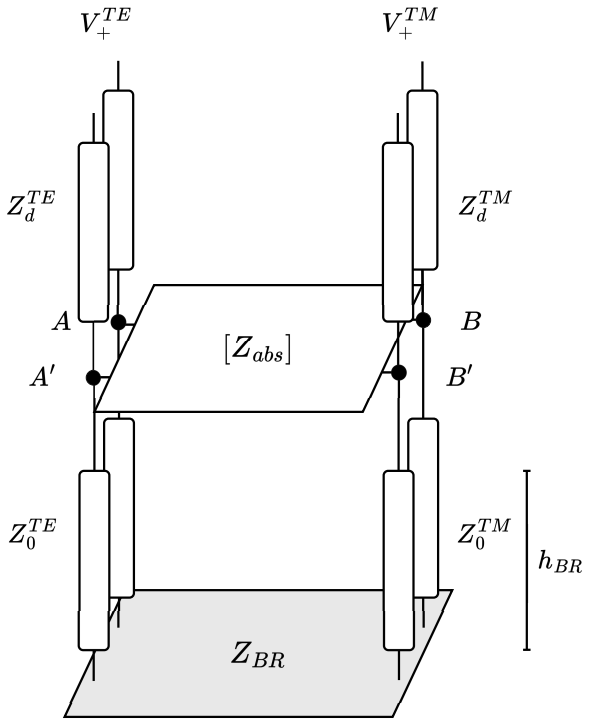

Fig. A.1: The Floquet-wave transmission line model for the absorbing structure. The structure consists of the Z-parameters of the absorbing layer in between interfaces AA' and BB', the transmission lines representing the medium where the incoming fields originate from above, and the backing reflector below. The backing reflector consists of a free-space transmission line of length h_{BR} and a material with impedance Z_{BR}

The Floquet-wave transmission line circuit can be represented using the circuit in Fig. A.2, which can be used to calculate the S-parameters.

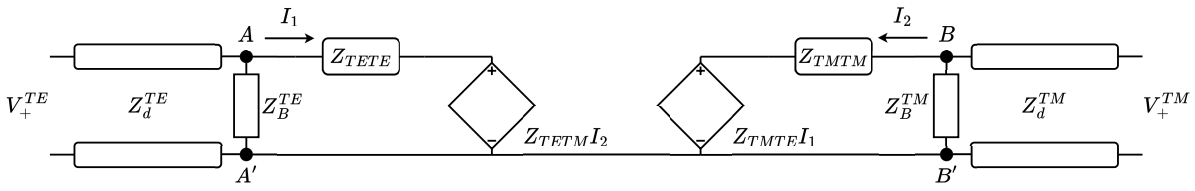

Fig. A.2: The equivalent circuit of Fig. A.1 which will be used to calculate the S-parameters of the absorber structure

A.1. Calculation of S_{TETE}

The reflection back into the TE port, S_{TETE}, can be calculated as:

$$S_{TETE} = \left.\frac{V_-^{TE}}{V_+^{TE}}\right|_{V_+^{TM}=0} \tag{A.2}$$

This equation is simply equal to the reflection coefficient at the AA' interface

$$S_{TETE} = \Gamma|_{AA'} = \frac{Z_{AA'} - Z_d^{TE}}{Z_{AA'} + Z_d^{TE}} \tag{A.3}$$

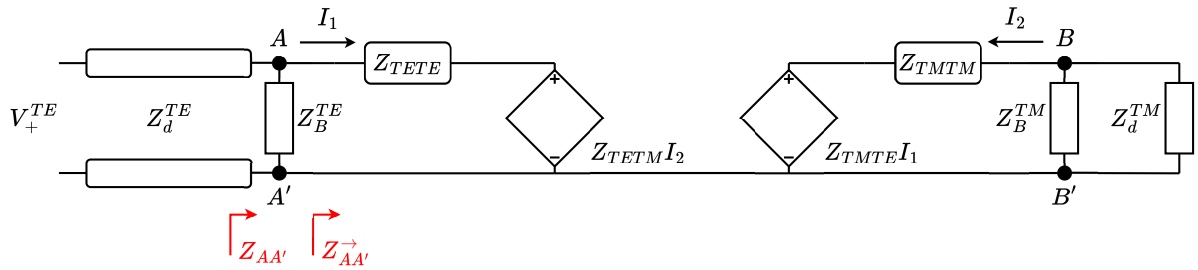

Fig. A.3: Equivalent circuit for finding S_{TETE}, where $V_+^{TM} = 0$

The impedance seen at the AA' can be more easily calculated by describing the impedance as the parallel combination of Z_B^{TE} and $Z_{AA'}^{\rightarrow}$, where $Z_{AA'}^{\rightarrow}$ is shown in Fig. A.3. This leads to the circuit in Fig. A.4.

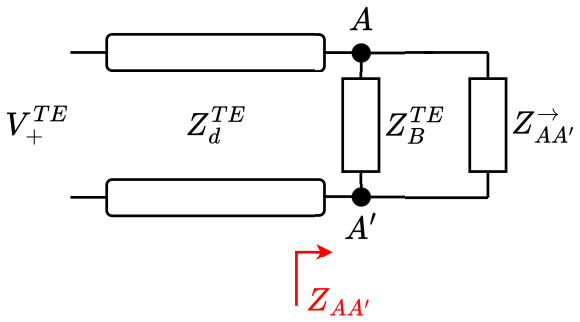

Fig. A.4: Equivalent circuit showing that $Z_{AA'}$ is represented by the parallel connection of two impedances: the backshort impedance Z_B^{TE}, and the equivalent impedance of the circuit to the right of AA', $Z_{AA'}^{\rightarrow}$

To calculate $Z_{AA'}^{\rightarrow}$, a test source of 1 Volt will be introduced, leading to the circuit in Fig. A.5. By finding I_1, $Z_{AA'}^{\rightarrow}$ can be calculated as $Z_{AA'}^{\rightarrow} = \frac{1}{I_1}$. To find I_1, the following system of equations can be set up:

$$-1 + Z_{TETE}I_1 + Z_{TETM}I_2 = 0 \tag{A.4}$$

$$(Z_{TMTM} + Z_B^{TM}||Z_d^{TM})I_2 + Z_{TMTE}I_1 = 0 \tag{A.5}$$

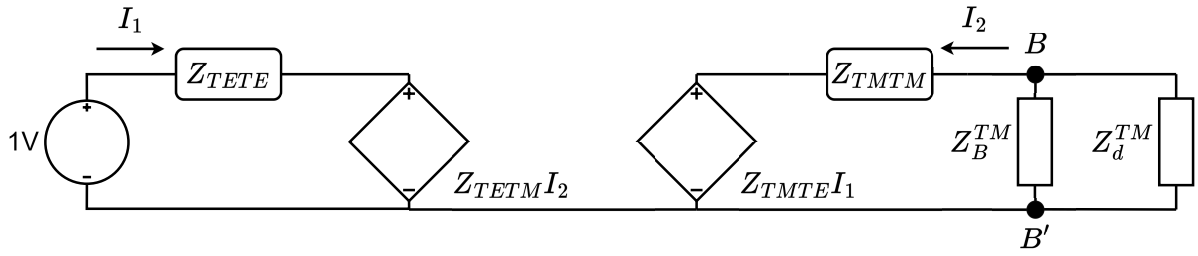

Fig. A.5: Equivalent circuit of $Z_{AA'}^{\rightarrow}$, with a test source of 1V

Solving Eq. A.5 for I_2 leads to:

$$I_2 = -\frac{Z_{TMTE}}{Z_{TMTM} + Z_B^{TM}||Z_d^{TM}} I_1 \tag{A.6}$$

This result can be substituted into Eq. A.4 and solved for I_1

$$\begin{aligned} Z_{TETE} I_1 + Z_{TETM} I_2 &= 1 \\ Z_{TETE} I_1 + -\frac{Z_{TETM} Z_{TMTE}}{Z_{TMTM} + Z_B^{TM}||Z_d^{TM}} I_1 &= 1 \\ \left(Z_{TETE} - \frac{Z_{TETM} Z_{TMTE}}{Z_{TMTM} + Z_B^{TM}||Z_d^{TM}} \right) I_1 &= 1 \\ I_1 = \frac{1}{Z_{TETE} - \frac{Z_{TETM} Z_{TMTE}}{Z_{TMTM} + Z_B^{TM}||Z_d^{TM}}} & \end{aligned} \tag{A.7}$$

Thus, with $Z_{AA'}^{\rightarrow} = \frac{1}{I_1}$, the final sets of equations are:

$$Z_{AA'} = Z_B^{TE}||Z_{AA'}^{\rightarrow} = Z_B^{TE} \left|\left| \left(Z_{TETE} - \frac{Z_{TETM} Z_{TMTE}}{Z_{TMTM} + Z_B^{TM}||Z_d^{TM}} \right) \right.\right. \tag{A.8}$$

$$S_{TETE} = \frac{Z_{AA'} - Z_d^{TE}}{Z_{AA'} + Z_d^{TE}} \tag{A.9}$$

A.2. Calculation of S_{TETM}

S_{TETM} can be expressed as:

$$S_{TETM} = \left. \frac{V_-^{TE}}{V_+^{TM}} \right|_{V_+^{TE}=0} \tag{A.10}$$

To solve this equation, the circuit in Fig. A.6 is used. In this circuit V_{tot}^{TM} is defined as the incident and reflected voltage on the absorber, which can be expressed as:

$$V_{tot}^{TM} = V_+^{TM}(1 + S_{TMTM}) \tag{A.11}$$

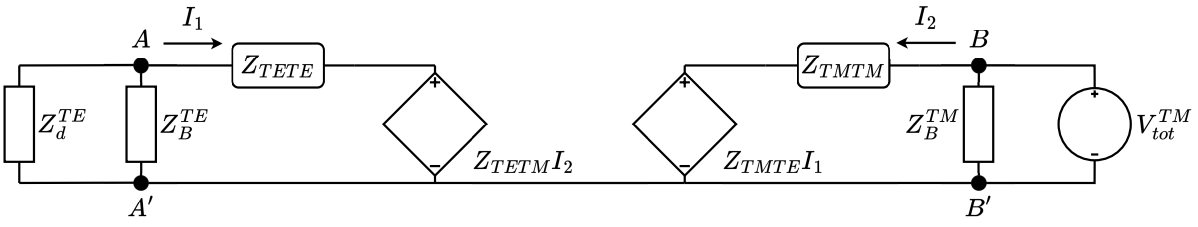

Fig. A.6: Equivalent circuit for finding S_{TETM}, where $V_+^{TE} = 0$

The circuit should be solved for V_-^{TE}, which is the same as the potential seen at AA'. Therefore, V_-^{TE} can be expressed as:

$$V_-^{TE} = V_{AA'} = -I_1 Z_B^{TE}||Z_d^{TE} \tag{A.12}$$

which is an equation in terms of I_1. To find I_1, the circuit should be expressed using a system of equations consisting of:

$$-V_{tot}^{TM} + Z_{TMTM} I_2 + Z_{TMTE} I_1 = 0 \tag{A.13}$$

$$(Z_{TETE} + Z_B^{TE} || Z_d^{TE}) I_1 + Z_{TETM} I_2 = 0 \tag{A.14}$$

Solving Eq. A.14 for I_2 leads to:

$$\begin{aligned} Z_{TETM} I_2 &= -(Z_{TETE} + Z_B^{TE} || Z_d^{TE}) I_1 \\ I_2 &= -\frac{Z_{TETE} + Z_B^{TE} || Z_d^{TE}}{Z_{TETM}} I_1 \end{aligned} \tag{A.15}$$

The result can be substituted into Eq. A.13 as

$$\begin{aligned} Z_{TMTE} I_1 - Z_{TMTM} I_2 &= V_{tot}^{TM} \\ Z_{TMTE} I_1 - Z_{TMTM} \frac{Z_{TETE} + Z_B^{TE} || Z_d^{TE}}{Z_{TETM}} I_1 &= V_{tot}^{TM} \\ \left(Z_{TMTE} - Z_{TMTM} \frac{Z_{TETE} + Z_B^{TE} || Z_d^{TE}}{Z_{TETM}} \right) I_1 &= V_{tot}^{TM} \end{aligned} \tag{A.16}$$

leading to an expression for I_1:

$$I_1 = \frac{V_{tot}^{TM}}{Z_{TMTE} - Z_{TMTM} \frac{Z_{TETE} + Z_B^{TE} || Z_d^{TE}}{Z_{TETM}}} \tag{A.17}$$

Finally, to obtain an expression for V_-^{TE} in terms of V_+^{TM}, Eq. A.17 is substituted into Eq. A.12. After rewriting the expression and expanding V_{tot}^{TM}, the result is as follows:

$$\begin{aligned} V_-^{TE} &= -\frac{V_{tot}^{TM}}{Z_{TMTE} - Z_{TMTM} \frac{Z_{TETE} + Z_B^{TE} || Z_d^{TE}}{Z_{TETM}}} Z_B^{TE} || Z_d^{TE} \\ V_-^{TE} &= -\frac{(1 + S_{TMTM}) Z_B^{TE} || Z_d^{TE}}{Z_{TMTE} - Z_{TMTM} \frac{Z_{TETE} + Z_B^{TE} || Z_d^{TE}}{Z_{TETM}}} V_+^{TM} \end{aligned} \tag{A.18}$$

Since $S_{TETM} = \frac{V_-^{TE}}{V_+^{TM}}\Big|_{V_+^{TE}=0}$, the final expression for S_{TETM} is:

$$S_{TETM} = -\frac{(1 + S_{TMTM}) Z_B^{TE} || Z_d^{TE}}{Z_{TMTE} - Z_{TMTM} \frac{Z_{TETE} + Z_B^{TE} || Z_d^{TE}}{Z_{TETM}}} \tag{A.19}$$

A.3. Calculation of S_{TMTM}

The calculation procedure of S_{TMTM} is very similar to the calculation of S_{TETE} as seen in Sec. A.1. The final expression to calculate S_{TMTM} is:

$$Z_{BB'} = Z_B^{TM} || Z_{BB'}^{\leftarrow} = Z_B^{TM} \left|\left| \left(Z_{TMTM} - \frac{Z_{TMTE} Z_{TETM}}{Z_{TETE} + Z_B^{TE} || Z_d^{TE}} \right) \right.\right. \tag{A.20}$$

$$S_{TMTM} = \frac{Z_{BB'} - Z_d^{TM}}{Z_{BB'} + Z_d^{TM}} \tag{A.21}$$

A.4. Calculation of S_{TMTE}

The calculation of S_{TMTE} is similar to the calculation of S_{TETM} as shown in Sec. Sec. A.2. The final expression to calculate S_{TETM} is:

$$S_{TMTE} = -\frac{(1 + S_{TETE})Z_B^{TM} || Z_d^{TM}}{Z_{TETM} - Z_{TETE}\frac{Z_{TMTM} + Z_B^{TM} || Z_d^{TM}}{Z_{TMTE}}} \tag{A.22}$$

B

Derivation of equivalent sources for an asymmetric absorber

Using the S-parameters of a periodic absorber, as in App. A, the reflected voltages and the current on the absorber can be calculated for an arbitrary set of incoming voltages $V_+^{TE/TM}$. The derivation of $V_-^{TE/TM}$ is trivial, using:

$$\begin{bmatrix} V_-^{TE} \\ V_-^{TM} \end{bmatrix} = S_{abs} \begin{bmatrix} V_+^{TE} \\ V_+^{TM} \end{bmatrix} \tag{B.1}$$

The derivation for $I^{TE/TM}$ is slightly more extensive and is described in the following section.

To derive $I^{TE/TM}$, the equivalent circuit in Fig. B.1 is used. For absorbers with an ideal $\frac{\lambda}{4}$-backing reflector, $Z_B^{TE/TM}$ will approach ∞. In this case, the current on the absorber is simplified to:

$$I^{TE/TM} = \frac{1}{Z_d^{TE/TM}} \left(V_+^{TE/TM} - V_-^{TE/TM} \right) \tag{B.2}$$

For a more generic scenario, the currents should be derived using the Z-parameters of the absorber.

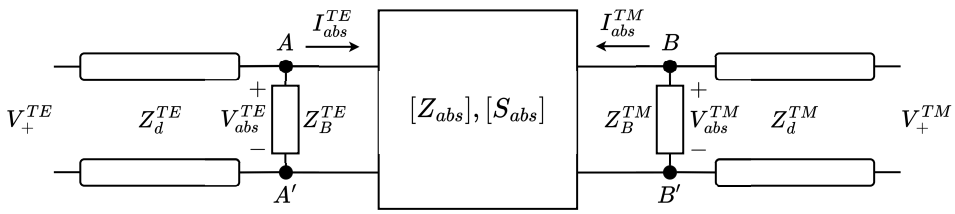

Fig. B.1: An equivalent circuit for the two-port absorber connected to the two transmission lines, similar to Fig. A.1. The voltage across the absorber ports equal the total voltage along the transmission lines, while the currents have to be derived using the Z-parameters of the absorber

Using the Z-parameters of an absorber, the relation between the voltages $V_{abs}^{TE/TM}$ and currents $I_{abs}^{TE/TM}$ can be described as:

$$\begin{bmatrix} V_{abs}^{TE} \\ V_{abs}^{TM} \end{bmatrix} = \begin{bmatrix} Z_{abs}^{TETE} & Z_{abs}^{TETM} \\ Z_{abs}^{TMTE} & Z_{abs}^{TMTM} \end{bmatrix} \begin{bmatrix} I_{abs}^{TE} \\ I_{abs}^{TM} \end{bmatrix} \tag{B.3}$$

Which leads to the expressions for V_{abs}^{TE} and V_{abs}^{TM}:

$$\begin{aligned} V_{abs}^{TE} &= Z_{abs}^{TETE} I_{abs}^{TE} + Z_{abs}^{TETM} I_{abs}^{TM} \\ V_{abs}^{TM} &= Z_{abs}^{TMTE} I_{abs}^{TE} + Z_{abs}^{TMTM} I_{abs}^{TM} \end{aligned} \tag{B.4}$$

From this system of equations, an expression for I_{abs}^{TE} can be derived as:

$$I_{abs}^{TE} = \frac{V_{abs}^{TE} - Z_{abs}^{TETM} I_{abs}^{TM}}{Z_{abs}^{TETE}} \tag{B.5}$$

This equation can be substituted in the expression for V_{abs}^{TM} following from Eq. B.3, leading to

$$V_{abs}^{TM} = Z_{abs}^{TMTE} \frac{V_{abs}^{TE} - Z_{abs}^{TETM} I_{abs}^{TM}}{Z_{abs}^{TETE}} + Z_{abs}^{TMTM} I_{abs}^{TM} \tag{B.6}$$

This equation is rearranged to lead to the final expression for I_{abs}^{TM}:

$$I_{abs}^{TM} = \frac{V_{abs}^{TM} - \frac{Z_{abs}^{TMTE}}{Z_{abs}^{TETE}} V_{abs}^{TE}}{Z_{abs}^{TMTM} - \frac{Z_{abs}^{TMTE} Z_{abs}^{TETM}}{Z_{abs}^{TETE}}} \tag{B.7}$$

A similar derivation leads to the expression for I_{abs}^{TE}:

$$I_{abs}^{TE} = \frac{V_{abs}^{TE} - \frac{Z_{abs}^{TETM}}{Z_{abs}^{TMTM}} V_{abs}^{TM}}{Z_{abs}^{TETE} - \frac{Z_{abs}^{TETM} Z_{abs}^{TMTE}}{Z_{abs}^{TMTM}}} \tag{B.8}$$

C

Analytical and Numerical GO techniques

C.1. Analytical GO

In order to calculate the GO-field using the analytical GO method, two major approximations are made. First of all, the approximation is made that the added phase term $e^{-jks(Q_{FO})}$ can be constant for the elliptical lens that is being analysed. This only works if the eccentricity of the elliptical lens is equal to $e = 1/\sqrt{\epsilon_r}$.

Secondly, the goal of the analytical GO method is to calculate the spreading factor analytically. For a broadside incident plane wave, the spreading factor of an elliptical lens can be represented by:

$$S_{spread}(\theta) = \frac{a\left(1-e^2\right)}{R_{FO}\left(1-e\cos\theta\right)} \tag{C.1}$$

where θ is the angle of the lens' surface from the lower focus of the lens. This spreading factor is based on the ratio between the distance from the focus of the lens to the surface of the lens, and the radius of the FO-sphere.

Using the constant phase and analytical spreading factor alone is only applicable for broadside plane wave illumination of the lens. In cases where the lens is illuminated by an off broadside plane wave, a second approximation is made related to the polarization and phase of the GO-field. In the off broadside case, the polarization is assumed to be the same as the broadside case. Instead, only a progressive phase shift is added[12]:

$$\vec{E}^{GO}(\vec{k}_{\rho,i}) \approx \vec{E}^{GO}(\vec{k}_{\rho,i}=0)e^{-j\vec{k}_{\rho,i}\cdot\vec{\rho}_i} \tag{C.2}$$

where $\vec{k}_{\rho,i} = k_0 \sin\theta_i \left(\cos\phi_i\hat{x} + \sin\phi_i\hat{y}\right)$ is the transversal projection of the incident wave vector, and where $\vec{\rho}_i = r(\theta)\sin\theta\left(\cos\phi\hat{x} + \sin\phi\hat{y}\right)$ is the observation point in the phase reference plane, with the distance to the lens surface $r(\theta)$. The distance to the lens surface can be represented by $r(\theta) = R_{FO} + \delta_i(\theta)$, where $\delta_i(\theta)$ is the distance from the surface of the lens to its FO-sphere. For elliptical lenses this can be written as:

$$\frac{\delta_i(\theta)}{R_{FO}} = \delta_n(\theta) = \frac{e\left(\cos\theta - \cos\theta_0\right)}{1-e\cos\theta} \tag{C.3}$$

Assuming that the FO-sphere has the maximum possible radius, meaning $R_{FO} = F$ where F is the focal distance of the lens, the flash point of the lens can be defined as:

$$\vec{\rho}_{fp} = R_{FO}\frac{\vec{k}_{\rho,i}}{k_0} \tag{C.4}$$

Substituting Eq. C.3 and Eq. C.4 into Eq. C.2, the analytical GO-field can be rewritten as:

$$\vec{E}^{GO}(\vec{k}_{\rho,i}) \approx \vec{E}^{GO}(\vec{k}_{\rho,i}=0)e^{-j\vec{\rho}_{fp}\cdot\vec{k}_{\rho}(1+\delta_n(\theta))} \tag{C.5}$$

This approximation corresponds to an error in the calculated field that is proportional to $\tan\theta_i$ due to ignoring the change in polarization of incident plane waves in off broadside cases[12]. Limiting the polarization error budget to 20% leads to a limitation on the analytical GO method of $\theta_i < 11°$. Thus, the analytical GO/FO method should only be used for validation cases with either broadside, or slight off broadside incident plane waves. A numerical GO method is applied here for larger incident angles.

C.2. Numerical GO

Instead of analytically determining the spreading factor of the Quasi-Optical component, the spreading factor can also be computed using the method described in [13]:

$$S_{spread}(Q_{FO}) = \sqrt{\frac{\rho_1^{r/t}(Q_{FO})\rho_2^{r/t}(Q_{FO})}{\left(\rho_1^{r/t}(Q_{FO})+s(Q_{FO})\right)\left(\rho_2^{r/t}(Q_{FO})+s(Q_{FO})\right)}} \tag{C.6}$$

where $\rho_1^{r/t}(Q_{FO})$ and $\rho_2^{r/t}(Q_{FO})$ are the principal radii of curvature of the reflected or transmitted wave fronts respectively, which are expressed in [37].

In order to calculate the spreading factor and the phase changes due to the propagation from the lens surface to the FO-sphere, this path length has to be evaluated. In order to do this, a raytracing technique is employed, which is described in further detail in App. D.

The advantage of using the numerical method, is that this technique can be applied to any arbitrary Quasi-Optical component, since the raytracing technique can find the path length between any surface and the FO-sphere.

C.3. The transmission and reflection dyads

For the GO technique, the field scattering on the Quasi-Optical surface can by calculated by applying either the reflection or transmission dyad to the incoming field:

$$\vec{E}^{r}(Q_R) = \vec{E}^{i}\cdot\bar{R}(Q_R) \tag{C.7}$$

$$\vec{E}^{t}(Q_T) = \vec{E}^{i}\cdot\bar{T}(Q_T) \tag{C.8}$$

where $Q_{R/T}$ represents the reflecting or transmitting surface, and $\bar{R}$ and $\bar{T}$ are the reflection and transmission dyads, respectively[13]. These dyads can be calculated as:

$$\bar{R}(Q) = \Gamma^{TE}\hat{p}^{i,TE}\hat{p}^{r,TE} + \Gamma^{TM}\hat{p}^{i,TM}\hat{p}^{r,TM} \tag{C.9}$$

$$\bar{T}(Q) = \tau^{TE}\hat{p}^{i,TE}\hat{p}^{t,TE} + \tau^{TM}\hat{p}^{i,TM}\hat{p}^{t,TM} \tag{C.10}$$

where $\Gamma^{TE/TM}$ and $\tau^{TE/TM}$ are the reflection and transmission coefficients on the QO surface, $\hat{p}^{r,TE/TM}$ and $\hat{p}^{t,TE/TM}$ are the polarization unit vectors of the reflected and transmitted rays, and $\hat{p}^{i,TE/TM}$ are the polarization unit vectors of the incident rays.

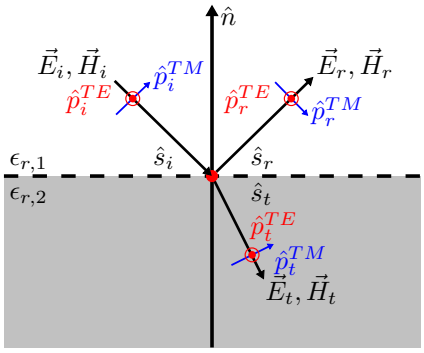

Fig. C.1: Electric and Magnetic fields $\vec{E}_i$ and $\vec{H}_i$ with polarizations defined by $\hat{p}_i^{TE/TM}$ and the direction of propagation $\hat{s}_i$, incident on an interface of two materials: one with relative permittivity $\epsilon_{r,1}$, and one with relative permittivity $\epsilon_{r,2}$. The reflected fields are defined by $\vec{E}_r$ and $\vec{H}_r$ with polarizations $\hat{p}_r^{TE/TM}$ and the direction of propagation $\hat{s}_r$, and the transmitted fields are defined by $\vec{E}_t$ and $\vec{H}_t$ with polarizations $\hat{p}_t^{TE/TM}$ and the direction of propagation $\hat{s}_t$.

The electric field can be decomposed into TE and TM components, for this decomposition, the corresponding polarization unit vectors need to be defined. Following the illustration in Fig. C.1, the polarizations for the incident, transmitted, and reflected rays respectively can be defined by:

$$\begin{aligned}
\hat{p}_i^{TE} &= \frac{\hat{s}_i \times \hat{n}}{|\hat{s}_i \times \hat{n}|} & \hat{p}_t^{TE} &= \frac{\hat{s}_t \times \hat{n}}{|\hat{s}_t \times \hat{n}|} & \hat{p}_r^{TE} &= \frac{\hat{s}_r \times \hat{n}}{|\hat{s}_r \times \hat{n}|} \\
\hat{p}_i^{TM} &= \hat{p}_i^{TE} \times \hat{s}_i & \hat{p}_t^{TM} &= \hat{p}_t^{TE} \times \hat{s}_t & \hat{p}_r^{TM} &= \hat{s}_r \times \hat{p}_r^{TE}
\end{aligned} \tag{C.11}$$

All that remains, is the calculation of the Fresnel reflection and transmission coefficients in order to calculate the reflection and transmission dyads. These coefficients can be found by applying boundary conditions on the electric and magnetic field at the surface location Q. For lenses, the coefficients of interest are the transmission coefficients, which are derived for a lens without a matching layer as [14]:

$$\begin{aligned}
\tau^{TE}(Q) &= \frac{2\eta_2 \cos\theta_i}{\eta_2 \cos\theta_i + \eta_1 \cos\theta_t} \\
\tau^{TM}(Q) &= \frac{2\eta_2 \cos\theta_i}{\eta_1 \cos\theta_i + \eta_2 \cos\theta_t}
\end{aligned} \tag{C.12}$$

where $\eta_1 = \eta_0/\sqrt{\epsilon_{r,1}}$ and $\eta_2 = \eta_0/\sqrt{\epsilon_{r,2}}$ are the impedances of media 1 and 2, respectively, with $\eta_0 = 120\pi$ as the impedance of free space.

The issue with using lenses without matching layers, is that there is often a large mismatch between the impedance of free-space, and the impedance of the material of the lens. This mismatch will lead to a large reduction in the transmitted field.

For these cases, a matching layer with a thickness of $\frac{\lambda}{4}$ can be added on top of the lens. The transmission coefficients in this case are equal to [14]:

$$\begin{aligned}
\tau^{TE} &= \frac{V_{d+}^{TE}(z=-d_m)}{V_{0+}^{TE}(z=0)} \\
\tau^{TM} &= \frac{V_{d+}^{TM}(z=-d_m)}{V_{0+}^{TM}(z=0)} \frac{\cos\theta_i}{\cos\theta_t^d}
\end{aligned} \tag{C.13}$$

where d_m is the thickness of the matching layer, $V_{0+}^{TE/TM}(z=0)$ are the voltages at the air-matching layer interface, and $V_{d+}^{TE/TM}(z=-d_m)$ are defined as

$$V_{d+}^{TE/TM}(z=-d_m)=\frac{\tau_1^{TE/TM}\tau_2^{TE/TM}V_{0+}^{TE/TM}(z=0)e^{-jk_{zm}d_m}}{1+\Gamma_2^{TE/TM}e^{-2jk_{zm}d_m}} \tag{C.14}$$

where $\Gamma_2^{TE/TM}=\frac{Z_2^{TE/TM}-Z_m^{TE/TM}}{Z_2^{TE/TM}+Z_m^{TE/TM}}$ are the reflection coefficients on the matching layer-lens interface, $\tau_1^{TE/TM}=\frac{2Z_1^{TE/TM}}{Z_1^{TE/TM}+Z_0^{TE/TM}}$ are the transmission coefficients through the air-matching layer interface, and $\tau_2^{TE/TM}=\frac{2Z_2^{TE/TM}}{Z_2^{TE/TM}+Z_m^{TE/TM}}$ are the transmission coefficients through the matching layer-lens interface, with $Z_1^{TE/TM}$ and $Z_2^{TE/TM}$ as the input impedances seen at the air-matching layer and matching layer-lens interface, respectively.

D

Raytracing for numerical GO analysis

In order to apply the GOFO method on lenses, the distance between the surface of a lens and the FO-sphere must be determined. To do so, a raytracing technique can be applied where for an incoming ray with a direction $\hat{s}_i$ incident on a location on the surface of the lens defined by Q_T, the location on the FO-sphere defined by Q_{FO} can be obtained.

To derive these locations on the FO-sphere, the following system of equations can be defined

$$\begin{bmatrix} Q_{FO}^x \\ Q_{FO}^y \\ Q_{FO}^z \end{bmatrix} = \begin{bmatrix} Q_T^x \\ Q_T^y \\ Q_T^z \end{bmatrix} + s \begin{bmatrix} s_t^x \\ s_t^y \\ s_t^z \end{bmatrix} \tag{D.1}$$

where $Q_{FO}^{x/y/z}$ and $Q_T^{x/y/z}$ are x, y, and z coordinates on the FO-sphere and the surface of the lens, respectively, s is the propagation length of the ray between these two sets of coordinates, and $\hat{s}_t^{x/y/z}$ are the x, y, and z components of the direction of propagation of the ray after transmitting through the surface of the lens. In this equation, the coordinates on the surface of the lens Q_T are known, and the direction of incidence $\hat{s}_i$ is know. Using the equations in Sec. C.3, the direction of the transmitted ray $\hat{s}_t$ can be found. With these known variables two unknown variables remain: the propagation length s, and the coordinates on the FO-sphere of the ray Q_{FO}. If the coordinates Q_{FO} are related to each other, Eq. D.1 can be solved for s and Q_{FO}.

For a lens with an FO-sphere with radius R_{FO}, the surface of the FO-sphere can be defined by

$$\left(Q_{FO}^x\right)^2 + \left(Q_{FO}^y\right)^2 + \left(Q_{FO}^z\right)^2 = R_{FO}^2 \tag{D.2}$$

This equation can be combined with Eq. D.1, leading to

$$\begin{bmatrix} Q_{FO}^x \\ Q_{FO}^y \\ \sqrt{R_{FO}^2 - \left(Q_{FO}^x\right)^2 - \left(Q_{FO}^y\right)^2} \end{bmatrix} = \begin{bmatrix} Q_T^x \\ Q_T^y \\ Q_T^z \end{bmatrix} + s \begin{bmatrix} s_t^x \\ s_t^y \\ s_t^z \end{bmatrix} \tag{D.3}$$

The equation can be simplified by taking the first two equations for Q_{FO}^x and Q_{FO}^y in Eq. D.3 and substituting them into the third equation. This leads to the following polynomial:

$$
\begin{aligned}
&s^2\left[\left(s_t^x\right)^2+\left(s_t^y\right)^2+\left(s_t^z\right)^2\right]+\\
&s\left[2\left(s_t^xQ_T^x+s_t^yQ_T^y+s_t^zQ_T^z\right)\right]+\\
&\left[\left(Q_T^x\right)^2+\left(Q_T^y\right)^2+\left(Q_T^z\right)^2-R_{FO}^2\right]=0
\end{aligned}
\tag{D.4}
$$

Since $\hat{s}_t$ is a unit vector, the coefficients of this second order polynomial can be defined as:

$$
\begin{aligned}
p_1&=1\\
p_2&=2\left(s_t^xQ_T^x+s_t^yQ_T^y+s_t^zQ_T^z\right)\\
p_3&=\left(Q_T^x\right)^2+\left(Q_T^y\right)^2+\left(Q_T^z\right)^2-R_{FO}^2
\end{aligned}
\tag{D.5}
$$

Solving this second order polynomial leads to two possible results. By selecting the smallest non-negative result, the propagation length of the ray can be found for a given location on the surface of the lens defined by Q_T.

E

Kinetic Inductance Fraction of Transmission Line resonators

For a quarter-wavelength transmission line resonator, the resonance frequency of the resonator can be expressed by

$$f_0 = \frac{1}{4l\sqrt{LC}} \tag{E.1}$$

where l is the length of the resonator, C is the capacitance per unit length of the resonator, and L is the inductance of the resonator.

The kinetic inductance fraction is defined as[27]

$$\alpha = \frac{L_k}{L_t} = \frac{L_k}{L_k + L_g} \tag{E.2}$$

where L_k is the kinetic inductance of the resonator, and L_g is the geometrical inductance of the resonator, and $L_t = L_k + L_g$ is the total inductance. By measuring the resonance frequency of a resonator with and without superconducting material, this kinetic inductance fraction can be obtained. For this, the resonance frequencies of both resonators can be expressed as

$$f_{Al} = \frac{1}{4l\sqrt{L_t C}} \tag{E.3}$$

$$f_{PEC} = \frac{1}{4l\sqrt{L_g C}} \tag{E.4}$$

where f_{Al} is the resonance frequency of a resonator made with superconductive aluminium, and f_{PEC} is the resonance frequency of the same resonator made with a non-superconductive material (in this case PEC). These equations can be rewritten to express the total inductance (L_t) and geometric inductance (L_g) in terms of the resonance frequencies:

$$L_t = \frac{1}{C\left[4lf_{Al}\right]^2} \tag{E.5}$$

$$L_g = \frac{1}{C\left[4lf_{PEC}\right]^2} \tag{E.6}$$

By using the fact that $L_k = L_t - L_g$, the equations above can be substituted into Eq. E.2, leading to an expression for the kinetic inductance fraction in terms of resonance frequencies of the transmission line resonator:

$$\begin{aligned}\alpha &= \frac{L_t - L_g}{L_t} \\ &= \frac{\frac{1}{C[4lf_{Al}]^2} - \frac{1}{C[4lf_{PEC}]^2}}{\frac{1}{C[4lf_{Al}]^2}} \\ &= \frac{\frac{1}{f_{Al}^2} - \frac{1}{f_{PEC}^2}}{\frac{1}{f_{Al}^2}} \\ &= 1 - \left[\frac{f_{Al}}{f_{PEC}}\right]^2\end{aligned} \tag{E.7}$$

which can be rewritten for clarity as:

$$\alpha = 1 - \delta F^2 \tag{E.8}$$

where $\delta F = \frac{f_{Al}}{f_{PEC}}$.

F

Absorber Design Parameters for 1.5 THz

This chapter contains all parameters for the complete absorber structures, for each of the 4 absorber designs discussed in Ch. 2. For reference, the parameter definition of the absorber unit cell is shown in Fig. F.1a, and the parameter definitions of the feeding lines and absorber width and height is shown in Fig. F.1a.

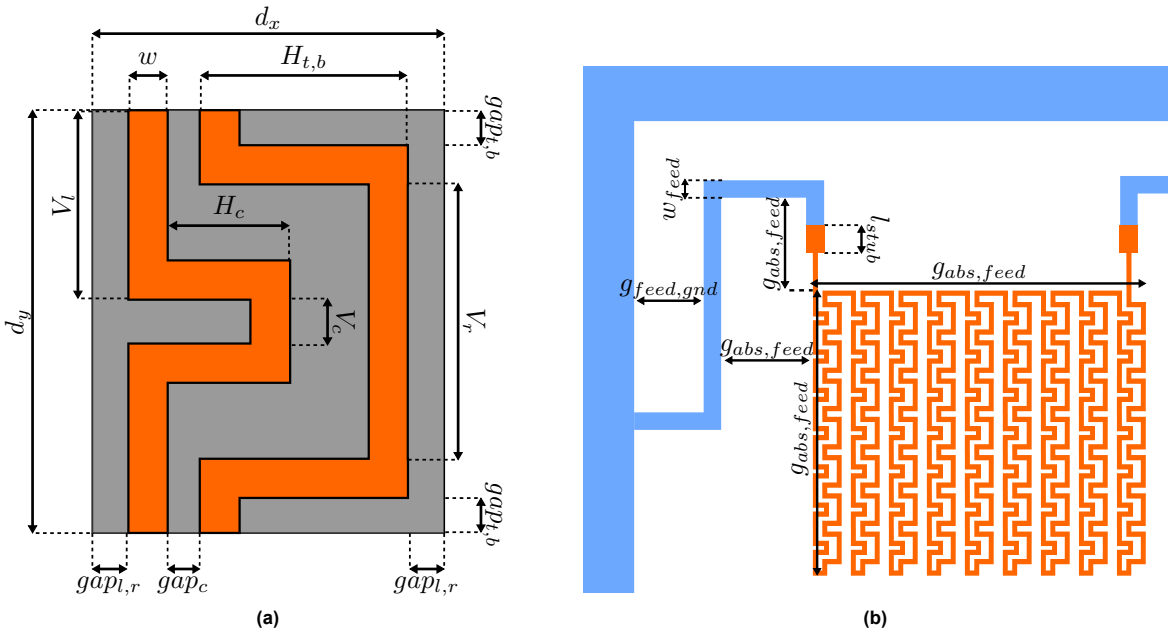

Fig. F.1: Definitions of the dimensions for (a) a unit-cell of the absorber and (b) dimensions of the feeding lines of the absorber structure connected to a complete absorber. In both figures the Aluminium is coloured orange, and the NbTiN is coloured blue.

F.1. Absorber Design with 21 nm thick Aluminium and a line width of 0.6 $\mu\mathrm{m}$

Parameter name	JSON fieldname	Value [$\mu\mathrm{m}$]
$gap_{l,r}$	gap_l_and_r	2.4
$gap_{t,b}$	gap_t_and_b	2.6
gap_c	gap_c	0.63
$H_{t,b}$	horz_t_and_b	25
H_c	horz_c	14.33
V_l	vert_l	16.885
V_r	vert_r	28
V_c	vert_c	0.63
w	w	0.6
d_x	N/A	31.03
d_y	N/A	34.4
W	array_width	279.27
H	array_height	240.8
w_{feed}	feed_w	10
l_{stub}	feed_stub	20
$g_{abs,feed}$	gap_abs_feed	60
$g_{feed,gnd}$	gap_feed_gnd	35

Tab. F.1: Dimension values for each parameter in the complete absorber design, including the feeding lines, for the absorber design made with 21 nm thick Aluminium and a line width of 0.6 $\mu\mathrm{m}$.

F.2. Absorber Design with 21 nm thick Aluminium and a line width of 1.3 $\mu\mathrm{m}$

Parameter name	JSON fieldname	Value [$\mu\mathrm{m}$]
$gap_{l,r}$	gap_l_and_r	2.4
$gap_{t,b}$	gap_t_and_b	3
gap_c	gap_c	0.63
$H_{t,b}$	horz_t_and_b	22
H_c	horz_c	14.33
V_l	vert_l	17.985
V_r	vert_r	28
V_c	vert_c	0.63
w	w	1.3
d_x	N/A	28.73
d_y	N/A	36.6
W	array_width	258.57
H	array_height	256.2
w_{feed}	feed_w	10
l_{stub}	feed_stub	20
$g_{abs,feed}$	gap_abs_feed	60
$g_{feed,gnd}$	gap_feed_gnd	35

Tab. F.2: Dimension values for each parameter in the complete absorber design, including the feeding lines, for the absorber design made with 21 nm thick Aluminium and a line width of 1.3 $\mu\mathrm{m}$.

F.3. Absorber Design with 28 nm thick Aluminium and a line width of 0.6 $\mu\mathrm{m}$

Parameter name	JSON fieldname	Value [$\mu\mathrm{m}$]
$gap_{l,r}$	gap_l_and_r	2.6
$gap_{t,b}$	gap_t_and_b	2.8
gap_c	gap_c	0.63
$H_{t,b}$	horz_t_and_b	21.23
H_c	horz_c	14.33
V_l	vert_l	18.25
V_r	vert_r	30.33
V_c	vert_c	0.63
w	w	0.6
d_x	N/A	27.66
d_y	N/A	37.13
W	array_width	248.94
H	array_height	259.91
w_{feed}	feed_w	10
l_{stub}	feed_stub	20
$g_{abs,feed}$	gap_abs_feed	60
$g_{feed,gnd}$	gap_feed_gnd	35

Tab. F.3: Dimension values for each parameter in the complete absorber design, including the feeding lines, for the absorber design made with 28 nm thick Aluminium and a line width of 0.6 $\mu\mathrm{m}$.

F.4. Absorber Design with 28 nm thick Aluminium and a line width of 1.3 $\mu\mathrm{m}$

Parameter name	JSON fieldname	Value [$\mu\mathrm{m}$]
$gap_{l,r}$	gap_l_and_r	2
$gap_{t,b}$	gap_t_and_b	3.5
gap_c	gap_c	0.63
$H_{t,b}$	horz_t_and_b	22
H_c	horz_c	14.33
V_l	vert_l	18.485
V_r	vert_r	28
V_c	vert_c	0.63
w	w	1.3
d_x	N/A	27.93
d_y	N/A	37.6
W	array_width	251.37
H	array_height	263.2
w_{feed}	feed_w	10
l_{stub}	feed_stub	20
$g_{abs,feed}$	gap_abs_feed	60
$g_{feed,gnd}$	gap_feed_gnd	35

Tab. F.4: Dimension values for each parameter in the complete absorber design, including the feeding lines, for the absorber design made with 28 nm thick Aluminium and a line width of 1.3 $\mu\mathrm{m}$.

G

High Frequency Absorber Designs

Two high-frequency absorber designs designed for a wavelength of 18.5 μm (16.2 THz) and 8.5 μm (35.3 THz). These designs are limited by two fabrication parameters: a minimum feature size of 250 nm, and a minimum gap size between features of 250 nm. The designs serve as a proof of concept of the design strategy presented in Ch. 2 for higher frequencies.

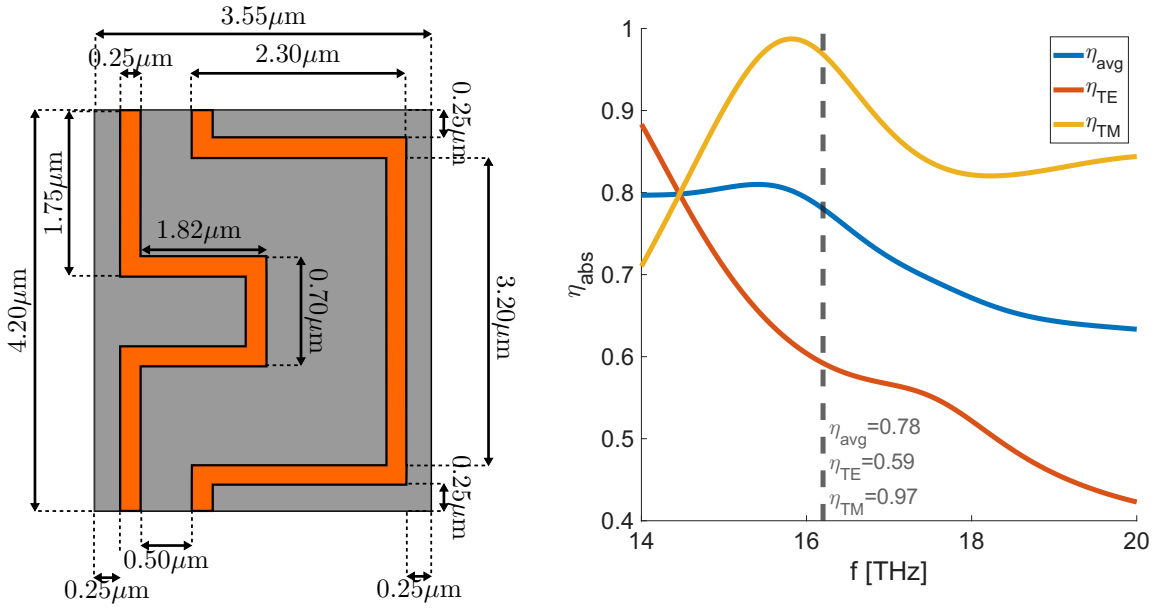

(a) (b)

Fig. G.1: Absorber design for a wavelength of $\lambda_0 = 18.5\mu$m. Shown is the (a) unit cell design, and (b) the absorption efficiency for broadside incidence.

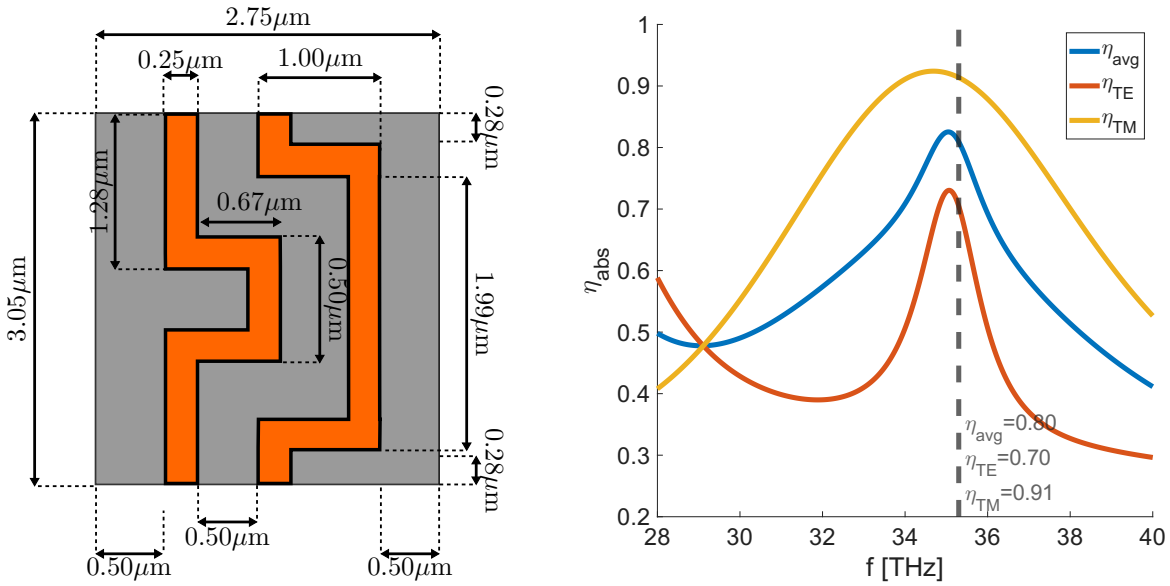

(a) **(b)**

Fig. G.2: Absorber design for a wavelength of $\lambda_0 = 8.5\mu\text{m}$. Shown is the (a) unit cell design, and (b) the absorption efficiency for broadside incidence.

H

JSON Absorber Definition File Format

```
{
    id: string,
    description: string | undefined,
    // Absorber unit-cell dimensions (in microns)
    gap_l_and_r: number,
    gap_t_and_b: number,
    gap_c: number,
    horz_t_and_b: number,
    horz_c: number,
    vert_l: number,
    vert_r: number,
    vert_c: number,
    w: number,
    // Absorber structure dimensions (in microns)
    array_width: number,
    array_height: number,
    feed_w: number,
    feed_stub: number,
    gap_abs_feed: number,
    gap_feed_gnd: number,
    feed_overlap: number,
    // Settings for inverted masks
    inverted: boolean,          // Defines if mask should be inverted
    invert_offset: number,      // Offset added to certain parts (in microns)
    // Relative path to previously simulated Sonnet data
    sonnet_data: string,
    // Material data for the absorber and MKID
    absorber_material: {
        Tc: number,     // Critical temperature in Kelvin
        rho: number,    // Resistivity in Ohm*m
        d: number       // Thickness in m
    },
    mkid_material: {
        Tc: number,
        rho: number,
        d: number
    }
}
```